ALMA MATER STUDIORUM · UNIVERSITY OF BOLOGNA

School of Science
Department of Physics and Astronomy
Master Degree in Physics

Diagnosing criticality in symmetric and chiral clock models

Supervisor:
Prof. Elisa Ercolessi

Co-supervisor:
Sunny Pradhan

Submitted by:
Laura Pecorari

Academic Year 2021/2022

Abstract

Quantum clock models are statistical mechanical spin models which may be regarded as a sort of bridge between the one-dimensional quantum Ising model and the one-dimensional quantum XY model. This thesis aims to provide an exhaustive review of these models using both analytical and numerical techniques. We present some important duality transformations which allow us to recast clock models into different forms, involving for example parafermions and lattice gauge theories. Thus, the notion of topological order enters into the game opening new scenarios for possible applications, like topological quantum computing. The second part of this thesis is devoted to the numerical analysis of clock models. We explore their phase diagram under different setups, with and without chirality, starting with a transverse field and then adding a longitudinal field as well. The most important observables we take into account for diagnosing criticality are the energy gap, the magnetisation, the entanglement entropy and the correlation functions.

Sommario

I clock model quantistici sono modelli di spin studiati in meccanica statistica che si collocano a metà strada fra il modello di Ising e il modello XY. Con questa tesi ci si propone di condurre una rassegna il più possibile esaustiva di questi modelli, utilizzando tecniche analitiche e numeriche. Presentiamo alcune importanti trasformazioni di dualità che permettono di trasformare i clock model in forme nuove, per esempio ricorrendo al linguaggio dei parafermioni e delle teorie di gauge su reticolo. Questo permette di introdurre la nozione di ordine topologico aprendo nuovi scenari per possibili applicazioni, quali la compuazione quantistica topologica. La seconda parte di questa tesi è riservata all'analisi numerica dei clock model. Ne esploriamo il diagramma di fase studiando configurazioni diverse: con e senza chiralità, introduciamo inizialmente soltanto un campo trasverso, successivamente applichiamo anche un campo longitudinale. I principali osservabili fisici che studiamo per diagnosticare la criticità sono il gap di energia, la magnetizzazione, l'entropia di entanglement e le funzioni di correlazione.

Contents

List of Figures v

List of Tables vii

Introduction 1

1 Critical phenomena: an overview 5
- 1.1 Field theoretical background . . . 5
- 1.2 Quantum phase transitions . . . 7
  - 1.2.1 Observables at criticality . . . 8
  - 1.2.2 QPTs with Spontaneous Symmetry Breaking (SSB) . . . 11
  - 1.2.3 Beyond SSB: BKT transitions and the XY-model . . . 12
- 1.3 Critical exponents and universality classes . . . 15
- 1.4 Finite-size scaling . . . 17
- 1.5 The quantum Ising model . . . 20

2 Quantum clock models 24
- 2.1 *p*-state clock models . . . 24
  - 2.1.1 The model . . . 26
  - 2.1.2 Phase diagram . . . 27
- 2.2 *p*-state chiral clock models . . . 29
  - 2.2.1 What does *chiral* mean? . . . 30
  - 2.2.2 The model . . . 31
  - 2.2.3 Phase diagram . . . 32
- 2.3 Symmetries . . . 34

3 Duality transformations 37
- 3.1 Kramers-Wannier duality . . . 37
- 3.2 Jordan-Wigner duality . . . 40
- 3.3 Fradkin-Kadanoff duality . . . 44
- 3.4 Clock models and Lattice Gauge Theories . . . 45
  - 3.4.1 Lattice gauge theories in a nutshell . . . 46
  - 3.4.2 Bond-algebraic approach to dualities . . . 48
  - 3.4.3 Ladder LGT-clock models duality . . . 49

4 Numerical analysis **52**
4.1 DMRG parameters . . . 53
4.2 Symmetry implementation . . . 53
4.3 $p = 3$, 4-state clock models with transverse field . . . 54
4.3.1 Energy gap . . . 54
4.3.2 Entanglement entropy . . . 58
4.3.3 Magnetisation . . . 60
4.3.4 Binder cumulant . . . 62
4.3.5 Correlation functions at criticality . . . 63
4.4 $p \geq 5$-state clock models with transverse field . . . 65
4.4.1 Energy gap for $p = 5$ and $p = 6$ . . . 65
4.4.2 Magnetisation . . . 67
4.5 $p = 3$-state chiral clock models with transverse field . . . 68
4.5.1 Energy gap . . . 69
4.5.2 Lifshitz oscillations . . . 76
4.5.3 Entanglement entropy . . . 79
4.5.4 Correlation functions at criticality . . . 81
4.5.5 Binder cumulant . . . 86
4.6 Adding a longitudinal field . . . 89
4.6.1 Phase diagram . . . 89
4.6.2 Duality with Lattice Gauge Theories . . . 92

Conclusions and outlooks **95**

A Computational tools **97**
A.1 The Density Matrix Renormalisation Group . . . 97
A.1.1 Infinite-system DMRG . . . 98
A.1.2 Finite-system DMRG . . . 99
A.2 Tensor Networks: a brief overview . . . 100
A.2.1 Matrix Product States . . . 101
A.2.2 Matrix Product Operators . . . 102

Bibliography **103**

List of Figures

2.1 Pictorial representation of the classical clock model. 25
2.2 Pictorial representation of the action of the Z operator. 27
2.3 Phase diagram of p-state clock models vs XY model. 29
2.4 Picture of the three possible values of $s_j^* s_k e^{i\theta}$ for $\theta = 0$ and $\theta \neq 0$. . . 31

3.1 Pictorial representation of the plaquette and Gauss' operators on the ladder. 47
3.2 Pictorial representation of the LGT-to-clock model duality. 50

4.1 Plot of the energy levels of the 3 and 4-state clock model. 55
4.2 Plot of the energy gap of the 3 and 4-state clock model. 55
4.3 Scaling of the energy gap of the 3- and 4- state clock models. 56
4.4 Critical exponent ν for 3- and 4-state clock models. 57
4.5 Half chain entanglement entropy of the 3-state clock model. 59
4.6 Finite-size scaling of the entanglement entropy for the 3- and 4-state clock model. 59
4.7 Magnetisation of the 3- and 4-state clock models (PBC). 61
4.8 Universal scaling of the magnetisation for the 3- and 4-state clock models (PBC). 61
4.9 Fourth-order Binder cumulant of the 3-state clock model. 63
4.10 Correlation functions of 3 and 4-state clock models at criticality. . . . 64
4.11 Plot of the energy gap of the 5 and 6-state clock model. 66
4.12 Scaling of the energy gap for the 5-state clock model. 67
4.13 Magnetisation for the 5-state clock model (PBC). 68
4.14 Two possible scenarios for the phase diagram of 3-state chiral clock models. 70
4.15 Plot of the energy gap of the 3-state chiral clock model at two different angles, $\theta = \phi = \frac{\pi}{4}$ and $\frac{\pi}{10}$. 70
4.16 Critical exponent ν for the Pokrovsky-Talapov transition. 71
4.17 Critical exponent $z\nu$ at small angles (self-dual case). 73
4.18 Phase diagram and plot of the energy gap of the 3-state chiral clock model with $\theta = 0.9$ and $\phi = 0$. 74

4.19 Phase diagram and plot of the energy gap of the 3-state chiral clock model with $\phi = 0.9$ and $\theta = 0$. 74
4.20 Plot of the energy levels of the 3-state chiral clock model 75
4.21 Oscillations of the energy gaps of the 3-state chiral clock model in the different symmetry sectors. 76
4.22 Plot of the oscillations in the energy levels of the 3-state chiral clock model. 77
4.23 Oscillations of the energy gap of the 3-state chiral clock model. 77
4.24 Half chain entanglement entropy of the 3-state chiral clock model. . . 80
4.25 Absolute value, real and imaginary part of the correlation functions of the 3-state chiral clock model within the IC phase. 81
4.26 Correlation functions of the 3-state chiral clock model within the IC phase as a function of h. 82
4.27 Correlation functions of the 3-state chiral clock model within the IC phase as a function of θ. 82
4.28 Plots of the wave vector k and the oscillation length ℓ as a function of h. 83
4.29 Incommensurability exponent at Pokrovsky-Talapov for $\theta = \frac{\pi}{4}$ and $\frac{\pi}{5}$. 84
4.30 Plots of the wave vector k and the oscillation length ℓ as a function of θ. 85
4.31 Binder cumulant for the 3-state chiral clock model with $\theta = \phi = \frac{\pi}{10}$. . 87
4.32 Universal scaling of the Binder cumulant for the 3-state chiral clock model. 88
4.33 Phase diagram of the 3-state symmetric clock model with both transverse and longitudinal field. 90
4.34 Phase diagram of the 3-state chiral clock model with both transverse and longitudinal field. 90
4.35 Energy gaps of the 3-state clock model with transverse and longitudinal fields. 93
4.36 Transverse and longitudinal magnetisation of the 3-state clock model with transverse and longitudinal fields. 94

A.1 Infinite-system DMRG vs finite-system DMRG. 100

List of Tables

1.1 Incomplete list of critical exponents. 16
1.2 Incomplete list of universality classes. 17

2.1 Dictionary of commensurate-incommensurate transitions. 33

Introduction

Phase transitions are ubiquitous in nature. Since decades they have shown themselves familiar in our common experience and yet not fully understood, exhaustive in their classification and then prolific arena for constant discoveries. All these features have contributed to make them one of the most compelling phenomena of modern physics, raising a long-standing interest in several research areas, both on theoretical and experimental grounds.

In physics one needs a theory in order to make quantitative predictions. So let us here recall some historical notes about the theory of critical phenomena. Its birth may be traced to the experiments performed by Thomas Andrews in 1869 [2] on the liquid-gas transition in carbon dioxide. This transition is indeed accompanied by the phenomenon of critical opalescence, which can be explained in terms of strong fluctuations in the density of the liquid reflecting into fluctuations in the refraction index near criticality. This was firstly understood by Marian von Smoluchowski in 1908 [75] and then formalised by Albert Einstein in 1910 [21]. Since then, many other phase transitions have been investigated and new exotic phases of matter have been discovered, especially in the quantum regime. At the same time many ideas of condensed matter physics started to spread to other physical areas, going even far beyond the domain of solid-state physics. Among those it is worth mentioning at least three famous examples, namely the Bose-Einstein condensate, BCS-superconductivity and the quark-gluon plasma. Such a richness of critical behaviours immediately pushed the need for a synthesis from the reductionist perspective, which culminated with the Ginzburg-Landau theory in 1950 [47] which is still largely exploited nowadays. Originally developed within the framework of superconductivity, this theory allows to reshape the theory of critical phenomena in a group-theoretical fashion by associating different symmetries with different phases - or orders - and explaining phase transitions in terms of the spontaneous symmetry breaking mechanism. However, the Ginzburg-Landau theory is not able to describe all possible orders and new phases which do not fit this paradigm have been soon discovered. The most famous examples are Berezinskii-Kosterlitz-Thouless

transitions [7, 8, 44], high-temperature superconductivity [6], the fractional quantum Hall effect [48] and all models displaying topological order in general [14].

The most widespread and paradigmatic playground for studying critical phenomena is the Ising model [37]. This is indeed the simplest statistical mechanical model exhibiting a phase transition. It may be thought of as a d-dimensional lattice with spins variables - either classical, i.e. boolean, or quantum - attached at each site. Only neighbouring spins are allowed to interact with each other and a transverse magnetic field is usually applied. Despite the apparent simplicity and the high degree of abstraction, this model already encodes most of the salient features of critical systems and allows for extremely interesting applications even on the experimental ground. Following the success of the Ising model, many other spin models with different symmetry group (e.g. $\mathbb{Z}_p$, $U(1)$, $O(p)\dots$) have then been introduced. Among these, clock models are highly notable. Not only they provide the simplest and most natural generalisation of the $\mathbb{Z}_2$ symmetry of the Ising model to the $\mathbb{Z}_p$ symmetry, but they also share a deep connection with another extremely famous statistical model, namely the XY model. Thus, depending on the clock order, they may enjoy properties of either model, like the Kramers-Wannier duality when $p \leq 4$ or the emergence of a new critical phase of Berezinskii-Kosterlitz-Thouless type for $p \geq 5$.

Standard clock models, like Potts and Ashkin-Teller, are symmetric in nature, as the interaction energy between two spins is left invariant by their interchange. Thus, the three discrete spacetime symmetries of parity, time reversal and charge conjugation are preserved. However, it is possible to explicitly break these symmetries by introducing chiral interactions into the clock Hamiltonian. This may be practically achieved by allowing the coupling constants to take complex values and avoiding special configurations which would restore the symmetry of the model. When this happens to be the case, clock models are said to be chiral. Chiral clock models were firstly studied by Stellan Ostlund in 1980 [61] who suggested that they may host in their phase diagram a new critical and floating incommensurate phase having no counterpart either in symmetric clock models or in the chiral Ising model. For this reason, chiral clock models represent the best testing ground for investigating a long-standing problem of condensed matter physics, namely the commensurate-incommensurate transition, which has recently risen in new popularity in the study of Rydberg atoms [17].

With the present dissertation we aim to fit into this framework by presenting a review of both symmetric and chiral models. The main duality transformations involving these models are discussed as well. A special focus is then deserved to

the study of their critical behaviour, which is investigated via DMRG numerical simulations with tensor networks.

This thesis is organised as follows. In Chapter 1 we provide a quick overview of the theory of critical phenomena. After recalling a few necessary notions of quantum field theory, we present quantum phase transitions and discuss the behaviour of the main thermodynamic observables at criticality. The mechanism of spontaneous symmetry breaking lying behind most phase transitions is described and the example of Berezinskii-Kosterlitz-Thouless transitions, which instead do not fit this paradigm, is provided. Then we move on discussing the universality of phase transitions which allows for their organisation into universality classes and the finite-size scaling which we have to deal with when working out of the thermodynamic limit. We end the chapter by reviewing the quantum Ising model in one dimension.

In Chapter 2 we introduce both symmetric and chiral p-state clock models with different fields and couplings. We also discuss the topology of their phase diagrams according to the literature. The very last part of this chapter focuses on the symmetries enjoyed by these models. A special attention is given to the three discrete spacetime symmetries of parity, time reversal and charge conjugation along with their explicit violation.

Chapter 3 aims to review the most important duality transformations involving these models. The Kramers-Wannier duality both for Ising and clock models is firstly presented. Then we discuss the Jordan-Wigner transformation which allows to exactly solve the Ising model and its generalisation to clock models, which instead goes under the name of Fradkin-Kadanoff transformation. The notion of topological order is then introduced and its relevance for topological quantum computation is briefly discussed. The last duality transformation we have decided to present relies on a recently developed formalism known as bond-algebraic approach and links Abelian $\mathbb{Z}_p$ lattice gauge theories on a ladder geometry with p-state clock models with both transverse and longitudinal fields.

The numerical analysis of symmetric and chiral clock models via DMRG calculations with tensor networks may be found in Chapter 4. Here, by investigating these models under several configurations, we focus on the most important observables, namely the energy gap, the entanglement entropy, the magnetisation and the correlation functions, in order to study their scaling behaviour and extract the corresponding critical exponents. The universality classes of most phase transitions are therefore identified and a global picture of the phase diagrams is obtained. A specific discussion is deserved to the topology of the phase diagram of the 3-state

chiral clock model and to the Lifshitz oscillations observed in its energy gap as a function of the system size. Then we add a longitudinal field to these models in order to understand how the phase diagram gets modified. Under the same setup, the duality with lattice gauge theories is numerically explored.

Finally, in the conclusions we review the main results we have achieved and try to outline some pathways for possible future research about these topics.

More technical considerations about the computational tools we have used throughout this dissertation are listed in Appendix A.

1

Critical phenomena: an overview

In this chapter we recall the main features of critical phenomena in one-dimensional quantum systems at the equilibrium. We do not intend to be exhaustive, but simply to review the most important theoretical aspects which we are going to take advantage of for the study of p-state clock models in the next chapters.

Thus, we start by reviewing the field theoretical background behind critical phenomena by presenting the correspondence between statistical mechanics and quantum field theory. Afterwards, we define and recall the main characteristics of quantum phase transitions, focusing on continuous ones with some examples. In particular we focus on Berezinskii-Kosterlitz-Thouless transitions which are the paradigmatic example of infinite order phase transitions. We end the chapter with a more detailed study of the quantum Ising model.

1.1 Field theoretical background

We think worth opening this chapter by presenting an idea which we will extensively exploit all along the next sections: the correspondence between equilibrium statistical systems and quantum field theories near criticality [18, 20]. Let us consider a quantum mechanical system with time-independent Hamiltonian $\mathcal{H}$, which may be either relativistic or not, but we now stick to the non-relativistic case for the sake of simplicity. The time evolution of this system is expressed by the time-

evolution operator

$$U(t,t') = \exp\left\{-\frac{i}{\hbar}\mathcal{H}\ (t-t')\right\} \tag{1.1}$$

which acts on the wave function at time t and makes it evolve to the time t', formally $\psi(t') = U(t,t')\psi(t)$. Assuming $t - t' \ll 1$, we may derive a path integral expression for the generating functional. We will not go through the formal derivation of it, as we are only interested in the physical intuition. However, we stress that the path integral derivation represents an alternative way in quantum mechanics for passing from the Hamiltonian to the Lagrangian beside the standard Legendre transform [26]. Indeed the final expression for the generating functional reads

$$\mathcal{Z} = \int dx_i \prod_i U(t_{i+1}, t_i) = \int Dx \exp\left(-\frac{i}{\hbar}S\right) \tag{1.2}$$

where $S(t_1,t_2) = \int_{t_1}^{t_2} dt\mathcal{L}$ is the classical action, with $\mathcal{L}$ the classical Lagrangian, and $\int Dx$ is a symbolic way of writing the path integral indicating the sum over all paths in (x,t)-space. If instead we consider a statistical mechanical system, for example a spin system in d dimensions (a temporal one and $d-1$ space ones), being τ_1, τ_2 two instants of time and $\underline{\sigma}(\tau_1), \underline{\sigma}(\tau_2)$ the corresponding spin configurations, we may introduce the *transfer matrix* $\mathcal{T}$, which is defined by having elements

$$\langle \underline{\sigma}(\tau_1)|\mathcal{T}|\underline{\sigma}(\tau_2)\rangle = \exp\left(\frac{1}{k_B T}h(\tau_1,\tau_2)\right)\ , \tag{1.3}$$

where $\mathcal{H} = \sum_\tau h(\tau, \tau+1)$ is the classical Hamiltonian. Then the partition function of the system reads

$$\mathcal{Z} = \sum_{\underline{\sigma}_1,\ldots,\underline{\sigma}_m} \exp\left(-\frac{1}{k_B T}\mathcal{H}\right) = \mathrm{Tr}\,\mathcal{T}^m \tag{1.4}$$

being m the number of sites along the temporal direction, assuming our systems to live on a $m \times n$ lattice. The strong formal analogies between the two descriptions suggest to interpret $\mathcal{T}$ as an Euclidean time-evolution operator, i.e.

$$\mathcal{T} = \exp\left(-\tau H\right) \tag{1.5}$$

where now H is the quantum Hamiltonian. Thus, the eigenstates of the transfer matrix correspond to the energy eigenstates: let us call Λ_r the 2^n eingenvalues of $\mathcal{T}$ and E_r the corresponding eigenvalues of H, we have

$$E_r = -\frac{1}{a}\ln(\Lambda_r)\ , \tag{1.6}$$

being a the lattice spacing. This also comes along with other identifications, for example between the real time t and the Euclidean time $-i\tau$, between the generating functional and the partition function and of course between the time-evolution operator and the transfer matrix. Thus, we see that we are able to build a map between a classical system in d dimensions and a quantum one in $(d-1)$ dimensions. We stress that this map is highly non-trivial as in the former case we have classical commuting variables, whereas in the latter case the variables are quantum, i.e. non-commuting. Moreover, this correspondence between statistical systems and quantum field theories allows us to indifferently speak about equilibrium state and ground state, ensemble average and ground state expectation value, inverse correlation length (or mass) and energy gap, and so on. Indeed, being $\hat{\sigma}$ the spin operator, the ensemble average of the magnetisation $\langle \sigma_{ij} \rangle$ may be computed as

$$\langle \sigma_{11} \rangle = \lim_{m \to \infty} \left(\mathrm{Tr}\, \mathcal{T}^m \right)^{-1} \mathrm{Tr}\, \left(\hat{\sigma} \mathcal{T}^m \right) \tag{1.7}$$

$$= \lim_{m \to \infty} e^{-ma(E_1 - E_0)} \sum_l \langle 0 | \hat{\sigma}_1 | l \rangle \tag{1.8}$$

$$= \langle 0 | \hat{\sigma}_1 | 0 \rangle \ , \tag{1.9}$$

where in the last step we have used the identities $\sum_l |l\rangle\langle l| = \mathbb{1}$ and $\langle 0|l\rangle = \delta_{0,l}$. The energy gap $E_1 - E_0$ entering the previous formula represents the energy of a particle at rest, i.e. its mass. Consequently, we may introduce the correlation length

$$\xi = \frac{1}{ma} \ , \tag{1.10}$$

whose divergence at criticality - which we are going to discuss in the next section - implies the vanishing of the mass. In this sense we will say that statistical systems at criticality correspond to massless quantum field theories.

Finally, we also mention that $\beta = 1/(k_B T)$ and $1/\hbar$ parameterise thermal and quantum fluctuations, which are responsible for driving classical and quantum phase transitions, respectively.

1.2 Quantum phase transitions

For classical systems thermal fluctuations are responsible for classical phase transitions, which may then occur only at non-zero temperature. On the contrary, quantum phase transitions (QPTs) are driven by quantum fluctuations which do occur even at zero temperature due to the Heisenberg uncertainty principle. More formally, quantum phase transitions are points of non-analiticity of the ground

state energy of the system with respect to the coupling of the external field. Let us consider an Hamiltonian having the form

$$H(\lambda) = H_0 + \lambda H_1 \ . \tag{1.11}$$

for some parameter λ. The eigenvalues of H_0 and H_1 - whether they commute or not, if they do they are also simultaneously diagonalisable - are λ-dependent. Two possible scenarios show up: either there is no level-crossing between the ground state and the first excited state, thus no phase transition occurs and the energy spectrum of the system remains gapped, or there is a point of non-analiticity occurring for some $\lambda = \lambda_c$, which may either be a point of level-crossing or the limiting case of an avoided level-crossing [69].

In this dissertation we are going to focus mostly on the so called *continuous* quantum phase transitions, which are characterised by the vanishing of the energy gap, the divergence of the correlation length and of the entanglement entropy and the power-law decay of the correlators at criticality. Thus, these observables separately provide useful pieces of information which all together may be used to detect the presence of a phase transition of this kind.

1.2.1 Observables at criticality

Let us now discuss more in detail how the most relevant physical observables behave in a vicinity of a point of second order phase transition.

Energy gap and correlation length. The closing of the energy gap implies that we may have excitations with arbitrarily low energy and thus a qualitative change in the nature of the system takes place. As we approach criticality, the gap ΔE is known to close as

$$\Delta E \sim J|\lambda - \lambda_c|^{z\nu} \ , \tag{1.12}$$

for some proportionality constant J having the dimension of an energy. The exponent ν is a universal *critical exponent*, as we will clarify later on, and z is the *dynamical critical exponent*. We stress that this behaviour holds true even for $\lambda \geq \lambda_c$ and $\lambda \leq \lambda_c$ with the same exponent, but with different and non-universal proportionality constant (*velocity*).

At a point of quantum phase transition, the correlation length - the characteristic length scale of the fluctuations of the system - diverges as

$$\xi^{-1} \sim \Lambda|\lambda - \lambda_c|^{\nu} \tag{1.13}$$

for some proportionality constant Λ having the dimension of an inverse length. As the exponents governing the scaling of the energy gap and the correlation length are the same, by comparing the two previous expressions we immediately find the following relation:

$$\Delta E \sim \xi^{-z} \,. \tag{1.14}$$

As an aside, we stress that the vanishing of the correlation length at criticality implies that the theory is scale invariant. If it is also Lorentz invariant, the theory is then said to be *conformally* invariant, which is plenty of geometrical consequences. We do not intend to present all the machinery of Conformal Field Theory (CFT) as this would go beyond the scope of this dissertation. We simply clarify that conformal invariance is the symmetry under local (i.e. position-dependent) dilatations. For classical systems in two dimensions, or equivalently quantum systems in one dimension, conformal symmetry becomes extremely rich as here there exist infinitely many locally conformal coordinate transformations. A crucial object emerging within this framework is then the *central charge*, c, sometimes also called *conformal anomaly*, as it is related to a soft breaking of conformal symmetry by the introduction of a macroscopic scale into the system [18]. The central charge is strictly model-dependent and thus it plays an important role in the context of universality and finite-size scaling, as we will see in the next sections.

Entanglement entropy. Another useful physical observable to detect quantum phase transitions is the entanglement entropy, which deserves a separate and broader discussion.

Quantum entanglement is one of the most intriguing and counter-intuitive phenomena of quantum mechanics, as it is responsible for the violation of the locality principle. Given two entangled particles, the measurement of the properties of one particle may instantaneously affect the outcome of the measurement performed on the other particle, arbitrarily far away. In this sense, entanglement describes non-local quantum correlations and it also shares a deep connection with quantum phase transitions. Indeed, in the framework of quantum many-body systems, by measuring the degree of entanglement between two regions of the system, the entanglement entropy provides extremely useful information both about the location of the critical points and the nature of the phase transitions themselves [11].

Let us consider a system with density matrix ρ and let us take it in a pure quantum state $|\psi\rangle$ so that $\rho = |\psi\rangle\langle\psi|$. Then, let us partition the system into two regions, namely A and B, so that the total Hilbert space reads $\mathcal{H} = \mathcal{H}_A \otimes \mathcal{H}_B$ and

the reduced density matrix of the subsystems A and B is $\rho_{A,B} = \mathrm{Tr}_{B,A}\,\rho$. Thus, the entanglement entropy is the von Neumann entropy of either subsystem, formally

$$S_A = -\,\mathrm{Tr}\,(\rho_A \ln \rho_A) = -\,\mathrm{Tr}\,(\rho_B \ln \rho_B) = S_B\ . \tag{1.15}$$

We stress that the equality $S_A = S_B$ holds true only when the system is in a pure quantum state. On the contrary, when the state is mixed the entanglement entropy is no longer a good quantity to measure the degree of entanglement between the two subsystems, as it would mix classical and quantum correlations and its definition would overlap with the one of the thermodynamic entropy.

For our purposes, we are interested in how the entanglement entropy behaves at criticality. As already anticipated, it diverges at a quantum critical point so providing useful information about its location. Moreover, the entanglement entropy is infinite all within gapless phases, thus it may also be used to understand whether a phase is gapped or gapless, and therefore critical [11].

We defer the discussion about the universal scaling of the entanglement entropy to the specific section about finite-size scaling.

Correlation functions. In order to investigate the phase diagram of a system correlation functions are also extremely useful. In spin systems, they measure the degree of alignment between two spins at a given distance r. The closer the spins are, the more they tend to be correlated and the length scale describing their correlation is given by the correlation length. More quantitatively, at distances much larger than the lattice spacing a, the asymptotic behaviour of the correlation functions $G(r)$ away from criticality is given by

$$G(r) \sim \exp\left(-\frac{|r|}{\xi}\right) \quad \text{for} \quad r \gg a\ , \quad h \neq h_c\ . \tag{1.16}$$

It decays exponentially to a finite value G_0 in the ordered phase and to zero in the disordered one.

Instead, at criticality correlation functions display a power-law decay of the form

$$G(r) \sim \frac{1}{|r|^{d-2+\eta}} \quad \text{for} \quad r \gg a\ , \quad h = h_c\ , \tag{1.17}$$

where d is the dimension of the classical system and η is a critical exponent called *anomalous dimension*. Such a behaviour means that at criticality correlations extend to all distance scales, as the correlation length is infinite.

Order and disorder parameter. Another way of distinguishing between two different phases and thus to identify a point of second order phase transition

makes use of the order and disorder parameters. In contrast to the previous observables, these quantities neither diverge nor vanish, but their first derivative suffers a discontinuity across criticality, as they are defined to be zero in a phase and different from zero in the other one. In this sense an order parameter (e.g. the net magnetisation in ferromagnetic spin systems) measures the degree of order across the boundaries between two phases and similarly a disorder parameter measures the degree of disorder.

Consider a quantum system with Hamiltonian $H(\lambda)$ which is symmetric under a group G for any value of the parameter λ, let $|\psi_0(\lambda)\rangle$ be the ground state of the system and let λ_c be the location of a critical point. Then, the order parameter ϕ is defined as

$$\phi = \langle \hat{O} \rangle_0 = \langle \psi_0(\lambda) | \hat{O} | \psi_0(\lambda) \rangle = \begin{cases} 0\,, & \text{if } \lambda > \lambda_c \\ \phi_0 \neq 0\,, & \text{if } \lambda < \lambda_c \end{cases} . \tag{1.18}$$

for some operator $\hat{O}$ which is not invariant under the action of the symmetry group getting spontaneously broken in the ordered phase [23]. A complementary description holds true for the disorder parameter as well, so we omit it.

Strictly speaking, the notion of order parameter arises in the framework of spontaneous symmetry breaking, which we are now going to discuss, even if there exist infinite order phase transitions which do not break any symmetry, as we will see next.

1.2.2 QPTs with Spontaneous Symmetry Breaking (SSB)

As already mentioned, many quantum phase transitions correspond to a change in the global symmetries of the system, which will then host two different phases, one more symmetric than the other. Typically, in ferromagnetic spin systems we have a disordered highly symmetric phase, where the symmetry group leaving the Hamiltonian invariant is a Lie group G, and an ordered less symmetric phase where the Hamiltonian is only invariant under $G_0 \subset G$. When this happens to be the case, we say that the symmetry group G spontaneously breaks down to its subgroup G_0 in the ordered phase and an order parameter - as we have already anticipated - appears. Also, the subgroup G_0 of the broken phase is isomorphic to the little group of the order parameter and the order parameters space is given by the coset space G/G_0 [23]. A similar discussion generalises to discrete symmetries as well. Moreover, we stress that no spontaneous symmetry breaking can take place in finite systems.

Most importantly, the spontaneous breaking of a symmetry comes along with gapless excitations known as *Nambu-Goldston modes*. In the context of magnetic systems, these modes not costing any energy are spin waves.

Despite their widespread, there are some limits - depending on the dimension of the system - to the possibility of having phase transitions associated with the breaking of some symmetry. In this regard, let us state the following theorem [52]:

Mermin-Wagner theorem: *for short-range forces no phase transition involving the breaking of a continuous symmetry may occur in $d < 3$ dimensions at positive temperature, $T > 0$. Instead, if the symmetry is discrete, the same holds true for $d < 2$.*

Thus, $d = 1, 2$ and $d = 1$ respectively are called *lower critical dimensions* as no phase transition can occur below these dimensions. Given the correspondence between classical systems in d dimensions and quantum systems in $(d-1)$ dimensions, the generalisation of this theorem to the quantum case is straightforward.

However, there exist phase transitions occurring below the lower critical dimension in systems having a continuous symmetry. Still, they are not in contrast with the Mermin-Wagner theorem because, despite they are continuous, they do not break any symmetry. The most famous example is the infinite order Berezinskii-Kosterlitz-Thouless transition occurring in the XY model, which is discussed in the next section.

1.2.3 Beyond SSB: BKT transitions and the XY-model

Berezinskii-Kosterlitz-Thouless (BKT) phase transitions were firstly discovered in the two-dimensional classical XY-model by Vadim Berezinskii in 1971 [7, 8] and independently by John M. Kosterlitz and David J. Thouless in 1973 [44], but they are actually ubiquitous in classical two-dimensional systems. In this section we provide a description of these new phase transitions along with a discussion of the XY-model, which - together with the Ising model - will represent our starting point for presenting clock models in the next chapter.

The classical XY-model, or planar rotor model, enjoys a global continuous $O(2)$ symmetry, thus, according to the Mermin-Wagner theorem, in $d < 3$ dimensions long-range order is destroyed by fluctuations of the order parameter. However, this model is known to undergo a phase transition even in two dimensions, which may be explained in terms of a new notion of long-range order - called *quasi long-range order* - which relies on the existence of topological excitations emerging on top of the standard spin-wave excitations.

Let us briefly review some notions of the theory of topological defects in two-

dimensions [13]. The new topological excitations emerging in the XY model - which are called *vortices* - are topological defects, i.e. defects which cannot be made disappear by any continuous deformation of the order parameter, thus they are topologically stable. The characterisation of topological defects and their combination is mathematically formalised within the framework of *homotopy theory* and defects are classified into homotopy classes of the ground state manifold, or order parameter space $\mathcal{M}$. For the XY model $\mathcal{M} = S^1$. Defects belong to the same homotopy class if the mappings of all the paths enclosing them may be continuously deformed into each other and they are labelled by the number of times the paths wrap around a unit circle surrounding the defect. We call this integer quantity *winding number* and we say that the first homotopy group $\pi(\mathcal{M})$. For the XY model $\pi(S^1) = \mathbb{Z}$.

Let us now introduce the XY-model: being $\mathbf{s} \equiv s(\cos\theta, \sin\theta)$ with $\theta \in [0, 2\pi[$ the order parameter, the ladder Hamiltonian of the classical XY-model reads

$$H = -J \sum_{\langle i,j \rangle} \mathbf{s}_i \cdot \mathbf{s}_j = -Js^2 \sum_{\langle i,j \rangle} \cos(\theta_i - \theta_j) \,. \tag{1.19}$$

Thanks to the isomorphism $SO(2) \cong U(1)$ (upon setting $s = 1$), we may equivalently express the order parameter as a complex scalar $\psi = |\psi| e^{i\theta}$ and re-write the Hamiltonian in a field-theoretical language as

$$H = \int d^2x \frac{1}{2} (\nabla\psi)^2 \tag{1.20}$$

which we will also call *action*, following the convention of quantum field theories. Using the definition of the order parameter ψ we may also manipulate the Hamiltonian (1.20) to get an effective field theory for θ, namely

$$H = \frac{\rho_s}{2} \int d^2x (\nabla\theta)^2 \tag{1.21}$$

where we have introduced the *stiffness* or *elasticity modulus* $\rho_s \equiv |\psi|^2$. Thus, in the XY-model vortices are spin configurations such that

$$\oint d\theta = \oint_\Gamma \frac{d\theta}{ds} ds = 2n\pi \,, \quad n = 0, \pm 1, \ldots \tag{1.22}$$

where n is the winding number. There exists a simple heuristic argument - due to Kosterlitz and Thouless - entirely based on thermodynamics considerations which describes how vortices are responsible for driving the system from quasi long-range order to disorder and how to work out an estimate of the critical temperature of this second-order phase transition. Let us consider a vortex with winding number $n = 1$ and let us compute its energy, which is given by the sum of the core energy plus an

elastic contribution. We will neglect the former and compute the latter. From (1.21) by minimising the energy and up to an integration by parts we find

$$\frac{\delta H}{\delta \theta} = -\rho_s \nabla^2 \theta = 0 \quad \Rightarrow \quad \nabla^2 \theta = 0 \tag{1.23}$$

which is solved by

$$\theta = n\phi \quad \text{with} \quad \mathbf{v}_s \equiv \nabla\theta = \frac{n}{r}\mathbf{e}_\phi \tag{1.24}$$

where we have introduced the polar angle $\phi = \tan(y/x)$ and the radius $r = \sqrt{x^2+y^2}$, as we are working on the (x,y)-plane. The computation of the elastic energy of the vortex is then straightforward,

$$E_{el} = \frac{\rho_s}{2}\int_D d^2x \mathbf{v}_s^2 = \frac{\rho}{2} 2\pi n^2 \int_a^R \frac{drr}{r^2} = \pi n^2 \rho_s \ln\left(\frac{R}{a}\right) \tag{1.25}$$

where D is the domain of the sample deprived of the vortex core and of the "infinity", a is the core radius of the vortex, R the linear dimension of the sample with the vortex inside and $n = 1$ in our example. Now we need to evaluate the entropy, which may be estimated as follows: imagine to cover the sample with many vortices all with the same core radius a and count the number of possible configurations, Γ. This will be proportional to the ratio between the area of the sample and the area of a single vortex, i.e.

$$\Gamma \sim \frac{\pi R^2}{\pi a^2} = \left(\frac{R}{a}\right)^2 \tag{1.26}$$

so the entropy is given by $S = k_B \ln\Gamma = 2k_B \ln\left(\frac{R}{a}\right)$. At this point we have all the ingredients to compute the free energy of the system, which reads

$$F_{el} = E_{el} - TS = (\pi\rho_s - 2k_B T)\ln\left(\frac{R}{a}\right). \tag{1.27}$$

From this equation we infer that for $k_B T > \frac{\pi\rho_s}{2}$ the energy dominates favouring an ordered configuration against vortices, which are then energetically suppressed and they tend to bind into vortex and anti-vortex pairs, as the energy of two vortices is proportional to $(n_1^2 + n_2^2)$. Instead, for $k_B T < \frac{\pi\rho_s}{2}$ the entropy dominates favouring a disordered configuration and the vortex unbinding or proliferation. Thus, the critical temperature at which the phase transition occurs is given by

$$T_{BKT} = \frac{\pi\rho_s}{2k_B} \tag{1.28}$$

which is the same result one would obtain by deriving it rigorously via renormalisation group analysis [38, 70].

Before concluding, we mention - without going through the formal derivation - what is the main phenomenological feature of BKT transitions: the peculiar behaviour of the correlation length at $T = T_{BKT}$. In contrast to the usual algebraic divergence typically occurring at points of second order phase transition, when the transition is BKT the divergence of the correlation length is much faster and it gets infinite like

$$\xi(T_{BKT}) \sim \exp\left(\frac{A}{\sqrt{T - T_{BKT}}}\right) \tag{1.29}$$

for some constant A, as we approach criticality from above.

1.3 Critical exponents and universality classes

The proper theoretical framework for describing how statistical systems behave at criticality is the renormalisation group (RG), which allows for a clear understanding of scaling laws and *universality*. Indeed, as we have anticipated, close to a phase transition the thermodynamic observables describing the system display a characteristic power-law behaviour which may be parametrised by a set of *critical exponents*, some of which we have already encountered in the previous sections. Assuming that we have already chosen a path to approach the critical field h_c, any observable f will depend only on the *reduced field* $\epsilon \equiv 1 - h/h_c$, namely $f \equiv f(\epsilon)$. We define the critical exponent λ_f associated with f as [23, 54]

$$\lambda_f \equiv \lim_{\epsilon \to 0} \frac{\ln f(\epsilon)}{\ln |\epsilon|} , \tag{1.30}$$

so that, if $\lambda_f \neq 0$, when $\epsilon \to 0$

$$f(\epsilon) \sim |\epsilon|^{\lambda_f} g(\epsilon) \quad \text{with} \quad g(0) \neq 0 . \tag{1.31}$$

Always having in mind magnetic systems, in Tab.1.1 we list the critical exponents of the most important thermodynamic observables which are defined by their behaviour close to criticality.

The exponents $\alpha, \beta, \gamma, \delta$ and ν we have just introduced are not all independent, in fact they satisfy the following algebraic relations:

$$\alpha + 2\beta + \gamma = 2 \qquad \text{(Rushbrooke [24, 68])} \tag{1.32}$$

$$\alpha + \beta\delta + \beta = 2 \qquad \text{(Griffits [33])} \tag{1.33}$$

$$\nu(2 - \eta) = \gamma \qquad \text{(Fisher [27])} \tag{1.34}$$

$$\alpha + \nu d = 2 \qquad \text{(Josephson [39, 40, 76])} . \tag{1.35}$$

Observable	Scaling and critical exponent
Specific heat	$C \sim A\|\epsilon\|^{-\alpha}$
Magnetisation	$M \sim B\|\epsilon\|^{\beta}$
Susceptibility	$\chi \sim C\|\epsilon\|^{-\gamma}$
Correlation length	$\xi \sim \Lambda\|\epsilon\|^{-\nu}$
Correlation function	$G(r) \sim r^{2-d-\eta}$
Incommensurate wave vector	$k \sim D\|\epsilon\|^{\bar{\beta}}$

Table 1.1: Incomplete list of critical exponents.

To be more precise, all these relations between critical exponents were historically discovered as inequalities, but under the Widom scaling hypothesis [83] one can prove that they all reduce to the above exact equalities [23]. Thus, knowing only two of these critical exponents is enough to determine all the other ones. As an aside, the existence of these relations between the critical exponents justifies the scaling relations of the thermodynamic observables which are discussed in the next section.

Another striking observation - which is also justified on the experimental ground - is that critical exponents depend only on the symmetries of the Hamiltonian and the dimension of the system. In this sense they are universal and allow for a classification of phase transitions into *universality classes* independently of the microscopic details [23, 54].

We end this section by listing the main universality classes we are going to encounter in this dissertation along with their critical exponents and central charges, namely Ising, 3-Potts, 4-Potts, Pokrovsky-Talapov, Berezinskii-Kosterlitz-Thouless and chiral. We provide a schematic descriptions in Tab.1.2 along with the main critical exponents and the central charge. We have also reported the nominal values of the dynamical exponents z for these universality classes. We stress that a non-unitary value of the dynamical exponent implies that the underlying quantum field theory is not Lorentz invariant and therefore non-conformal. We defer more detailed considerations to the last chapter.

	α	β	γ	δ	ν	η	$\overline{\beta}$	z	c
Ising	0	1/8	7/4	15	1	1/4	?	1	1/2
3-Potts	1/3	1/9	13/9	14	5/6	4/15	5/3	1	4/5
4-Potts	2/3	1/12	7/6	15	2/3	1/4	?	1	1
Pokrovsky-Talapov	1/2	?	?	?	1/2	$2/p^2$ *	1/2	2	?
BKT	-	-	-	-	-	1/4	-	1	1
Chiral	1/3	?	?	?	2/3	?	2/3	3/2	?

Table 1.2: Incomplete list of universality classes in $d = 2$ dimensions (classical systems). The main critical exponents are reported along with the dynamical exponents and the central charges. We have denoted by (?) those critical exponents whose value is not analytically known and by (-) those which are not defined for that particular universality class. * being p the order of the clock model.

1.4 Finite-size scaling

Finite-size scaling describes finite-size effects arising when a statistical system is confined in a finite geometry, for example a chain or a lattice with a given number of sites. The most important implication is that no phase transition may occur under these conditions. Thus, the energy gap does not close, the correlation length and the entanglement entropy do not diverge, but the singularities appear rounded and shifted with respect to the nominal values of the thermodynamic limit [12, 18, 28].

So let h be the magnitude of the transverse field applied to a one-dimensional spin system (in a classical setup this would be the temperature T) and let us consider a thermodynamic observable O, which can be for example the specific heat or the magnetic susceptibility, but the following discussion holds true on a general ground for every thermodynamic observable. The curves of O will display a maximum at some value $h_c(L)$ which is shifted away from $h_c(\infty) \equiv h_c$, at which the phase transition occurs in the thermodynamic limit. Thus, the finite-size shift amounts to

$$\frac{h_c(L) - h_c(\infty)}{h_c(\infty)} \sim L^{-\lambda} \quad \text{as} \quad L \to \infty \,, \tag{1.36}$$

where λ is the *shift exponent*.

Similarly, we may define the *rounding field* $h^*(L)$ such that if

$$\frac{|h - h_c|}{h_c} \geq \frac{|h^* - h_c|}{h_c} \tag{1.37}$$

then the finite-size O is close to its bulk value, formally $O(L;h) \simeq O(\infty;h)$. This defines the *rounding exponent* θ as

$$\frac{h^*(L) - h_c(\infty)}{h_c(\infty)} \sim L^{-\theta} \quad \text{as} \quad L \to \infty \,. \tag{1.38}$$

The basic hypothesis of finite-size scaling states that there should be only one relevant length describing the rounding and shifting of the singularities. Thus, the correlation length in the thermodynamic limit goes like

$$\xi(h^*(L)) \sim L \tag{1.39}$$

and recalling that $\xi_\infty \sim (h - h_c)^{-\nu}$, we immediately find that the rounding exponent equals the inverse of the critical exponent ν, i.e. $\theta = 1/\nu$. Going through very similar steps, we find that $\lambda = 1/\nu$ as well.

Let us now consider a specific example, namely the scaling of the magnetisation, M. We introduce the scaling variable

$$\tilde{z} \equiv \frac{L}{\xi_\infty(h)} \tag{1.40}$$

and define the *finite-size scaling region* as the region where $\tilde{z}$ is finite. Recalling that in the thermodynamic limit $M \sim |\epsilon|^\beta$, one may postulate that in the finite-size scaling limit

$$L \to \infty, \quad h \to h_c \quad \text{with} \quad \tilde{z} \equiv \frac{L}{\xi(h)} \quad \text{fixed} \,. \tag{1.41}$$

Thus, one may write the magnetisation in the form

$$M(L;h) \sim L^\omega \tilde{Q}(\tilde{z}) \sim L^\omega \tilde{Q}(L^{\frac{1}{\nu}}\epsilon) \tag{1.42}$$

where $\tilde{Q}$ is a universal function. Finally, in order to reproduce the bulk behaviour in the limit $\tilde{z} \gg 1$, we do the following ansatz for the scaling function:

$$\tilde{Q}(\tilde{x}) \sim q_\infty^\pm \tilde{x}^{-\rho} \quad \text{when} \quad \tilde{x} \to \pm\infty \tag{1.43}$$

and then by matching $\omega = \rho/\nu$ and $\rho = -\beta$, we find

$$M(L;h) \sim L^{-\frac{\beta}{\nu}} \tilde{Q}(L^{\frac{1}{\nu}}\epsilon) \tag{1.44}$$

or equivalently

$$M(L;h^*) \sim L^{-\frac{\beta}{\nu}} \tilde{Q}(\tilde{z}) \tag{1.45}$$

with $\tilde{Q}(\tilde{z})$ finite and different from zero for $0 \leq \tilde{z} \leq 1$, so that

$$M(L; h_c(h)) \sim L^{-\frac{\beta}{\nu}} . \tag{1.46}$$

We stress again that despite we have focused on the magnetisation as a specific example, a very similar discussion holds true every thermodynamic quantity, each one with its own critical exponents. In this regard we list the finite-size scaling of the most relevant thermodynamic quantities close to a point of second order phase transition with $\tilde{z} = 0$:

(i) Specific heat: $C \sim L^{\frac{\alpha}{\nu}}$;

(ii) Magnetic susceptibility: $\chi \sim L^{\frac{\gamma}{\nu}}$;

(iii) Order parameter/magnetisation: $M \sim L^{-\frac{\beta}{\nu}}$;

(iv) Correlation length: $\xi \sim L$;

(v) Free energy density: $f \sim L^{-d}$.

The finite-size scaling of the entanglement entropy deserves instead a separate discussion. When periodic boundary conditions are enforced on a chain of length L, the entanglement entropy of a sub-chain of length ℓ scales according to the Calabrese-Cardy formula [11]

$$S_{PBC}(L; \ell) = \frac{c}{3} \ln \left[\frac{L}{\pi} \sin \left(\frac{\pi \ell}{L} \right) \right] + S_0 \tag{1.47}$$

where c is the central charge and S_0 is a non-universal constant. On the other hand, when open boundary conditions are enforced, the entanglement entropy scales as [11]

$$S_{OBC}(L; \ell) = \frac{c}{6} \ln \left[\frac{2L}{\pi} \sin \left(\frac{\pi \ell}{L} \right) \right] + S_0 \tag{1.48}$$

which is again proportional to the central charge c and has an extra piece S_0 which now includes both the boundary entropy and a non-universal constant. Thus, the study of the logarithmic scaling of the entanglement entropy is crucial in the theory of critical phenomena, as it provides the central charge of the underlying conformal theory, which may be used to identify the nature of the phase transition the system is undergoing.

1.5 The quantum Ising model

We end this chapter by discussing one of the simplest statistical models hosting a second order phase transition: the Ising model[1]. In its classical version, it was firstly studied and solved in one dimension by Ernst Ising in 1925 [37], whom it is named after. Moreover, it is also one of the very few examples of statistical models which are integrable and therefore exactly solvable even in two-dimensions, as it was firstly proved by Lars Onsager in 1944 [59].

The Hamiltonian of the one-dimensional quantum Ising model on a chain of length L with open boundary conditions (OBC) is

$$H = -J \sum_{i=1}^{L-1} \sigma_i^z \sigma_{i+1}^z - h \sum_{i=1}^{L} \sigma_i^x \tag{1.49}$$

where the first term describes the exchange interaction energy between nearest-neighbours spins with coupling constant $J > 0$, enforcing a ferromagnetic interaction along the z-direction. The second term describes a transverse magnetic field along the x-direction with magnitude $h \geq 0$ which tends to break the $\mathbb{Z}_2$ symmetry of the model along with the magnetic order. Instead σ_i^x, σ_i^z are operators acting on the i-th site of the chain and they are defined as

$$\sigma_i^a = \underbrace{\mathbb{1}_2 \otimes \cdots \otimes \mathbb{1}_2}_{(i-1) \text{ times}} \otimes \sigma^a \otimes \underbrace{\mathbb{1}_2 \otimes \cdots \otimes \mathbb{1}_2}_{(L-i) \text{ times}} \quad \text{with} \quad a = x, y, z \,, \tag{1.50}$$

where σ^x, σ^z are two Pauli operators. We recall that, upon choosing a suitable orthonormal basis, these operators may be realised as the following 2×2 hermitian matrices

$$\sigma^x = \begin{pmatrix} 0 & 1 \\ 1 & 0 \end{pmatrix} \,, \quad \sigma^y = \begin{pmatrix} 0 & -i \\ i & 0 \end{pmatrix} \,, \quad \sigma^z = \begin{pmatrix} 1 & 0 \\ 0 & -1 \end{pmatrix} \,. \tag{1.51}$$

It is well-known that the Pauli operators obey a non-trivial algebra which is given by the following commutation and anti-commutation relations

$$[\sigma^a, \sigma^b] = 2i\epsilon_c^{ab} \sigma^c \quad \text{and} \quad \{\sigma^a, \sigma^b\} = 2\delta^{ab} \mathbb{1}_2 \,, \tag{1.52}$$

where ϵ_c^{ab} is the Levi-Civita anti-symmetric tensor, δ^{ab} the Kronecker symbol and the indices take values $a, b, c = x, y, z$. In our notation, we have non-trivial relations only when the Pauli operators are defined on the same site, otherwise on different

[1] For our purposes, we focus only on its one-dimensional quantum version, which may also be derived from the classical one via the transfer matrix method (see for example Ref.[30, 54]).

sites they commute. The operator σ_i^z has eigenvalues ± 1 and eigenstates which we may denote as

$$|\uparrow\rangle_i \equiv |0\rangle_i = \begin{pmatrix} 1 \\ 0 \end{pmatrix}_i \quad \text{and} \quad |\downarrow\rangle_i \equiv |1\rangle_i = \begin{pmatrix} 0 \\ 1 \end{pmatrix}_i \tag{1.53}$$

describing the states with spin up and down, respectively.

Now that we have clarified the notation, we can start studying the quantitative properties of the phase diagram of the quantum Ising model [69]. The ground state of the system depends upon the magnitude of the transverse field h, so it is useful to distinguish between two different regimes: $h \gg 1$ and $h \ll 1$, which correspond to the classical high- and low-temperature limits, respectively. When $h \gg 1$, the transverse field along the x-direction wins against the exchange interaction term, thus spoiling the magnetic order along the z-direction and favouring a random spin configuration, which we will call *paramagnetic phase* or *quantum paramagnet*. So if we denote by

$$|\rightarrow\rangle_i = \frac{1}{\sqrt{2}}\left(|\uparrow\rangle_i + |\downarrow\rangle_i\right) \quad \text{and} \quad |\leftarrow\rangle_i = \frac{1}{\sqrt{2}}\left(|\uparrow\rangle_i - |\downarrow\rangle_i\right) \tag{1.54}$$

the eigenstates of σ_i^x with corresponding eigenvalues ± 1, the ground state in the asymptotic limit $h = 0$ reads

$$|GS\rangle = \prod_i |\rightarrow\rangle_i \ . \tag{1.55}$$

We also notice that the zero-order ground state correlator is given by $\langle \sigma_i^z \sigma_j^z \rangle = \delta_{ij}$ as the operators at different sites $i \neq j$ are completely uncorrelated. But when the transverse field is strong but finite, perturbative corrections produce correlations which are expected to remain short-ranged at large distances, i.e. we expect

$$\langle \sigma_i^z \sigma_j^z \rangle \sim e^{-|x_i - x_j|/\xi}, \quad \text{for} \quad |x_i - x_j| \gg 1 \ , \tag{1.56}$$

where ξ is the correlation length, so this picture is consistent with the expected behaviour of the correlation function away from criticality which we have previously described in the specific section.

Instead, in the limit of weak field $h \ll 1$, the first term in (1.49) now dominates forcing a configuration, which we will call ordered *ferromagnetic phase*, where all the spins tend to be aligned, either up or down, formally

$$|\uparrow\rangle = \prod_i |\uparrow\rangle_i \quad \text{and} \quad |\downarrow\rangle = \prod_i |\downarrow\rangle_i \ . \tag{1.57}$$

Strictly speaking, this holds true for $h = 0$, but it may be considered approximately true when the transverse field is weak, i.e. $h \ll 1$. Thus, we see that there is a clear qualitative change in the nature of the ground state of the system when passing from one regime to the other, this providing strong evidences supporting the hypothesis of a phase transition occurring at some $h = h_c$ in between. Such phase transition is second-order in nature and it is triggered by a mechanism of spontaneous symmetry breaking.

The Ising model indeed enjoys a discrete global $\mathbb{Z}_2$ symmetry generated by the unitary operator

$$\mathcal{O} = \prod_{i=1}^{L} \sigma^x \tag{1.58}$$

which acts by sending σ^z into $-\sigma^z$, thus leaving the Hamiltonian invariant when the transverse field is switched off, i.e. when $h = 0$. Moreover, we have already anticipated that the ground state is twofold degenerate, as it consists in a configuration in which the spins are all aligned, either up-ward or down-ward. Therefore the system will choose either one configuration or the other, thus breaking the $\mathbb{Z}_2$ symmetry. This also defines an order parameter as

$$\langle \sigma_i^z \rangle = \pm M \neq 0 \tag{1.59}$$

where the expectation value $\langle \cdot \rangle$ is taken over either of the ground state configurations.

As we approach criticality from above, $h \to h_c^+$, the correlation length diverges, the energy gap closes and the magnetisation decays algebraically to zero. At least this is true in the thermodynamic limit, where the lattice gets infinite, otherwise no phase transition may happen and we need to deal with finite-size effects.

It is also possible to exactly locate the point of second order phase transition at $h_c = 1$ by exploiting the *Kramers-Wannier duality*, which establishes a map between the strong- and weak-field regimes and thus between order and disorder. We will discuss it in detail in the third chapter, along with the *Jordan-Wigner duality*, which instead maps the Ising model into a free fermion model, so providing an easy way to exactly diagonalise the Hamiltonian.

We end this section about the Ising model by briefly discussing what happens to the model if we modify the Hamiltonian (1.49).

By adding a longitudinal field, the Ising Hamiltonian becomes

$$H = -J \sum_{i=1}^{L-1} \sigma_i^z \sigma_{i+1}^z - h_x \sum_{i=1}^{L} \sigma_i^x - h_z \sum_{i=1}^{L} \sigma_i^z \ . \tag{1.60}$$

where now the magnitude of the transverse field is h_x, while h_z is the magnitude of the longitudinal field. The primary effect of adding such a field to the ferromagnetic transverse Ising model is that the singularity at $h = 1$ gets removed, namely no phase transition occurs anymore and the energy spectrum of the model is completely gapped [78]. In addition to that, the presence of a longitudinal field spoils the symmetry between the strong- and weak-field regimes, thus the Kramers-Wannier duality does not hold anymore.

Another possible version of the model is the *chiral Ising model*, which however is not particularly interesting, as no new phases emerge [61]. For this reason we do not present it and postpone the discussion about chirality to the next chapter in the context of p-state chiral clock models.

2

Quantum clock models

In this second chapter we present one-dimensional quantum p-state clock models under different setups. We start by studying the symmetric case with a transverse field only and then we add a longitudinal field as well. We discuss both real and complex coupling constant for the longitudinal field. Then we move on to consider p-state chiral clock models: after having clarified what we mean by chiral, we firstly apply to the model a transverse field and in a second time a longitudinal field as well. We end the chapter by discussing the symmetries of these models, with a special focus on the discrete spacetime symmetries of parity, time reversal and charge conjugation.

2.1 p-state clock models

Quantum p-state clock models historically arise as a generalisation of the transverse Ising model, which indeed is recovered when the clock order $p = 2$. The literature about these models is rich, yet sometimes ambiguous in the naming. Indeed, p-state clock models are also known as $\mathbb{Z}_p$-models, after their symmetry, and as vector or planar Potts models, because a generalisation of the Ising model with $p = 3$ was firstly studied by Renfrey Potts in 1951 [63]. When $p = 4$ the 4-state clock model - or 4-state Potts model - is often referred to as Ashkin-Teller model, named after Julius Ashkin and Edward Teller, who firstly studied an equivalent

model in 1943 [3]. Besides generalising the Ising model, clock models are also strictly related to the XY-model which we have introduced in the previous chapter. More precisely, p-state clock models may be regarded as progressive approximations to the XY-model as p increases and suitably performing the limit $p \to \infty$ the XY-model itself is recovered [22]. This is particularly manifest if we take into account their classical formulation in two dimensions, where the clock Hamiltonian in absence of an external magnetic field ($h = 0$) takes the form

$$H = -J \sum_{\langle i,j \rangle} \cos\left(\theta_i - \theta_j\right) , \tag{2.1}$$

which differs from (1.19) only for the fact that now the angles are discretised,

$$\theta_i = \frac{2\pi n_i}{p} , \quad n_i = 0, 1, \ldots, p-1 . \tag{2.2}$$

Indeed while the classical XY-model can be figured as a lattice with a spin attached at each site, which is able to rotate in the (x, y)-plane, for the classical p-clock model we should imagine to attach at each site a spin which may take only a discrete set of values, like the hand of a clock, hence the name (see Fig.2.1).

However, in what follows we are going to focus only on the one-dimensional quantum version of p-clock models, which one could also formally derive starting from the classical two-dimensional one via the transfer matrix method [5, 50]. So let us introduce the model.

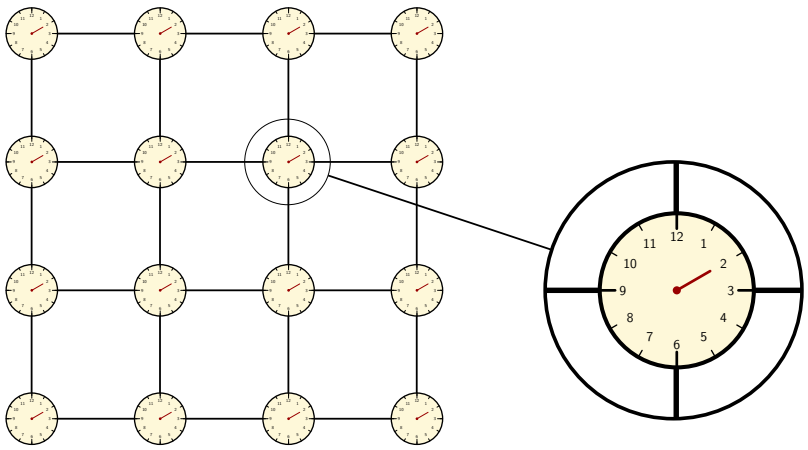

Figure 2.1: Pictorial representation of the classical 12-state clock model on a square lattice.

2.1.1 The model

The Hamiltonian of the one-dimensional quantum p-state clock model on a chain of length L with open boundary conditions reads [60, 77]

$$H = -J \sum_{j=1}^{L-1} \left(Z_j Z_{j+1}^\dagger + Z_{j+1} Z_j^\dagger \right) - h \sum_{j=1}^{L} \left(X_j + X_j^\dagger \right) \tag{2.3}$$

where J and h are real and positive parameters representing the coupling constants of the "kinetic" term and of the transverse field, respectively. X and Z are the unitary operators describing the clock degrees of freedom and they satisfy the following algebra:

$$ZX = \omega XZ, \quad Z^p = X^p = \mathbb{1}, \quad \omega \equiv e^{\frac{2\pi i}{p}}, \tag{2.4}$$

which is a generalisation to arbitrary p's of the Pauli matrix algebra $\sigma^x \sigma^z = e^{\frac{2\pi i}{p}} \sigma^x \sigma^z$, holding for $p = 2$. Thus, each clock degree of freedom lives in a p-dimensional Hilbert space, say $\mathcal{H}_p$, where one can build an orthonormal basis

$$\{|n\rangle \in \mathcal{H}_p,\ n = 0, 1, 2, \dots p-1\} \tag{2.5}$$

such that the clock operators are realised as the following unitary matrices:

$$X = \begin{pmatrix} 1 & 0 & 0 & \dots & 0 \\ 0 & \omega & 0 & \dots & 0 \\ 0 & 0 & \omega^2 & \dots & 0 \\ \vdots & \vdots & \vdots & \ddots & \vdots \\ 0 & 0 & 0 & \dots & \omega^{p-1} \end{pmatrix} \quad \text{and} \quad Z = \begin{pmatrix} 0 & 1 & 0 & \dots & 0 \\ 0 & 0 & 1 & \dots & 0 \\ \vdots & \vdots & \vdots & \ddots & \vdots \\ 0 & 0 & 0 & \dots & 1 \\ 1 & 0 & 0 & \dots & 0 \end{pmatrix}. \tag{2.6}$$

The X operator acts on the states $|n\rangle$ by extracting a phase, whereas the action of the Z operator results in a counterclockwise rotation in the internal space of clock degrees of freedom from one state to the nearest-neighbour one. Formally:

$$X|n\rangle = |n\rangle \omega^n \quad \text{and} \quad Z|n\rangle = |n-1\rangle, \tag{2.7}$$

with the convention $Z|0\rangle = |p-1\rangle$. A pictorial representation of the action of the Z operator is sketched in Fig.2.2.

One may then add to the model a longitudinal field as well, so that (2.3) becomes

$$H = -J \sum_{j=1}^{L-1} \left(Z_j Z_{j+1}^\dagger + Z_{j+1} Z_j^\dagger \right) - h_x \sum_{j=1}^{L} \left(X_j + X_j^\dagger \right) - h_z \sum_{j=1}^{L} \left(Z_j + Z_j^\dagger \right) \tag{2.8}$$

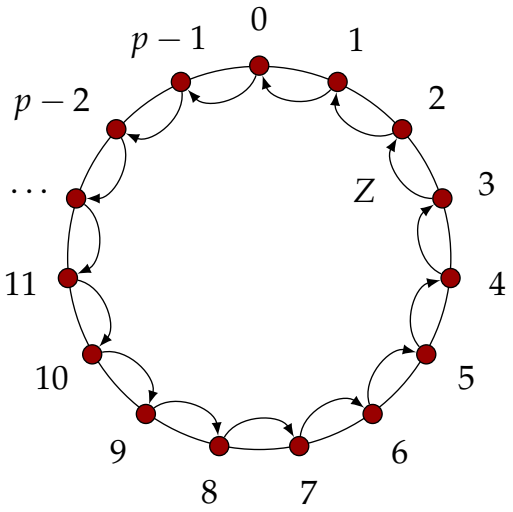

Figure 2.2: Pictorial representation of the action of the Z operator, resulting in a counter-clockwise rotation to the nearest-neighbour state. Similarly, the action of $Z^\dagger$ will result in a clockwise rotation to the nearest-neighbour state.

where we have re-named h_x the magnitude of the transverse field and called h_z that of the longitudinal field.

The last setup we are going to study is that of p-state symmetric clock models with complex longitudinal field, having Hamiltonian

$$H = -Jh \sum_{j=1}^{L-1} \left(Z_j Z_{j+1}^\dagger + Z_{j+1} Z_j^\dagger \right) - \sum_{j=1}^{L} \left(X_j + X_j^\dagger \right) + \\ - h \sum_{j=1}^{L} \left(Z_j (1 + \omega^n) + (1 + \omega^{n*}) Z_j^\dagger \right) , \tag{2.9}$$

were $\omega \equiv \exp(2\pi i/p)$ and $n = 0, 1, \ldots, p-1$ is a term keeping memory of the topological sector of the dual lattice gauge theory, as we will discuss in the third chapter.

We notice that despite the presence of a complex coupling, this model is not chiral in the sense we are going to clarify in the next section, thus it can rightfully be discussed in the present section.

2.1.2 Phase diagram

The basic topology of the phase diagram of transverse p-state clock models, at least in their classical formulation, is well known since the late seventies of the previous century [22] . When $p \leq 4$ these models are characterised by two gapped phases separated by a second order phase transition occurring at $h = h_c$. Thanks to self-duality considerations which will be clarified in the next chapter, we are able

to locate the critical point at $h_c = 1$, just like the Ising model. Thus, for $h < 1$ (low temperature regime) the system is in a ferromagnetic phase which is characterised by long-range order and by the breakdown of the $\mathbb{Z}_p$ symmetry. Instead, when $h > 1$ (high temperature regime) the system enters a disordered paramagnetic phase where the $\mathbb{Z}_p$ symmetry is restored. For a more exhaustive discussion, it is useful to characterise these phases in the language of $\mathbb{Z}_p$ discrete gauge models as well [22]. In this sense, we may also say that the low temperature phase is Higgs-type and deconfined, with Wilson loops displaying a perimeter law behaviour, whereas the high temperature phase is Coulomb-type and confined, with Wilson loops displaying an area law behaviour. We will go back to discuss the relation between lattice gauge theories and clock models in the next chapters.

According to the literature when $p \geq 5$ clock models seem to support a third phase of Berezinskii-Kosterlitz-Thouless type opening symmetrically around the critical point $h_c = 1$ [60]. This new critical phase is characterised by quasi-long-range order along with the power-law decay of the correlators and the loss of exact self-duality. The reason of this discontinuous behaviour when passing from $p \leq 4$ to $p \geq 5$ may be traced to the emergence of a continuous $U(1)$ symmetry together with a new type of excitations appearing on top of the usual domain walls already present for $p \leq 4$. These new excitations are topological in nature as they carry non zero winding number and therefore they may be identified as *discrete vortices*.

Finally, in the limit $p \to \infty$ we recover the continuous XY model, thus the ordered ferromagnetic phase must shrink into a single point, according to the Mermin-Wagner theorem. We also recall that the XY model is not self-dual, this explaining the loss of self-duality starting from $p = 5$.

We summarise all these pieces of information in Fig.2.3. More quantitative considerations about the phase diagram of p-state clock models are postponed to the last chapter where we investigate these models by using numerical techniques as - in contrast to the Ising models - clock models are not exactly solvable.

The presence of a longitudinal field instead modify the topology of the phase diagram, as it tends to align all the spins along its direction. Indeed, at least for $p = 3, 4$, clock models are known to behave like the Ising model, meaning that the longitudinal field immediately dominates over the transverse one as far as it is switched on. So the singularity is removed and the spectrum is completely gapped for any non-zero value of h_z.

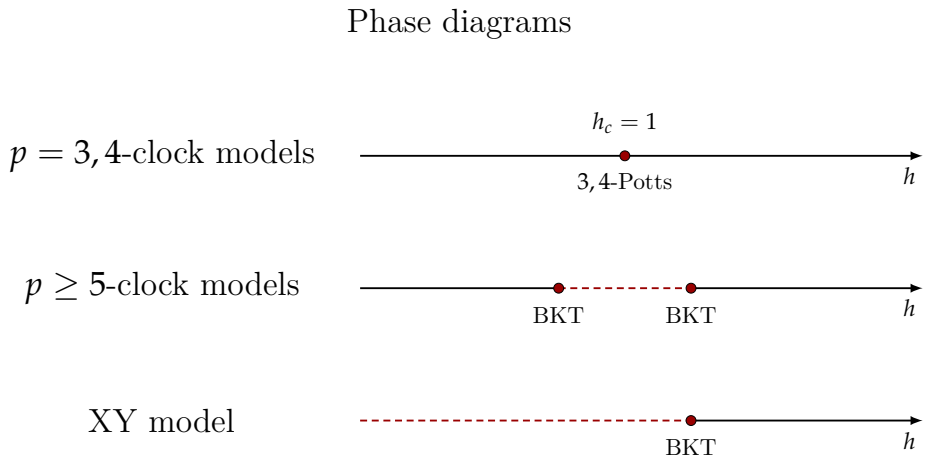

Figure 2.3: Sketch of the phase diagram of p-state clock models for $p \leq 4$ (on top), $p \geq 5$ (in the middle) and phase diagram of the XY model (at the bottom). We draw the gapped phases with smooth black lines and the critical ones with dashed red lines. Red circles represent the points of phase transition.

2.2 p-state chiral clock models

The next models we take into account are one-dimensional quantum p-state chiral clock models. Among the first studies about chiral clock models it is worth mentioning the work carried out by Stellan Ostlund in 1980 [61]. Here he investigated the commensurate-incommensurate (C-IC) transition which occurs each time a commensurate phase with long-range order melts to an incommensurate floating phase. This kind of phase transition naturally arises when introducing an asymmetry in clock models with order $p \geq 3$. No C-IC transition occurs in the chiral Ising model.

Chiral clock models have recently risen in new popularity thanks to the work of Paul Fendley [25] who has shown that parafermionic edge zero modes do appear only in presence of chiral interactions. Moreover, as we will better discuss in the next chapter, one-dimensional $\mathbb{Z}_n$-parafermionic models display topological order with non-Abelian anyonic excitations and thus they may seem promising for topological quantum computing. Unfortunately, they are not sufficient for performing universal quantum computation. Still, this discovery started both theoretical and experimental new research lines in the context of chiral clock models and nowadays the literature in this area is quite rich [49, 71, 82, 85].

In analogy with the previous section, even if we are going to focus only on the quantum version of these models, it may be useful to write down the Hamiltonian of classical chiral clock models as well, which in absence of an external magnetic

field ($h = 0$) reads [61]

$$H = -J \sum_{\langle i,j \rangle} \cos \left[\frac{2\pi}{p} \left(n_i - n_j - \mathbf{R}_{ij} \cdot \mathbf{\Delta} \right) \right] \tag{2.10}$$

where n_i, n_j are integers ranging from 0 up to $p-1$, $\mathbf{R}_{ij} \equiv (\mathbf{R}_i - \mathbf{R}_j)/|\mathbf{R}_i - \mathbf{R}_j|$ is the unit vector between the i-th and j-th sites of the lattice and $\mathbf{\Delta} \equiv \Delta \hat{x}$ is the vector whose magnitude Δ introduces a chirality in the model. Indeed, Δ forces the angle $\theta_i = 2\pi n_i / p$ to undergo a continuous rotation in space, which is in competition with the discrete nature of the angle itself. This competition is the origin of the emerging of a new critical phase which is floating incommensurate in nature.

Before going further and present the quantum version of chiral clock models, let us firstly formalise what do we truly mean by *chiral*.

2.2.1 What does *chiral* mean?

Before formally defining the model, we need to clarify what the word *chiral* means in the present context [25] . We will say that a system or model is chiral if the interaction energy between two spins is not invariant under their interchange. The models we have described in the previous section are defined to have real coupling constants, hence they are always non chiral. Instead, by allowing the couplings to take complex values, we may introduce an asymmetry into the model, which then becomes chiral in the sense we have just defined.

Let us call s_j the spin at site j taking values $1, \omega, \omega^2, \ldots, \omega^{p-1}$, where ω is the usual phase defined as $\omega \equiv e^{\frac{2\pi i}{p}}$. For a 3-state system with chiral phase θ, the energy term reads $s_j^* s_k e^{i\theta}$. When the chirality is absent, i.e. $\theta = 0$, $s_j^* s_k$ may take only three values, namely $1, \omega, \omega^2$ and the situation is sketched in Fig.2.4(a). As the interaction energy between any pair of spins is proportional to the real part of their values, the rightmost point in the figure has the largest real part ($s_j = s_k$) and thus it minimises the energy (because in the Hamiltonian there is a minus sign in front). On the other hand, when $\theta \neq 0$, the situation is sketched in Fig.2.4(b). Now the diagram describing the three values of $s_j^* s_k e^{i\theta}$ gets rotated anticlockwise by θ, as we are assuming $\theta > 0$. As a consequence of this, the rightmost point of the diagram still minimises the energy as it has the largest real part, but now the interaction energy is no longer invariant under the exchange of the spins s_j and s_k. Hence, this model is chiral. However, we stress that if θ is integer multiple of $2\pi/p$ the symmetric configuration is restored, the energy is again invariant under the exchange of two spins and thus the model is no longer chiral, even if it has complex coupling constants.

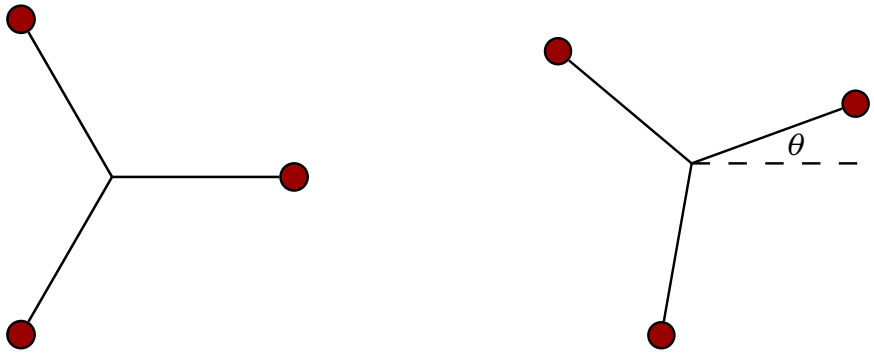

(a) Symmetric case, $\theta = 0$. **(b)** Chiral case, $\theta \neq 0$.

Figure 2.4: Picture of the three possible values of $s_j^* s_k e^{i\theta}$ for $\theta = 0$ (symmetric case, left) and $\theta \neq 0$ (chiral case, right) with clock order $p = 3$.

2.2.2 The model

The Hamiltonian of the one-dimensional quantum p-state chiral clock model with a chain of length L and open boundary conditions is [25, 82]

$$H = -J \sum_{j=1}^{L-1} \left(Z_j Z_{j+1}^\dagger e^{i\theta} + Z_{j+1} Z_j^\dagger e^{-i\theta} \right) - h \sum_{j=1}^{L} \left(X_j e^{i\phi} + X_j^\dagger e^{-i\phi} \right) . \tag{2.11}$$

Now the couplings are complex: θ and ϕ are two chiral phases, while J and h are the moduli of the couplings of the kinetic term and the transverse field, respectively. X and Z are the same unitary operators defined in the symmetric case, so they obey the algebra (2.4). Therefore, one may also find out an orthonormal basis of the Hilbert space in which the clock operators are realised as the same unitary matrices of (2.6), in full analogy with the previous case. We also stress that this model is indeed chiral - unless both the angles are integer multiples of $2\pi/p$ - as one can easily check that the interaction energy between two spins is not invariant under their interchange.

We have mentioned in the previous section that symmetric clock models are not integrable. Similarly, chiral clock models are not exactly solvable either, except for the line $h \cos(p\phi) = J \cos(p\theta)$ which is known to be integrable [25].

Another nice property of the chiral Hamiltonian is that it is left invariant when either of the two phases, θ and ϕ, get shifted by multiples of $\frac{2\pi}{p}$. Indeed, under the transformation

$$\theta \to \theta' = \theta + \frac{2n\pi}{p}, \qquad \phi \to \phi' = \phi + \frac{2m\pi}{p} \tag{2.12}$$

The Hamiltonian gets rephrased as

$$H = -J\omega^{-n} \sum_{j=1}^{L-1} Z_{j+1} Z_j^\dagger e^{-i\theta} - h\omega^{-m} \sum_{j=1}^{L} X_j^\dagger e^{-i\phi} + h.c. \ . \tag{2.13}$$

Now we may redefine the clock operators as

$$X'_j = \omega^{-m} X_j, \quad Z'_{2j} = \omega^{-n} Z_{2j}, \quad Z'_{2j+1} = Z_{2j+1} \tag{2.14}$$

and upon this redefinition we immediately recover the initial Hamiltonian. As an aside, it is important to notice that the previous redefinition is justified by the fact that the new operators preserve the algebra (2.4) and thus they are good clock operators. This has the main advantage of allowing us to restrict to a shorter range of angles within which these models are always chiral, namely $\theta \in [0, \frac{2\pi}{p}[$ and $\phi \in [0, \frac{2\pi}{p}[$.

By adding also a longitudinal field, the Hamiltonian gets modified from (2.11) to

$$\begin{aligned} H = -J \sum_{j=1}^{L-1} \left(Z_j Z_{j+1}^\dagger e^{i\theta} + Z_{j+1} Z_j^\dagger e^{-i\theta} \right) - h_x \sum_{j=1}^{L} \left(X_j e^{i\phi} + X_j^\dagger e^{-i\phi} \right) + \\ - h_z \sum_{j=1}^{L} \left(Z_j + Z_j^\dagger \right) \end{aligned} \tag{2.15}$$

where h_x and h_z are the couplings of the transverse and longitudinal field, respectively. In this dissertation we do not study the case with a chiral coupling on the longitudinal field, so if not otherwise specified h_z is real and positive.

2.2.3 Phase diagram

In addition to the two commensurate phases which we have already discussed in the symmetric case, chiral clock models are known to host a new *floating incommensurate* phase for any $p \geq 3$ [61] . Let us start by clarifying the "dictionary" we are going to use. A phase is said to be incommensurate if it has a periodicity which is irrational multiple of the periodicity of the underlying lattice. Indeed it is customary to describe these models with the language of condensed matter physics, as this new kind of phases has been investigated in the context of incommensurate crystals [62] since the last seventies of the previous century. Thus, the picture one should keep in mind is that of a mono-layer of atoms getting adsorbed on a surface with a regular array of adsorption sites. In this sense the superlattice may either be commensurate or incommensurate with the underlying lattice. Then, by varying the temperature (or any other thermodynamic field in general) the ordered solid-like commensurate phase may melt either into a disordered fluid-like phase or into a floating solid-like incommensurate phase via a C-IC transition [36]. We also mention that in the literature these phases are sometimes referred to as Tomonaga-Luttinger liquids, because the C-IC transition may be mapped into the insulator-Luttinger liquid transition occurring in a one-dimensional spinless fermion

Incommensurate (IC)	$\langle \mathbf{S}(0)\mathbf{S}(\mathbf{r})\rangle \sim \cos(\mathbf{k}\cdot\mathbf{r}+\varphi_0)$
Floating incommensurate	$\langle \mathbf{S}(0)\mathbf{S}(\mathbf{r})\rangle \sim r^{-\eta}\cos(\mathbf{k}\cdot\mathbf{r}+\varphi_0)$
Fluid	$\langle \mathbf{S}(0)\mathbf{S}(\mathbf{r})\rangle \sim \exp(-r/\xi)\cos(\mathbf{k}\cdot\mathbf{r})$
Commensurate (C)	$\langle \mathbf{S}(0)\mathbf{S}(\mathbf{r})\rangle \sim \cos(\mathbf{k}_0\cdot\mathbf{r})$

Table 2.1: Dictionary of commensurate-incommensurate transitions from condensed matter physics in two dimensions [4] . $\mathbf{S}$ is the two-component order parameter or spin, $\mathbf{k}$ is the wave vector of the phase, η is a critical exponent, $\mathbf{k}_0$ is a constant vector and φ_0 a phase.

at the bottom of a quadratic band [73, 82]. More formally, we may characterise different kinds of phases according to the long-distance behaviour of the correlators, as it is summarised in Tab.2.1.

Let us now focus more quantitatively on the floating incommensurate phase we have to deal with when studying quantum chiral clock models. This phase is gapless, and therefore critical, with central charge $c = 1$. Correlation functions display a power-law decay with a complex modulation, formally

$$\langle ZZ^\dagger\rangle \sim A(r)\cdot\exp\left(\frac{2\pi i}{p}k\cdot r\right) \tag{2.16}$$

with $A(r)$ decaying algebraically and k being irrational, thus both the real and imaginary parts of the correlators display an oscillating pattern with algebraic damping. Before focusing on the phase transitions the incommensurate phase is bounded by in chiral clock models, we notice that in general the chiral perturbation may either be relevant or irrelevant, in the sense of the renormalisation group, so we would need to distinguish between these two cases. However, at least for p-state chiral clock models the chiral perturbation happens to be always relevant at the symmetric critical point θ and ϕ. Therefore, the C-IC transition must be in a different universality class from that of the corresponding symmetric model, implying that the symmetric critical point is multicritical [36].

Coming now to the topology of the phase diagram, the first C-IC phase transition, the one from the ordered phase to the floating one, belongs to the Pokrovsky-Talapov universality class, whereas the second one, from the floating phase to the disordered one, is Berezinskii-Kosterlitz-Thouless. In chiral clock models with order $p \geq 4$ the incommensurate phase opens as soon as we turn on the chirality, implying that the transition from the ordered to the disordered phase is always two-step. When $p = 3$ the situation is more controversial: either the incommensurate phase opens

immediately, as in the previous case, or there is a tricritical Lifshitz point so that at small angles the transition is one-step. In the latter case, the direct transition between the 3-Potts point and the Lifshitz point should be non-conformal and live in a new universality class, called *chiral*, which was firstly proposed by David A. Huse and Michael E. Fisher in 1982 [36]. More precisely, they have found that this phase transition should be unambiguously signalled by an abrupt change in the value of the incommensurability exponent $\overline{\beta}$ across the the Lifshitz point. Moreover, the product of the incommensurate wave vector and the correlation function is supposed to converge to a universal constant, meaning that the equality $\nu = \overline{\beta}$ between their critical exponents must hold, with the dynamical critical exponent being $z \neq 1$. For scaling considerations of why this has to be the case see again Ref. [36].

On the other hand, the literature about chiral clock models with also a longitudinal field is not so rich. Therefore we defer the discussion about how the topology of the phase diagram is supposed to change to the fourth and last chapter, where we propose a purely numerical study of the model.

2.3 Symmetries

This last section is devoted to the symmetries of clock models. First of all, both symmetric and chiral clock models enjoy a $\mathbb{Z}_p$ discrete global symmetry. On the contrary, when a longitudinal field is applied to the models, this symmetry gets explicitely broken. Indeed, it is easy to check that the unitary operator

$$\mathcal{O} = \prod_{j=1}^{L} X_j \tag{2.17}$$

acts as $\mathcal{O}^\dagger Z_j \mathcal{O} = \omega Z_j$ and $\mathcal{O}^\dagger X_j \mathcal{O} = X_j$, thus it commutes with the Hamiltonians(2.3) and (2.11), but not with (2.8) and (2.15). Moreover, in the basis where X is diagonal, the operator $\mathcal{O}$ may be recast as

$$\mathcal{O} = \prod \exp \begin{pmatrix} 0 & 0 & \dots & 0 \\ 0 & \frac{2\pi i}{p} & \dots & 0 \\ \vdots & & \ddots & \vdots \\ 0 & \dots & & \frac{2\pi i}{p}(p-1) \end{pmatrix} = \exp \left\{ \sum \frac{2\pi i}{p} \begin{pmatrix} 0 & 0 & \dots & 0 \\ 0 & 1 & \dots & 0 \\ \vdots & & \ddots & \vdots \\ 0 & \dots & & p-1 \end{pmatrix} \right\} \tag{2.18}$$

from which we identify

$$K = \begin{pmatrix} 0 & 0 & \dots & 0 \\ 0 & 1 & \dots & 0 \\ \vdots & & \ddots & \vdots \\ 0 & \dots & & p-1 \end{pmatrix} \tag{2.19}$$

as the discrete "generator" of the $\mathbb{Z}_p$ symmetry.

In addition to that, it is useful to take into account the three discrete space-time symmetries of charge conjugation, spatial parity and time reversal. Charge conjugation acts on the clock operators via the unitary operator C as $CZ_jC = Z_j^\dagger$, $CX_jC = X_j^\dagger$ with $C^2 = 1$. Spatial parity is realised by the unitary operator P acting as $PZ_jP = Z_{-j}$, $PX_jP = X_{-j}$ and $P^2 = 1$. Finally, time reversal is anti-unitary and it is realised by the operator T acting on the clock operators as $TZ_jT = Z_j^\dagger$, $TX_jT = X_j$ with $T^2 = 1$. In addition to that, we stress that the time reversal transformation also performs a complex conjugation of the phases, namely $e^{i\theta} \leftrightarrow e^{-i\theta}$ and $e^{i\phi} \leftrightarrow e^{-i\phi}$. Symmetric clock models - with and without a longitudinal field - clearly enjoy all these three symmetries, as the non-chiral Hamiltonian is left invariant under the previous transformations. This is not the case of the chiral Hamiltonian, where the presence of complex couplings may break some or all these symmetries. More precisely,

$$H(\theta,\phi) \overset{\mathrm{C}}{\mapsto} H(-\theta,-\phi), \quad H(\theta,\phi) \overset{\mathrm{P}}{\mapsto} H(-\theta,\phi), \quad H(\theta,\phi) \overset{\mathrm{T}}{\mapsto} H(\theta,-\phi),$$

meaning that when both the chiral phases are present, i.e. $\theta \neq 0$ and $\phi \neq 0$, the chiral Hamiltonian breaks separately charge conjugation, parity and time reversal. Still, it is invariant under their combination, CPT.

When $\phi = 0$ and $\theta \neq 0$:

$$H(\theta,0) \overset{\mathrm{C,P}}{\longmapsto} H(-\theta,0), \quad H(\theta,0) \overset{\mathrm{T}}{\mapsto} H(\theta,0), \quad H(\theta,0) \overset{\mathrm{CP}}{\longmapsto} H(\theta,0),$$

the chiral Hamiltonian breaks parity and charge conjugation, but it is invariant under time reversal and CP-symmetry.

Finally, when $\theta = 0$ and $\phi \neq 0$:

$$H(0,\phi) \overset{\mathrm{C,T}}{\longmapsto} H(0,-\phi), \quad H(0,\phi) \overset{\mathrm{P}}{\mapsto} H(0,\phi), \quad H(0,\phi) \overset{\mathrm{CT}}{\longmapsto} H(0,\phi),$$

the chiral Hamiltonian is invariant under parity and CT-symmetry, while it breaks time reversal and charge conjugation.

Another way of breaking some discrete space-time symmetry is via a longitudinal field with complex coupling. So, fixing $n \neq 0$ for p odd and $n \neq 0,\ n \neq p/2$ for p even s.t. $\omega^n \neq \pm 1$, Hamiltonian (2.9) transforms as

$$H(\omega) \overset{\mathrm{C}}{\mapsto} H(\omega^*), \quad H(\omega) \overset{\mathrm{P,T}}{\longmapsto} H(\omega), \quad H(\omega) \overset{\mathrm{PT}}{\longmapsto} H(\omega^*),$$

thus breaking charge conjugation but preserving both parity and time reversal. The breaking of the PT-symmetry is required for consistency by the CPT-theorem. We stress that the fact that this Hamiltonian preserves parity is consistent with the non-chiral nature of the model and it is due to the fact that the angle entering the definition of ω is integer multiple of $2\pi/p$.

If instead we do not fix n, charge conjugation is preserved by the global theory, consistently with the dual lattice gauge theory which is C-symmetric. Let us consider for example the case $p = 3$. If $n = 0$ the clock Hamiltonian trivially preserves the charge conjugation symmetry. On the other hand when $n = 1, 2$

$$H(n = 1) \overset{\mathrm{C}}{\mapsto} H(n = 2) \quad \text{and} \quad H(n = 2) \overset{\mathrm{C}}{\mapsto} H(n = 1) \tag{2.20}$$

the two topological sectors get exchanged, thus the theory is globally invariant even under charge conjugation.

3

Duality transformations

Duality transformations are powerful analytical tools both in statistical mechanics and quantum field theory. They are commonly used to recast the same model into different forms in order to capture different features. Indeed, what seems obscure and cumbersome may become simple and clear just dressing up the model in a different way so changing our point of view. Thus, duality mappings result extremely helpful as they allow to tackle problems which otherwise would be too difficult to deal with.

In this chapter we present the traditional Kramers-Wannier and Jordan-Wigner dualities of the Ising model and their generalisation to $\mathbb{Z}_p$-clock models for arbitrary p. The former generalises straightforwardly to clock models, while the latter requires a bit more of attention and in this framework it goes under the name of Fradkin-Kadanoff duality. We also introduce the notion of topological order and discuss the possibility of having edge states costing no energy. We end by presenting a duality between some lattice gauge theories and clock models, which relies on a recently developed formalism known as bond-algebraic approach.

3.1 Kramers-Wannier duality

The Kramers-Wannier duality was firstly discovered in 1941 by Hendrik Kramers and Gregory Wannier for two-dimensional ferromagnets [45, 46]. It relates the high- and low-temperature or, in our context, the strong- and weak-field regimes thus

establishing a mapping between order and disorder. Consequently, it also allows to locate at $h_c = 1$ (cfr. Eq. (1.49) and (2.3)) the point of second order phase transition occurring in these models. We start by discussing the the quantum Ising model [32, 54, 65] and then we will generalise the mapping to p-state clock models as well. For simplicity, we shall also enforce periodic boundary conditions in the following, even if we stress that this same duality holds true even under open boundary conditions.

The Kramers-Wannier duality maps Ising spins on the principal chain into Ising spins on the dual chain. We denote the dual sites - corresponding to the links of the original chain - using half-odd numbers in the form $i + \frac{1}{2}$, with i labelling the principal sites. Then we define the dual Pauli operators μ_i^x, μ_i^z so that

$$\sigma_i^x = \mu_{i-\frac{1}{2}}^z \mu_{i+\frac{1}{2}}^z \quad \text{and} \quad \sigma_i^z \sigma_{i+1}^z = \mu_{i+\frac{1}{2}}^x \,, \tag{3.1}$$

where μ^x, μ^z clearly obey the same algebra as the standard Pauli operators. Both the models enjoy a global $\mathbb{Z}_2$ symmetry generated by

$$\mathcal{O} = \prod_i \sigma_i^x \quad \text{and} \quad \mathcal{O}_{dual} = \prod_i \mu_{i+\frac{1}{2}}^x \,, \tag{3.2}$$

respectively. Using the duality (3.1) two global constraints emerge, namely

$$\mathcal{O}_{dual} = \prod_i \sigma_i^z \sigma_{i+1}^z = \mathbb{1} \quad \text{and} \quad \mathcal{O} = \prod_i \mu_{i-\frac{1}{2}}^z \mu_{i+\frac{1}{2}}^z = \mathbb{1} \,, \tag{3.3}$$

meaning that only those states satisfying these relations have to be considered, i.e. in the spectrum only $\mathbb{Z}_2$-singlets are allowed. Afterwards, inserting the expressions (3.1) into the Ising Hamiltonian (1.49) and setting $J = 1$ we find

$$H(\lambda) = -\sum_i \mu_i^x - h \sum_i \mu_i^z \mu_i^z \tag{3.4}$$

$$= h \left(-\sum_i \mu_i^z \mu_{i+1}^z - \frac{1}{h} \sum_i \mu_i^x \right) \,, \tag{3.5}$$

up to boundary terms which we neglect. Thus we see that (3.4) differs from the original Hamiltonian just by an overall factor h and by the replacement $h \leftrightarrow 1/h$ within the round bracket, therefore

$$H(\sigma; h) = h H(\mu; h^{-1}) \tag{3.6}$$

which is the same as saying that the strong- and weak-field regimes are equivalent. Indeed, thanks to (3.6) we are able to map an eigenvalue of $H(h)$ into a unique eigenvalue of $H(h^{-1})$. Moreover, (3.6) for the Hamiltonians implies for the energy gaps:

$$\Delta E(h) = h \Delta E(h^{-1}) \,. \tag{3.7}$$

So we see that if the gap vanishes for some $h = h_c$, then it must vanish also for $h^{-1} = h_c^{-1}$ and assuming that there is only one critical point, we are able to locate it as

$$h_c = \frac{1}{h_c} \qquad \Longleftrightarrow \qquad h_c = 1 \,, \tag{3.8}$$

which is by the way consistent with the expression of the energy gap known from the exact solution of the Ising model, namely $\Delta E(h) = 2|1-h|$. Before concluding the discussion about the Kramers-Wannier we also stress that as in our notation σ_i^z and σ_i^x are order and disorder operators respectively, and they may be used to define the corresponding order and disorder parameters, similarly the dual operators

$$\mu^z_{i+\frac{1}{2}} = \prod_{j=1}^{i} \sigma_j^x \qquad \text{and} \qquad \mu^x_{i+\frac{1}{2}} = \sigma_i^z \sigma_{i+1}^z \quad \text{with} \quad \mu^x_{L+\frac{1}{2}} = \sigma_L^x \tag{3.9}$$

are disorder and order operators, whose expectation values over the ground state define the corresponding disorder and order parameters. More precisely, the former operator is responsible for a spin flip of all those spins placed before site i, thus producing a *kink* excitation, and the kink proliferation clearly disorders the system. In fact, the ground state of the paramagnetic phase may be considered as a kink condensate. Instead the latter is sensitive to alignment of two nearest-neighbour spins only. In this sense, the Kramers-Wannier duality may also be regarded as a duality between order and disorder.

The generalisation to p-state clock models is straightforward. We define the dual clock operators such that

$$X_i = \Phi_{i-\frac{1}{2}} \Phi^\dagger_{i+\frac{1}{2}} \quad \text{and} \quad Z_i Z^\dagger_{i+1} = \Pi_{i+\frac{1}{2}} \,, \tag{3.10}$$

and they clearly obey the same algebra of the clock operators previously defined in (2.4). Both the original and the dual model enjoy a global $\mathbb{Z}_p$ symmetry which is generated by

$$\mathcal{O} = \prod_i X_i \quad \text{and} \quad \mathcal{O}_{dual} = \prod_i \Pi_{i+\frac{1}{2}} \,, \tag{3.11}$$

respectively, which give rise to the following constraints:

$$\mathcal{O}_{dual} = \prod_i Z_i Z^\dagger_{i+1} = \mathbb{1} \quad \text{and} \quad \mathcal{O} = \prod_i \Phi_{i-\frac{1}{2}} \Phi^\dagger_{i+\frac{1}{2}} = \mathbb{1} \,. \tag{3.12}$$

Writing then the Hamiltonian in terms of the dual operators we find

$$H(X, Z; h) = hH(\Pi, \Phi; h^{-1}) \tag{3.13}$$

which implies $h_c = 1$, just like for the Ising model. Strictly speaking, this property of both Ising and clock models is known as *self-duality*. We also recall that this result actually holds true for $p = 3, 4$-state clock models only, as for $p \geq 5$ the topology of the phase diagram changes and a new gapless phase opens [60].

Even chiral clock models enjoy an exact duality which is very similar to the Kramers-Wannier one. Indeed, we can proceed in a similar way by introducing the same dual operators of (3.10) to re-phrase the Hamiltonian (2.11), up to boundary terms, as

$$H = -J \sum_{i=1}^{L-1} \left(\Pi_{i+\frac{1}{2}} e^{i\theta} + \Pi_{i+\frac{1}{2}} e^{-i\theta} \right) - h \sum_{i=1}^{L} \left(\Phi_{i-\frac{1}{2}} \Phi^{\dagger}_{i+\frac{1}{2}} e^{i\phi} + \Phi^{\dagger}_{i-\frac{1}{2}} \Phi_{i+\frac{1}{2}} e^{-i\phi} \right) , \tag{3.14}$$

which is formally equivalent to the original Hamiltonian up to the simultaneous exchanges of the phases and of the couplings, formally

$$\theta \leftrightarrow \phi \qquad \text{and} \qquad J \leftrightarrow h \, .$$

A nice consequence of this is that the phase diagram of the model is symmetric with respect to the self-dual line $J = h$ when $\theta = \phi$ and for this reason the following numerical analysis we will often stick to this special case.

3.2 Jordan-Wigner duality

The Jordan-Wigner duality is another interesting mapping involving the Ising model. It was firstly proposed by Pascual Jordan and Eugene Wigner in 1928 to exactly diagonalise the Ising Hamiltonian, thus solving the model.

Let us discuss it in detail. The Jordan-Wigner duality maps spin operators into fermionic creation and annihilation operators, so allowing for a free-fermion formulation of the Ising model. To simplify the notation we enforce periodic boundary conditions, label the sites with $i = -\frac{L}{2}, -\frac{L}{2}+1, \ldots, -1, 0, +1, \ldots, \frac{L}{2}-1, +\frac{L}{2}$ (so our chain is now $L+1$ sites long) and work with the Hamiltonian

$$H = -\sum_{i} \left(\sigma^z_i + h \sigma^x_i \sigma^x_{i+1} \right) \tag{3.15}$$

which is unitarily equivalent to (1.49), up to the choice of the boundary conditions. Then we introduce the operators

$$\sigma^+_i \equiv \frac{1}{2} \left(\sigma^z_i + i \sigma^y_i \right) \quad \text{and} \quad \sigma^-_i \equiv \frac{1}{2} \left(\sigma^z_i - i \sigma^y_i \right) \tag{3.16}$$

which we use to define the following fermionic creation and annihilation operators

$$c_i \equiv \left[\prod_{j=-L/2}^{i-1} \exp\left(i\pi\sigma_j^+\sigma_j^-\right)\right]\sigma_i^- \quad \text{and} \quad c_i^\dagger \equiv \sigma_i^+\left[\prod_{j=-L/2}^{i-1} \exp\left(-i\pi\sigma_j^+\sigma_j^-\right)\right] \tag{3.17}$$

$$\text{s.t.} \quad \{c_i, c_j^\dagger\} = \delta_{ij}\,, \quad \{c_i, c_j\} = 0 = \{c_i^\dagger, c_j^\dagger\}\,. \tag{3.18}$$

By inverting the definition of the fermionic operators we find

$$\sigma_i^z = 2c_i^\dagger c_i - 1 \tag{3.19}$$

$$\sigma_i^x\sigma_{i+1}^x = \left(c_i^\dagger - c_i\right)\left(c_{i+1}^\dagger - c_{i+1}\right) \tag{3.20}$$

which may be plugged into the Hamiltonian (3.15) to recast it in the form

$$H = -2\sum_i c_i^\dagger c_i - h\sum_i \left(c_i^\dagger - c_i\right)\left(c_{i+1}^\dagger - c_{i+1}\right) \tag{3.21}$$

which is now quadratic in the fermionic operators and thus diagonalisable. Before doing it, it is better to provide some important remarks about what happens at the boundaries which were firstly argued by Alexei Kitaev [42].

First of all we notice that the Hamiltonian (3.21) contains terms in the form c_ic_{i+1} and $c_i^\dagger c_{i+1}^\dagger$, therefore the fermion number, generated by $F = \sum_i c_i^\dagger c_i$, is conserved only modulo 2. Instead, the fermion parity is preserved as a direct consequence of the $\mathbb{Z}_2$ symmetry of the Ising model. Therefore, we stress that the choice of periodic boundary conditions on the spins does not completely specify the boundary conditions for the fermions as it leaves their parity unfixed [25, 30]. The second observation we want to point out is the possibility of having fermionic edge zero modes [42] in this model. To see this it is more instructive to go back to the notation defined in Chapter 1 for the Ising model and re-phrase it now in terms of Majorana fermions. This dual representation in terms of Majorana fermions is more commonly referred to as *Kitaev chain* or *wire*. Then we recall that a fermionic edge state is an operator, say Ψ, which commutes with the Hamiltonian $[H, \Psi] = 0$, anti-commute with the fermion number operator $\{(-1)^F, \Psi\} = 0$ and has a finite normalisation $\Psi^\dagger\Psi = 1$ even in the thermodynamic limit. The Ising model does have two of these zero modes when open boundary conditions are enforced. So let us see this by firstly introducing the operators

$$\chi_j^1 \equiv \left(\prod_{k<j}\sigma_k^x\right)\sigma_j^z \quad \text{and} \quad \chi_j^2 \equiv i\left(\prod_{k<j}\sigma_k^x\right)\sigma_j^z\sigma_j^x \tag{3.22}$$

which are self-adjoint, they anti-commute with each other and square to the identity, thus they are good Majorana operators indeed. If we re-write the Ising Hamiltonian with open boundary conditions (1.49) (pay attention that here we are no longer considering (3.15)!) we find

$$H = ih \sum_{j=1}^{L} \chi_j^1 \chi_j^2 + iJ \sum_{j=1}^{L-1} \chi_j^2 \chi_{j+1}^1 \,. \tag{3.23}$$

It is now easy to see that, upon setting $h = 0$, operators χ_1^1 and χ_L^2 at the boundaries do no longer enter the Hamiltonian and therefore they commute with it. As they also anticommute with the fermion parity and are correctly normalised (as they square to the identity) the are rightful fermionic edge zero modes. What is interesting in this whole picture is that the ordinary notion of order in the spin system becomes *topological order* [80] in the fermion model, which is signalled by the twofold degeneracy of the ground state along with the absence of a local order parameter acquiring a non-zero vacuum expectation value in the ordered phase. Indeed, no spontaneous breaking of any symmetry occurs here. These observations have given a new popularity to these models as the twofold degenerate ground states may be used a *qubit* which is robust against decoherence thanks to the presence of the energy gap between the first excited state. Thus, it is promising for *fault-tolerant quantum computing* [41] .

Let us now go back to the previous discussion and diagonalise the Hamiltonian (3.21): we firstly consider the Fourier transform of the fermion operators

$$c_j = \frac{1}{\sqrt{L+1}} \sum_k e^{-ikj} c_k \quad \text{and} \quad c_j^\dagger = \frac{1}{\sqrt{L+1}} \sum_k e^{ikj} c_k^\dagger \,, \tag{3.24}$$

where c_k and $c_k^\dagger$ are the fermionic creation and annihilation operators in momentum space. Using then (3.24) into (3.21) we find

$$H = -2 \sum_{k>0} (1 + h \cos k)(c_k^\dagger c_k + c_{-k}^\dagger c_{-k}) + 2ih \sum_{k>0} \sin k (c_k^\dagger c_{-k}^\dagger + c_k c_{-k}) \,, \tag{3.25}$$

where

$$\frac{1}{L+1} \sum_j e^{-i(k-k')j} = \delta_{k,k'} \tag{3.26}$$

has been used. Now we have to re-write the Hamiltonian in a canonical form via *Bogoliubov transformation*. So we introduce the new operators

$$\begin{cases} \eta_k = u_k c_k + i v_k c_{-k}^\dagger \\ \eta_k^\dagger = u_k c_k^\dagger - i v_k c_{-k} \end{cases} \quad \text{and} \quad \begin{cases} \eta_{-k} = u_k c_{-k} - i v_k c_k^\dagger \\ \eta_{-k}^\dagger = u_k c_{-k}^\dagger + i v_k c_k \end{cases} \tag{3.27}$$

where u_k and v_k are positive real coefficients. By imposing these operators to be fermionic, i.e. $\{\eta_k, \eta_p^\dagger\} = \delta_{kp}$, $\{\eta_k, \eta_p\} = 0 = \{\eta_k^\dagger, \eta_p^\dagger\}$, we find the equation

$$u_k^2 + v_k^2 = 1 \tag{3.28}$$

which is solved by

$$u_k = \cos\theta_k \quad \text{and} \quad v_k = \sin\theta_k \tag{3.29}$$

for $\theta_k \in [0, 2\pi[$. At this point we simply have to invert the relations in (3.27) to find out an explicit expression for the c-type operators

$$\begin{cases} c_k = u_k\eta_k - iv_k\eta_{-k}^\dagger \\ c_k^\dagger = u_k\eta_k^\dagger + iv_k\eta_{-k} \end{cases} \quad \text{and} \quad \begin{cases} c_{-k} = u_k\eta_{-k} + iv_k\eta_k^\dagger \\ c_{-k}^\dagger = u_k\eta_{-k}^\dagger - iv_k\eta_k \end{cases} \tag{3.30}$$

and insert these expressions into (3.25), so that the Hamiltonian becomes

$$\begin{aligned} H = &\sum_{k>0} \left[-2(1 + h\cos k)(u_k^2 - v_k^2) + 4h\sin k u_k v_k\right] (\eta_k^\dagger\eta_k + \eta_{-k}^\dagger\eta_{-k}) + \\ &+ \sum_{k>0} \left[4i(1 + h\cos k)u_k v_k + 2ih\sin k(u_k^2 - v_k^2)\right] (\eta_k^\dagger\eta_{-k}^\dagger + \eta_k\eta_{-k}) \,. \end{aligned} \tag{3.31}$$

Now we need to impose the vanishing of the second term, i.e.

$$4(1 + h\cos k)u_k v_k + 2h\sin k(u_k^2 - v_k^2) = 0 \,. \tag{3.32}$$

By using (3.28), from which we have

$$2u_k v_k = \sin 2\theta_k \quad \text{and} \quad u_k^2 - v_k^2 = \cos 2\theta_k \,, \tag{3.33}$$

(3.32) becomes

$$4(1 + 1 + h\cos k)\sin 2\theta_k + 2h\sin k\cos 2\theta_k = 0 \,. \tag{3.34}$$

This provides an explicit expression for the angles θ_k, formally

$$\tan 2\theta_k = -\frac{h\sin k}{1 + h\cos k} \tag{3.35}$$

which is equivalent to

$$\sin 2\theta_k = \frac{h\sin k}{\sqrt{1 + 2h\cos k + h^2}} \,, \tag{3.36}$$

$$\cos 2\theta_k = -\frac{1 + h\cos k}{\sqrt{1 + 2h\cos k + h^2}} \,. \tag{3.37}$$

Now we have done, as the Hamiltonian now reads

$$H = 2\sum_k E_k \eta_k^\dagger \eta_k + const. \tag{3.38}$$

with E_k providing the dispersion relation

$$E_k = \sqrt{1 + 2h\cos k + h^2} \tag{3.39}$$

which has a minimum for $k = \pm\pi$, so we recover the known expression for the energy gap $E_{\pm\pi} = 2|1-h|$.

3.3 Fradkin-Kadanoff duality

Clock models are the natural candidates to generalise the previous discussion beyond the $\mathbb{Z}_2$ symmetry of the Ising model. Indeed, their dual formulation in terms of *parafermions* via Fradkin-Kadanoff transformation is known to host a topological phase as well. However, zero-mode edge states generalising the Majorana ones do exist only when parity and time-reversal symmetries are broken, i.e. when clock models are chiral [25]. Given that one usually performs these duality transformations with the goal of identifying the edge states, in this section we focus on the chiral case only.

The Fradkin-Kadanoff duality, named after Eduardo Fradkin and Leo P. Kadanoff (1980) [31] , is indeed the natural generalisation of the Jordan-Wigner duality to p-state clock models with arbitrary clock order p. Let us discuss it in detail [25, 54]. We firstly take into account the chiral Hamiltonian defined in (2.11) and define at each site j of the chain the parafermions operators

$$\chi_j \equiv \left(\prod_{k=1}^{j-1} X_k\right) Z_j \tag{3.40}$$

$$\psi_j \equiv \omega^{\frac{p-1}{2}} \chi_j X_j = \omega^{\frac{p-1}{2}} \left(\prod_{k=1}^{j-1} X_k\right) Z_j X_j \tag{3.41}$$

where as usual $\omega = 2\pi/p$ being p the clock order. Moreover, the parafermion operators clearly obey the same algebra as the spin operators, namely

$$(\chi_j)^p = (\psi_j)^p = \mathbb{1}\,, \quad \chi_j^\dagger = \chi_j^{-1} = \chi_j^{p-1}\,, \quad \psi_j^\dagger = \psi_j^{-1} = \psi_j^{p-1}$$
$$\chi_j \psi_j = \omega \psi_j \chi_j\,.$$

In addition to that, now the parafermion operators do not commute even at different sites, because of the non-locality of their definition. Thus, we have

$$\chi_j\chi_k = \omega\chi_k\chi_j \quad \psi_j\psi_k = \omega\psi_k\psi_j\,, \quad \chi_j\psi_k = \omega\psi_k\chi_j \quad \text{for} \quad j < k\,. \tag{3.42}$$

So we see that parafermions are the natural p-state generalisation of the Majorana fermions of the Ising chain, with the difference that for clock models $\omega \neq \omega^{-1}$. Now performing the substitutions

$$X_j = \omega^{\frac{p-1}{2}}\chi_j^\dagger\psi_j \quad \text{and} \quad Z_j^\dagger Z_{j+1} = \omega^{\frac{p-1}{2}}\psi_j^\dagger\chi_{j+1} \tag{3.43}$$

into the Hamiltonian (2.11) we find that the parafermion Hamiltonian reads

$$H = -J\omega^{\frac{p-1}{2}}\sum_{j=1}^{L-1}\psi_j^\dagger\chi_{j+1}e^{-i\theta} - h\omega^{\frac{p-1}{2}}\sum_{j=1}^{L}\psi_j^\dagger\chi_j e^{-i\phi} + h.c.\,, \tag{3.44}$$

which is not as easily solvable as the Ising Hamiltonian in terms of free fermions. In fact, due to the relations in (3.42), there is a non trivial coupling between parafermion operators at different momenta, so even performing a Fourier transform we are not able to recast it into a block diagonal Hamiltonian as we did for the Ising model. As we have already mentioned in the previous chapter, clock models are not exactly solvable indeed. Yet, chiral clock models are integrable for a two-parameter family of couplings along the line

$$h\cos(p\phi) = J\cos(p\theta)\,. \tag{3.45}$$

We shall not discuss the integrability of the model along this special line as this would go beyond the goal of this dissertation. Similarly, we will not go through the formal derivation of the existence of edge states. We just mention that zero-mode edge states are indeed present even in these $\mathbb{Z}_p$-clock models when chiral couplings are present so to break both parity and time reversal symmetries. Moreover, when this last requirement is satisfied, they are exact, thus signalling the presence of topological order. Thus, chiral clock models may allow for interesting applications to topological quantum computing [53].

3.4 Clock models and Lattice Gauge Theories

Lattice Gauge Theories (LGTs) are non-perturbative regularisations of gauge theories on a discretised spacetime. They were firstly proposed by Kenneth G. Wilson [84] in order to tackle the problem of quark confinement within the framework of

quantum cromodynamics. However, their range of application was immediately understood to be much wider and nowadays they represent one of the most lively research areas in modern physics. In this section we shall not review the entire formal machinery of lattice gauge theories as the literature is extremely rich. We will instead provide only those tools which are strictly necessary for framing the duality between lattice gauge theories and clock models.

3.4.1 Lattice gauge theories in a nutshell

For our purposes we are interested only in a specific class of LGTs, namely Abelian $\mathbb{Z}_N$ lattice gauge theories on a ladder geometry in the Hamiltonian formulation [43]. The ladder geometry is a quasi two-dimensional geometry consisting in a lattice $\mathbb{L}$ made of two parallel chains (legs) coupled to each other by rungs in order to form square plaquettes [64]. We shall index rungs with $i = 1, \dots, L$, being L the length of the ladder and links with ℓ. Links on upper and lower legs will be denoted with $\ell^{\uparrow}, \ell^{\downarrow}$ respectively, whereas those on vertical rungs with ℓ^0. As gauge group degrees of freedom live on the links, we may introduce two unitary operators U_ℓ and V_ℓ for each link $\ell \in \mathbb{L}$ which commute on different links, whereas on the same link they satisfy

$$V_\ell U_\ell = \omega U_\ell V_\ell \quad \text{and} \quad U_\ell^N = V_\ell^N = \mathbb{1}_N \tag{3.46}$$

being $\omega = \exp\left(\frac{2\pi i}{N}\right)$ [74]. Let us now list what we need for constructing a lattice gauge theory:

(i) attach to each link ℓ a N-dimensional Hilbert space $\mathcal{H}_\ell$ which is spanned by the othonormal basis $\{|v_{k,\ell}\rangle_{k=1,\dots,N-1}\}$ (*electric basis*) such that $V_\ell|v_{k,\ell}\rangle = \omega^k|v_{k,\ell}\rangle$ and $U_\ell|v_{k,\ell}\rangle = |v_{k+1,\ell}\rangle$ (taking $k+1$ mod N);

(ii) identify the V's operators ($V_\ell^{\uparrow}$, $V_\ell^{\downarrow}$ and V_ℓ^0) as the *electric field operators*;

(iii) define on each plaquette the *magnetic field operators* as $U_i = U_i^{\downarrow} U_{i+1}^0 (U_i^{\uparrow})^\dagger (U_i^0)^\dagger$;

(iv) select as physical states only those states which satisfy the Gauss' law, formally $G_i^a|\Psi_{phys}\rangle = |\Psi_{phys}\rangle$, $\forall\ i$ with $a = \uparrow, \downarrow$, where $G_i^{\uparrow} = V_i^{\uparrow}(V_{i-1}^{\uparrow})^\dagger (V_i^0)^\dagger$ and $G_i^{\downarrow} = V_i^{\downarrow} V_i^0 (V_{i-1}^{\downarrow})^\dagger$ are *Gauss operators*.

A pictorial representation of these operators is provided in Fig.3.1. The gauge invariant Hamiltonian on the ladder then reads [64]

$$H_{\mathbb{Z}_N} = -\sum_i \left[U_i + \lambda \left(V_i^{\uparrow} + V_i^{\downarrow} + V_i^0 \right) + h.c. \right] \tag{3.47}$$

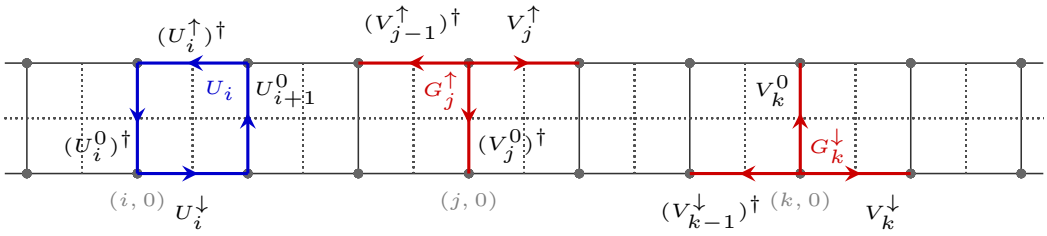

Figure 3.1: Pictorial representation of the local operators of the $\mathbb{Z}_N$ LGT on the ladder. In particular the plaquette/magnetic (blue) and the two Gauss' (red) operators are drawn.

with coupling constant $\lambda > 0$ and enforcing PBCs on the legs. We notice that there is a strong formal analogy between this theory and the famous two-dimensional Toric Code [41, 66]. In both cases the total Hilbert space of physical states can be decomposed as

$$\mathcal{H}_{phys} = \bigoplus_{n=0}^{N-1} \mathcal{H}_{phys}^{(n)} \tag{3.48}$$

with $\mathcal{H}_{phys}^{(n)}$ superselection sectors which may be distinguished by the operators

$$\overline{S} = V_{i^*}^{\uparrow} V_{i^*}^{\downarrow} \quad \text{and} \quad \overline{W} = \prod_{i \in \mathcal{C}^*} U_i^{\downarrow} \,, \tag{3.49}$$

with i^* labelling an arbitrary rung of the ladder and $\mathcal{C}^*$ being a non-contractile loop around the ladder, such that $\overline{W}\overline{S} = \omega \overline{S}\overline{W}$. Moreover, we recall that physical states in $\mathcal{H}_{phys}^{(n)}$ are eigenstates of $\overline{S}$ with eigenvalues ω^n, whereas the action of operator $\overline{W}$ results in a mapping of $\mathcal{H}_{phys}^{(n)}$ into $\mathcal{H}_{phys}^{(n+1)}$ [64].

Finally, let us make a few comments about the topology of the phase diagram of these Abelian $\mathbb{Z}_N$ LGTs, which are known to display topological order. It is indeed known from the literature that models with Hamiltonian (3.47) exhibit confined/deconfined phases separated by a *deconfined-confined phase transition* (DCPT). In standard lattice gauge theories the most important diagnostic tool for distinguishing between these two kinds of phases is the behaviour of Wilson loops, i.e. the product of all magnetic operators in a given region. Indeed they are known to display an area law behaviour within confined phases and a perimeter law behaviour within deconfined ones [84]. However, the ladder geometry has a disadvantage: both the area and the perimeter of a loop linearly grow with the size of the ladder, namely L. However, one can still look at the behaviour of $\mathcal{W}_D \equiv \prod_{i \in D} U_i$ over some connected region D to capture the phase transition [64]. Indeed we find that for $\lambda = 0$ - in full

analogy with the Toric Code [41] - the ground state of the system may be regarded as a condensate of electric loops and it is therefore deconfined with $\langle \mathcal{W}_D \rangle \approx 1$. On the other hand, in the limit $\lambda \to \infty$ electric loops get suppressed signalling a confided phase with $\langle \mathcal{W}_D \rangle \approx 0$.

3.4.2 Bond-algebraic approach to dualities

Let us now review the recently developed bond-algebraic approach to dualities. Details along with paradigmatic examples can be found in Ref. [60].

The notion of *bond algebra* was firstly introduced in 2008 by Zohar Nussinov and Gerardo Ortiz and relies on the crucial observation that most Hamiltonians can be written as the sum of quasi-local terms $\{h_R\}$ (*bonds*) as [56]

$$H = \sum_R \alpha_R h_R \,, \tag{3.50}$$

with α_R c-numbers and R finite set of indices (e.g. lattice sites). By definition a bond algebra $\mathcal{A}\{h_R\}$ is then the linear space of operators generated by all products of the bonds and their Hermitian conjugates. In this regard, we stress two points: bond operators h_R do not need to be all independent and the same Hamiltonian admits in principle more bond algebras depending on how it is partitioned into quasi-local terms.

Within this framework dualities are revealed to be bond algebras homomorphisms, i.e. structure-preserving local mappings between bond algebras which may be implemented as unitary or projective-unitary transformations [60]. So let us consider two Hamiltonians H_1 and H_2 acting on spaces having the same dimensions. H_1 and H_2 are then said to be *dual* if there exists a homomorphism between some bond algebra $\mathcal{A}_{H_1}$ of H_1 and some bond algebra $\mathcal{A}_{H_2}$ of H_2, formally

$$\begin{aligned} \Phi : \; \mathcal{A}_{H_1} &\longrightarrow \mathcal{A}_{H_2} \\ H_1 &\mapsto \Phi(H_1) = H_2 \,. \end{aligned} \tag{3.51}$$

Moreover, any bond algebra $\mathcal{A}$ is unitary implementable, i.e. there exists a unitary matrix $\mathcal{U}$ such that

$$\Phi(\mathcal{O}) = \mathcal{U}\mathcal{O}\mathcal{U}^\dagger, \quad \forall \mathcal{O} \in \mathcal{A} \,. \tag{3.52}$$

The bond-algebraic approach to dualities also comes along with the notion of *gauge-reducing dualities*. The process of eliminating gauge constraints may indeed be realised as a bond-algebraic duality [60] which allows to map a gauge model into a

non-gauge one. We recall that gauge models are characterised by the presence of redundant degrees of freedom so that the total space of states is actually larger than the space of physical states obeying the Gauss' law. Moreover, physical observables are required to be gauge invariant, thus they are realised as Hermitian operators which have to commute with the gauge symmetry. A gauge-reducing duality is then a mapping defined over a bond algebra which maps all local gauge operators to the identity, trivially. Formally

$$\Phi_{GR}(H_G) = H_{GR} \quad \text{and} \quad \Phi_{GR}(G_R) = \mathbb{1} \quad \forall R \tag{3.53}$$

where H_G and H_{GR} are the gauge and gauge-reduced Hamiltonians respectively, and G_R is the group of gauge symmetries.

3.4.3 Ladder LGT-clock models duality

Thanks to the bond-algebraic approach to dualities we are now able to establish a gauge-reducing duality mapping between the $\mathbb{Z}_N$ gauge model on the ladder and N-state clock models with both transverse and longitudinal field. Let us discuss the main steps (a more detailed discussion can be found in Ref. [64]).

We firstly associate with each plaquette of the LGT theory a site of the chain of the dual clock model. This allows us to map the gauge-invariant magnetic operator U_i into the single-body clock operator X_i. Afterwards, we map the V_i^0 operator into the "kinetic" term $Z_i Z_{i-1}^\dagger$ entering the clock Hamiltonian 2.8. This last mapping is justified by the fact that the electric field on the rung link ℓ_i^0 equals the flux difference between the two adjacent plaquettes. Turning then to the $V_i^\uparrow$, $V_i^\downarrow$ operators, we may define the mapping to clock operators via the following transformation

$$V_i^\uparrow \mapsto a_i^\downarrow Z_i^\dagger \quad \text{and} \quad V_i^\downarrow \mapsto a_i^\uparrow Z_i \tag{3.54}$$

with $a_i^\uparrow$, $a_i^\downarrow$ complex coefficients which must preserve the algebra defined in (3.46), guarantee the automatic enforcing of the Gauss' law, i.e. $G_i^\uparrow \mapsto \mathbb{1}$ and $G_i^\downarrow \mapsto \mathbb{1}$, and ensure that within each superselection sector $\overline{S} \mapsto \omega^n \mathbb{1}$. These three requirements allow to uniquely fix the values of the previous constants as $a_i^\downarrow = 1$ and $a_i^\uparrow = \omega^n$. Summarising, our sector dependent duality mapping reads [64]

$$\begin{aligned} U_i &\mapsto X_i\,, & V_i^0 &\mapsto Z_i Z_{i-1}^\dagger, \\ V_i^\uparrow &\mapsto Z_i^\dagger\,, & V_i^\downarrow &\mapsto \omega^n Z_i\,. \end{aligned} \tag{3.55}$$

A visual representation is sketched in Fig.3.2. Thus, applying this duality transformation to the LGT Hamiltonian (3.47) we find

$$H_{\mathbb{Z}_N}(\lambda) = \lambda H_{clock}(\lambda^{-1}) \tag{3.56}$$

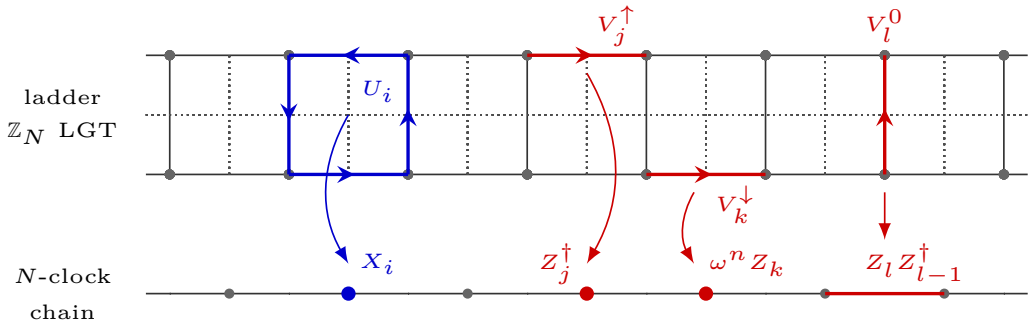

Figure 3.2: Pictorial representation of the local operators of the $\mathbb{Z}_N$ LGT on the ladder along with the duality transformation to the N-state clock model.

where

$$H_{clock}(\lambda^{-1}) = -\sum_i \left[Z_i Z_{i-1}^\dagger + \lambda^{-1} X_i + (1+\omega^n) Z_i + h.c. \right] \tag{3.57}$$

is a familiar clock Hamiltonian with both transverse and longitudinal field (cfr. (2.8) upon setting $J = 1, h = \lambda^{-1}$ and performing a change of variables in the summation, $i \to i-1$). We stress that the longitudinal field in the clock Hamiltonian keeps memory of the superselection sector of the dual lattice gauge theory as it depends explicitly on ω^n. Moreover, for $n = 0$ and also for $n = N/2$ if N is even, the coupling constant of the longitudinal field becomes real or disappears. However, we stress that even when the coupling is complex, the clock Hamiltonian is not chiral as ω^n is integer multiple of $2\pi i/N$, therefore the interaction energy between two spins is invariant under their interchange. Such a behaviour can be made explicit by redefining the Z clock operators as $Z_i \mapsto \omega^{-n/2} Z_i$ so that their eigenvalues get globally rotated but the algebra (2.4) is preserved. More precisely, for n even the eigenvalues simply get permuted without affecting the energy spectrum of the model. Instead, for n odd up to a re-order the eigenvalues get all shifted by a factor of $\pi/N = \omega/2$. In this way the Hamiltonian (3.57) can be rephrased as [64]

$$H_{clock}(\lambda^{-1}) = -\sum_i \left[Z_i Z_{i-1}^\dagger + \lambda^{-1} X_i + h.c. \right] - 2\cos\left(\frac{\pi n}{N}\right) \sum_i \left(Z_i + Z_i^\dagger \right) . \tag{3.58}$$

We stress that the presence of a longitudinal field depending on the n in the clock Hamiltonian, for n odd results in a two-fold degenerate ground state.

The main advantage of this duality transformation between Abelian $\mathbb{Z}_N$ lattice gauge theories and clock models - as we will better appreciate in the next chapter - relies in the correspondence between their phase diagrams, so that we may study either model to gain information about the other one. Thus it can be seen that the

confined and deconfined phases of the lattice gauge theory become respectively the paramagnetic and ferromagnetic phases of the dual clock model formulation. Moreover, the presence of the longitudinal field breaks the N-fold symmetry of the ferromagnetic phase into a one-fold (if n even) or two-fold (if n odd) degeneracy, depending on the parity of the superselection sector [64].

4

Numerical analysis

In this chapter we carry out an in-depth analysis of clock models with the aim of probing the theoretical predictions we have presented in the previous chapters. To this purpose, we have performed extensive DMRG numerical simulations with tensor networks [29] in order to explore the phase diagram of both symmetric and chiral clock models. The main focus is understanding the nature of the different phases along with the phase transitions they are bounded by. The most important observables encoding this information are the energy gap, the order (or disorder) parameter, the entanglement entropy and the correlation functions. Our discussion takes place in three steps: we firstly address to themes which are well-established in the literature in order to test our numerical apparatus and bring further evidence supporting the results. Then, we move on by trying to tackle those issues which are more controversial, like the topology of the phase diagram of 3-state chiral clock models and the oscillations of the energy gap. Afterwards, by adding a longitudinal field to the clock Hamilonian, we venture into new scenarios in order to study how the phase diagram gets modified. At the very end of the chapter we propose a purely numerical study of the duality linking clock models and lattice gauge theories working in the clock model formulation and making some contact with the recent literature.

4.1 DMRG parameters

We start with a short review of the best algorithm parameters we have chosen for the numerical simulations. For further information see appendix A.

For 3- and 4-state clock models, both symmetric and chiral, five DMRG sweeps with a schedule of increasing maximum bond dimension up to 150 were found to be enough to reach a high accuracy away from criticality. Instead, at criticality and when dealing with higher order clock models, we have gradually increased the maximum bond dimension up to 200 and 250 together with the number of sweeps. The truncation error cutoff has been fixed at 10^{-12}, which is near to exact accuracy. The noise term has been gradually reduced sweep by sweep down to a minimum of zero: this should ensure the convergence of DMRG calculations, especially of those conserving quantum numbers. Finally, increasing the number of iteration of the Davidson algorithm up to ~ 10 was found to be very efficient in order to get more accurate results at criticality.

4.2 Symmetry implementation

As already mentioned in the second chapter, both symmetric and chiral clock models enjoy a discrete global $\mathbb{Z}_p$ symmetry. Therefore, out of the ordered phase where this symmetry gets spontaneously broken, the eigenvalues $Q = 0, 1, 2, \ldots, p-1$ of the operator (2.19) behave as quantum numbers which are conserved under the dynamical evolution of the system. Thus, we have implemented (at least when possible) the conservation of these quantum numbers throughout DMRG calculations using *ITensor*. This allows for two main advantages:

(i) Speed up our numerical simulations and use less memory as the DMRG algorithm runs more quickly;

(ii) Obtain the ground states in the different symmetry sectors.

The clock Hamiltonian is automatically quantum number preserving, therefore we simply had to prepare the initial states within the right symmetry sector. Also, we have used chain lengths which were multiple of the clock order: this should allow for more precise results by minimising the competing effects between the finite size of the system and the symmetry constraints.

If not otherwise specified, all the following results within the disordered phase and at criticality (both points of second order phase transitions and incommensurate critical phases) have been obtained with conserved quantum numbers.

4.3 $p = 3$, 4-state clock models with transverse field

Coming to the results, we now start by presenting the numerical analysis carried out on transverse clock models with order $p \leq 4$. These are the simplest models we are going to discuss, as we recall that their phase diagram hosts just a single critical point located at $h_c = 1$[2]. In this sense, we say that 3- and 4-state clock models generalise straightforwardly the Ising model. Let us discuss the behaviour of the main physical observables in order to reconstruct a picture of the phase diagram.

4.3.1 Energy gap

In order to diagnose criticality in these models and investigate their different phases, we have firstly focused on the energy gap. Since in the disordered phase 3- and 4-state clock models enjoy an exact $\mathbb{Z}_3$ and $\mathbb{Z}_4$ symmetry respectively, we have separately computed the ground states in the different symmetry sectors, which are shown in Fig.4.1(a) and (b). This has allowed us to identify the state with $Q = 0$ as the true ground state of the system and that with $Q = 1$ as the first excited state, which were consequently used to compute the energy gap. Actually, this holds true for any order p as far as the model is non-chiral. We will come back to this later on.

We have then studied how the energy gap behaves as we tune the magnitude of the transverse field, h, across its critical value $h_c = 1$. We show the resulting plots in Fig.4.2(a) and (b) for 3- and 4-state clock models, respectively. In both cases the picture emerging from the profile of the energy gap is consistent with a self-dual phase diagram hosting two gapped phases separated by a critical point. Yet, the gap does not perfectly close at $h_c = 1$, but it rather appears as a minimum getting lower as the size of the system increases. This is a pure finite-size effect due to the fact that we have performed numerical simulations with finite chains. Indeed we recall that no phase transition can occur when we constrain a system to a finite geometry. Thus, in order to infer what happens in the thermodynamic limit, we have studied the scaling of the energy gap for increasing values of the chain length L and extrapolated its value as $L \to \infty$, assuming a purely linear dependence between ΔE and $1/L$ and performing a fit of the data. This last assumption is justified by the fact that for 3- and 4-state clock models the energy gap equals the inverse of the correlation length as the dynamical exponent is known to be $z = 1$ (cfr. (1.14)). The results of the analysis are shown in Fig.4.3 (a) and (b).

[2]From now on, unless otherwise specified, we will refer to the previously defined Hamiltonian (2.3) with open boundary conditions.

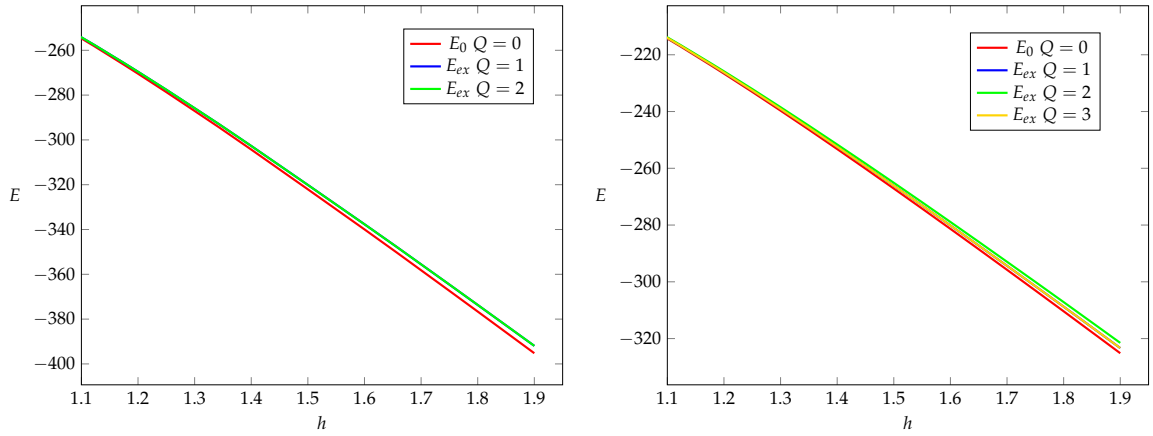

(a) 3-state clock model. **(b)** 4-state clock model.

Figure 4.1: Energy levels of the 3-state clock model (on the left) and 4-state clock model (on the right), with $L = 99$ and $L = 100$ respectively, within the different symmetry sectors of the disordered phase as a function of h. When $p = 3$ the energy levels in the sectors $Q = 1$ and $Q = 2$ are almost perfectly degenerate. The same holds true for the sectors $Q = 1$ and $Q = 3$ when $p = 4$. In both cases one should consider the energy level with $Q = 0$ as the true ground state of the system and the one with $Q = 1$ as the first exited state in order to compute the energy gap.

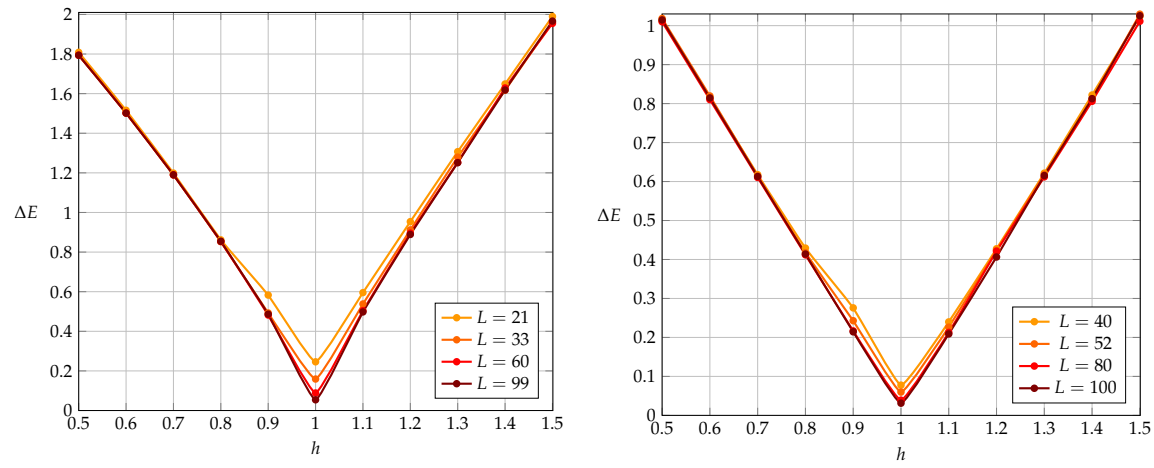

(a) 3-state clock model. **(b)** 4-state clock model.

Figure 4.2: Energy gap of the 3-state clock model (on the left) and 4-state clock model (on the right) for different lengths of the chain. Both the plots show that, although the minimum gets lower as the length of the chain increases, the gap does not perfectly close because of the finite size of the system. We also put a grid to guide the eye to appreciate the self-duality of the plot.

In both cases, as $L \to \infty$ the energy gap goes almost perfectly to zero at $h_c = 1.0$, supporting the hypothesis of a second order phase transition. Namely: $\Delta E = 0.000659 \pm 0.000013$ and $\Delta E = 0.00018 \pm 0.00003$ for the 3- and 4-state clock model, respectively[3]. The other two points, $h = 0.9$ and $h = 1.1$, in the ordered and disordered phase respectively, are chosen to be symmetric with respect to the critical point in order to check the self-duality of the model. For the 3-state clock model we have found $\Delta E(h = 0.9) = 0.47833 \pm 0.00004$ and $\Delta E(h = 1.1) = 0.47972 \pm 0.00014$, which are in very good agreement as they differ only by 0.3%.[4]

Instead, in the case of 4-state clock model a small discrepancy is found: $\Delta E(h = 0.9) = 0.1855 \pm 0.0006$ and $\Delta E(h = 1.1) = 0.1928 \pm 0.0004$, differing by 4%. The lower accuracy here is likely due to the fact that we are still considering chain lengths of $L \sim 10^2$ as in the case of 3-state clock models. However, now the clock order is higher, thus deviations from the first order linear behaviour become larger as well and they start playing some role. As a general rule, in order to reach the same accuracy one should consider larger values of L as the order, p, of the clock model increases.

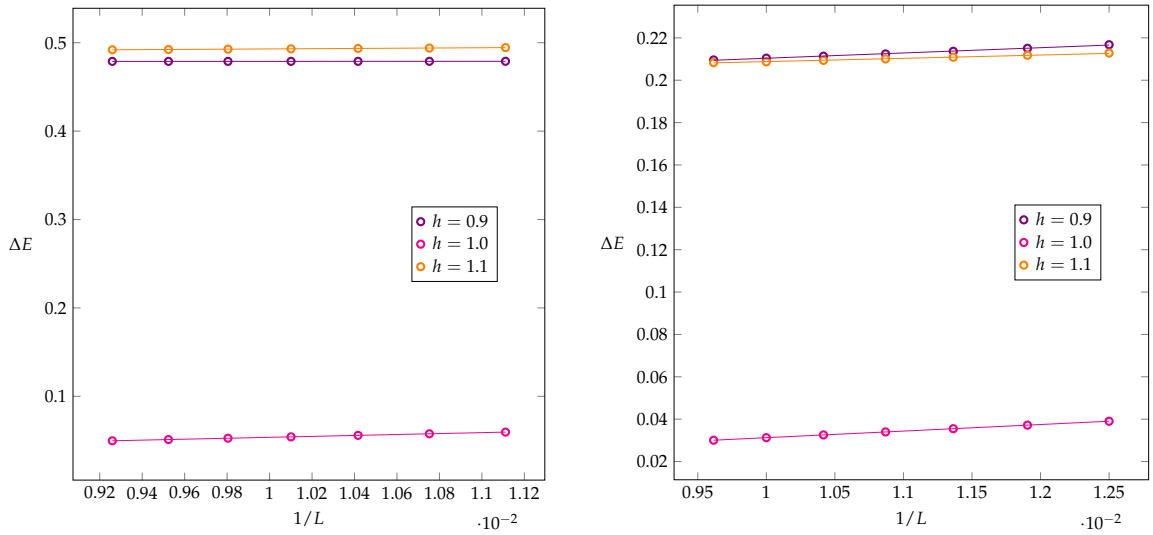

(a) 3-state clock model.

(b) 4-state clock model.

Figure 4.3: Scaling of the energy gap of the 3- (left) and 4- (right) state clock model at three different points: $h = 0.9$, $h_c = 1.0$ and $h = 1.1$. In both cases, in the limit of infinite chain the gap goes to zero at $h_c = 1.0$, whereas it converges approximately to the same non-zero values at $h = 0.9$ and $h = 1.1$, consistently with the self-duality property of these models.

[3] All the errors in this section have been estimated from the linear fits.

[4] To be more precise, in this dissertation we refer to dimensionless energies as they are energies in unit of J, the coupling of the kinetic term entering the clock Hamiltonian (2.3)

The last piece of information we can extract from the energy gap is the value of the critical exponent ν associated with the divergence of the correlation length at criticality. Although it is not enough, as at least two critical exponents are needed to identify unambiguously the universality class, this may start shedding some light on the nature of the phase transition. Thus, given $z = 1$, we expect the energy gap to scale like $\Delta E \sim |\epsilon|^{\nu}$ as we approach the critical point either from the disordered phase or from the ordered one, due to the self-duality of the models. In the present case, we have chosen to approach criticality from the disordered phase. The fits of the data reported in Fig.4.4(a) and (b) reveal $\nu = 0.838 \pm 0.008$ for $p = 3$ and $\nu = 0.999 \pm 0.009$ for $p = 4$. This strongly suggests that the second order phase transitions occurring in 3- and 4-state clock models may fall into the 3- and 4-Potts universality classes, which are characterised by $\nu = 5/6$ and $\nu = 1$, respectively. We will see that this is indeed the case by computing the critical exponents associated with other observables.

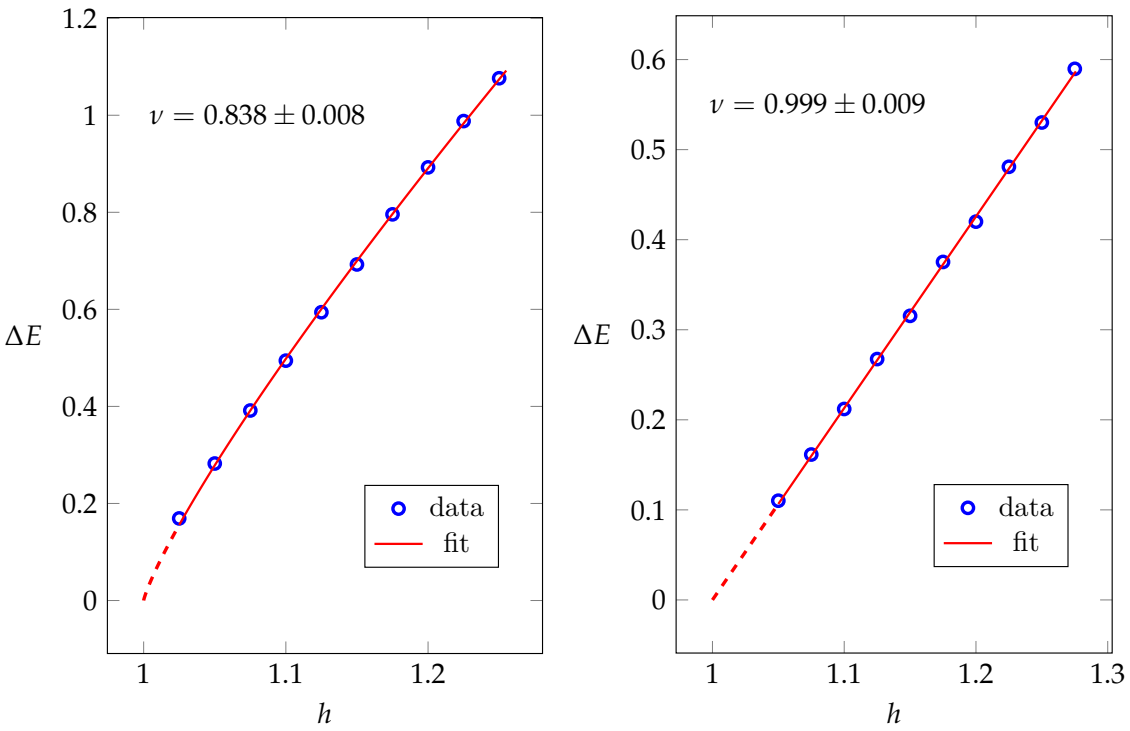

(a) 3-state clock model.

(b) 4-state clock model.

Figure 4.4: Critical exponent ν for 3- and 4-state clock models computed by fitting the data of the energy gap in a vicinity of the critical point $h_c = 1$. In both cases we have found values of ν suggesting that the phase transitions may fall into the 3- and 4-Potts universality classes.

4.3.2 Entanglement entropy

The second observable we take into account is the entanglement entropy. We have already discussed in the first chapter the crucial role played by this physical quantity in the theory of critical phenomena and how we can use it to gain information about the nature of phase transitions. In this regard, we recall that, for relativistic theories ($z = 1$) like those we are considering in this section, in the critical regime the entanglement entropy is known to diverge logarithmically. We show in Fig.4.5 the curves of the half chain entanglement entropy of the 3-state clock model for different values of the chain length ($L = 60, 90, 120, 150, 180, 210$). We immediately see from this plot that finite-size effects result both in the rounding and shifting of the singularities: as the size of the system increases the peaks get higher and sharper and they shift towards $h_c = 1$. More quantitatively, we may sit at $h_c = 1$, where the phase transition takes place in the the thermodynamic limit, and evaluate the finite-size scaling of the entanglement entropy by plotting it as a function of the logarithm of L, according to the Calabrese-Cardy law (1.48) (we recall that we are enforcing open boundary conditions). We expect a linear dependence, so we may extract the angular coefficient of the logarithmic growth which is proportional to the central charge of the underlying conformal field theory. The resulting plots for both 3- and 4-state clock models are shown in Fig.4.6(a) and (b). In the first case we have found $c = 0.7995 \pm 0.0014$, which is consistent with the nominal value $c = 4/5$ of the 3-Potts universality class. Instead, in the second case the central charge is found to be $c = 1.00860 \pm 0.00013$, which differs only by $\sim 0.86\%$ from the nominal value $c = 1$ of the 4-Potts universality class. This last small discrepancy is likely due to higher order corrections which get stronger as the clock order increases. Still, in both cases the analysis of the entanglement entropy may be considered consistent both with the theoretical predictions and with the numerical critical exponents.

Let us spend a few words about the non-critical regime as well. Away from criticality the system is gapped, meaning that the underlying quantum field theory is massive. Here the entanglement entropy does not scale logarithmically, but either increases monotonically with L up to a saturation value, or it is identically zero for any value of L, thus signalling that the state we are considering is unentangled, i.e. it is a product state [79]. In this case we see from the inset in Fig.4.5 that for the 3-state clock model the entropy is constant with L and different from zero as far as the transverse field is weak. On the other hand it is constant with L but vanishing when the magnitude of the transverse field $h \gtrsim 2$, implying that the magnetic field is so strong to set the spins into a unentangled product state.

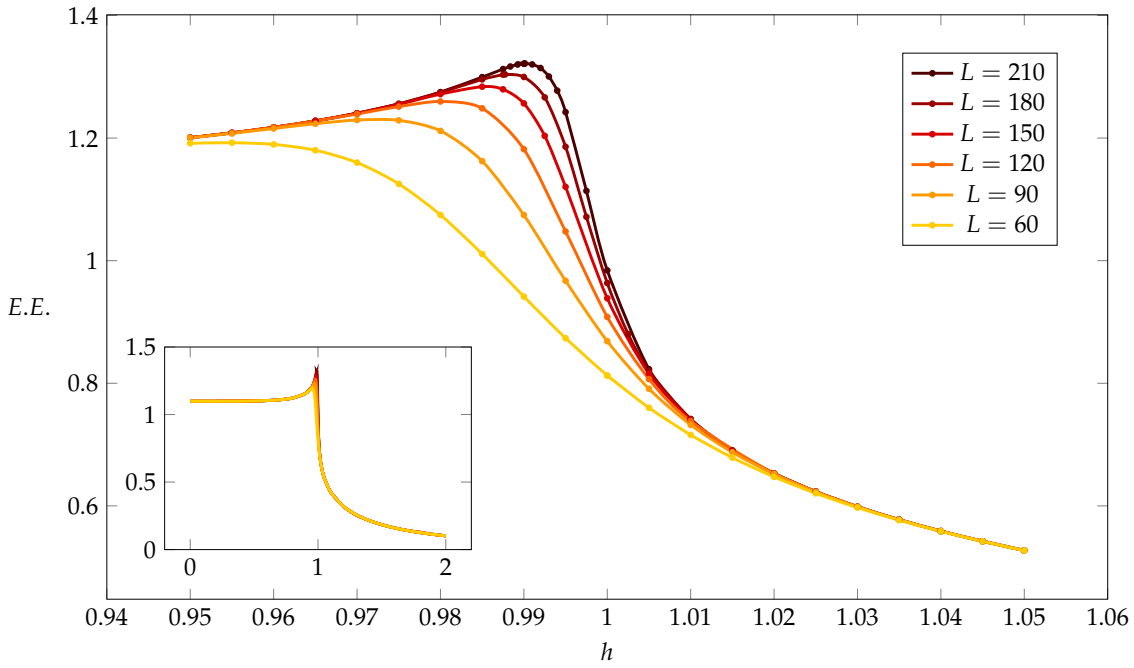

Figure 4.5: Half chain entanglement entropy of the 3-state clock model (OBC) at different chain lengths. Finite-size effects show themselves both in the rounding and shifting of the singularities: correctly the peaks of the entanglement entropy get sharper and shifted towards $h_c = 1$ as the chain length increases. Inset: same plot of the entanglement entropy for different chain lengths on a broader range of values of h.

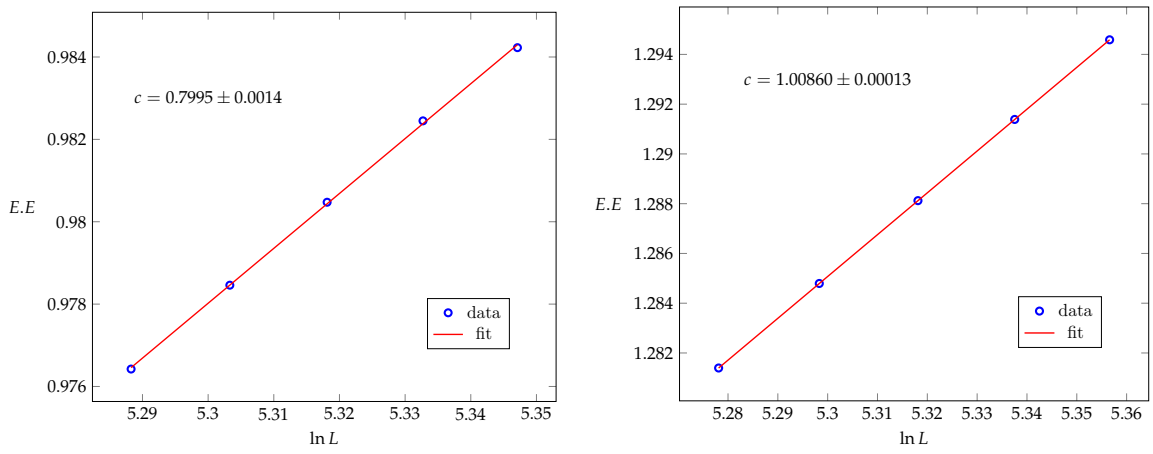

(a) 3-state clock model.

(b) 4-state clock model.

Figure 4.6: Finite-size scaling of the entanglement entropy for the 3- and 4-state clock model. A fit of the data according to the Calabrese-Cardy law (1.48) reveals values of the central charges compatible with the 3- and 4-Potts universality classes.

4.3.3 Magnetisation

In order to quantify the response of a spin system to the application of a transverse field, one usually introduces a quantity called magnetisation. For p-state clock models we define the normalised magnetisation as

$$M = \frac{1}{2L} \sum_i \langle X_i + X_i^\dagger \rangle \tag{4.1}$$

where X is the usual clock operator and and the expectation value $\langle \cdot \rangle$ is taken over the ground state. The magnetisation also provides a viable way for distinguishing between the two gapped phases of these models as in the thermodynamic limit it would be identically zero in the ordered phase and identically one in the disordered phase, displaying a point of inflection at criticality. Thus, the magnetisation is the natural disorder parameter for these models.

As usual, out of the thermodynamic limit we have to deal with finite-size effects, which for the magnetisation result in the smoothening of the singularity occurring at $h_c = 1$. We start by considering 3-state clock models and show in Fig.4.7(a) the curves of the magnetisation for different values of the chain length. First of all we stress that - unlike the previous cases - we have here enforced periodic boundary conditions in order to avoid boundary effects which would spoil the scaling analysis. Afterwards, we notice that the curves of the magnetisation are indeed smooth across $h = 1$, but they correctly get steeper as the chain length L increases. Moreover, out of the focus on a vicinity of $h_c = 1$, they goes to zero as we switch off the transverse field and they tend to one when the field is strong. The second crucial observation is that all the curves cross at a single point at $h \approx 1$, thus supporting the hypothesis of a second order phase transition occurring there in the thermodynamic limit. We may also be quantitative and evaluate the universal scaling of the magnetisation as we have already explained in the first chapter to verify the finite-size scaling law (1.44). In order to do so we firstly have to make an hypothesis on the nature of the phase transition. In this case we already known from the literature and from our previous numerical results that the expected universality class is 3-Potts, for which $\nu = 5/6$ and $\beta = 1/9$. Thus, by plotting the magnetisation multiplied by a factor of $L^{\beta/\nu}$ as a function of $L^{1/\nu}(h - h_c)$ we expect the curves to collapse all into the same universal constant, namely $Q(L^{1/\nu}(h - h_c))$, at least in a vicinity of the critical point. Such a behaviour is indeed verified as we see from Fig.4.8(a). This provides the second critical exponent which, along with the critical exponent ν of the correlation length and the central charge, validates the hypothesis of phase transition falling into the 3-Potts universality class for 3-state clock models.

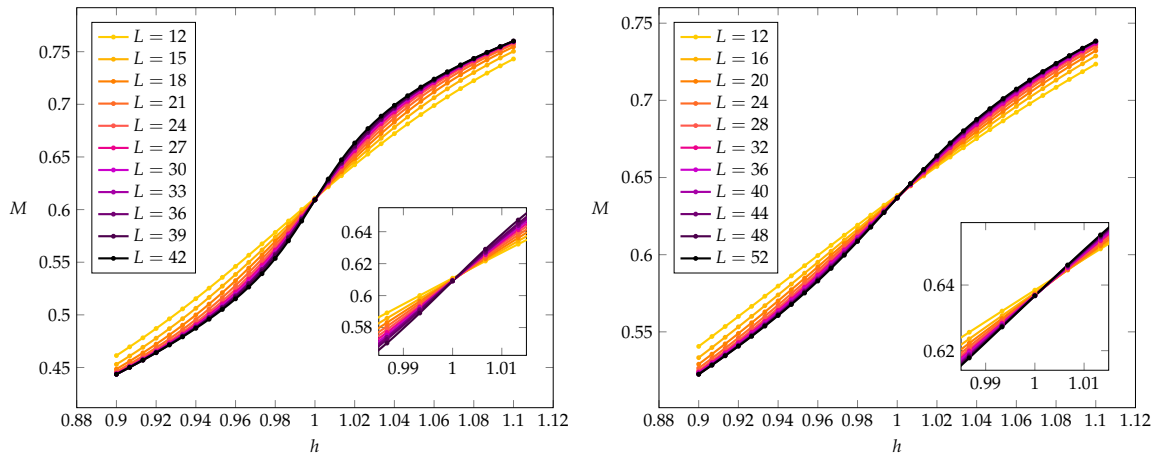

(a) 3-state clock model. **(b)** 4-state clock model.

Figure 4.7: Magnetisation of the 3- and 4-state clock model (PBC) at different chain lengths. In case of 3-state clock models the curves all cross at a single point which is consistent with the nominal value of the critical field $h_c = 1$. In the case of 4-state clock models we see that the curves cross at a point which is slightly shifted away from the nominal $h_c = 1.0$. This is a finite-size effect which gets stronger as the clock order increases. Indeed such a shifting is almost completely negligible in case of 3-state clock models. Insets: focus on a neighbourhood of the critical point.

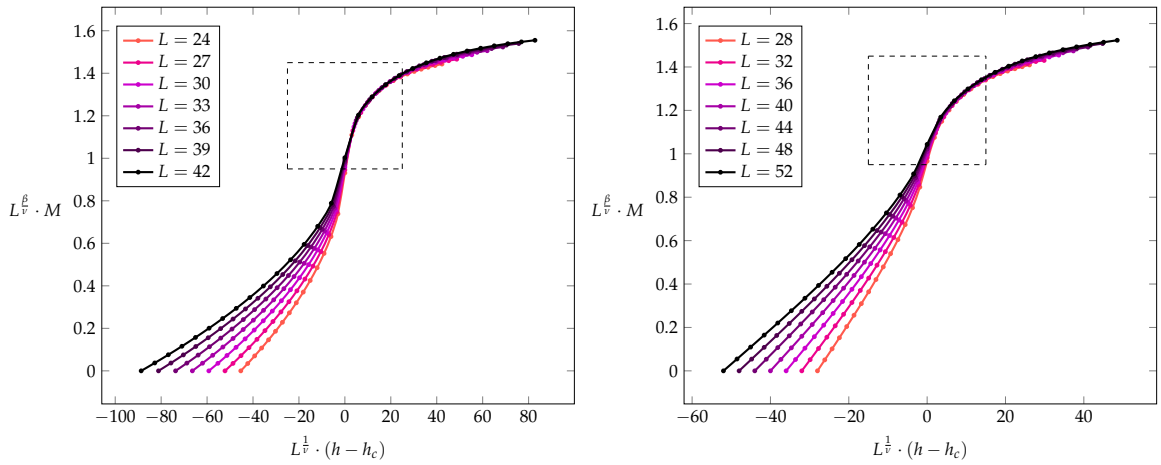

(a) 3-state clock model. **(b)** 4-state clock model.

Figure 4.8: Universal scaling of the magnetisation for the 3- and 4-state clock models (PBC). In both cases we see that, at least in a vicinity of the critical point, the curves of the magnetisation collapse onto the same universal curve. Such a behaviour allows us to extract the ratio β/ν between the critical exponents, verifying that the phase transitions occurring in the 3- and 4-state clock models fall into the 3- and 4-Potts universality class.

Going through very similar steps, one may also verify that the phase transition occurring in the 4-state clock model falls into the 4-Potts universality class. We show in Fig.4.7(b) the magnetisation of the 4-state clock model for different sizes. First of all we see that the curves are less steep with respect to those of the 3-state clock model. This may be easily explained in terms of the higher clock order. This is also the reason why in the present case the curves cross at a single point which is slightly shifted away from the nominal value of $h_c = 1.0$. Given the same values of L, finite-size effects are indeed usually stronger when the clock order is higher. As we have just done for the 3-state clock model, we may also evaluate the universal scaling of the magnetisation for the 4-state clock model as well. We have firstly made an hypothesis on the nature of the phase transition, which we expect to be 4-Potts. For this particular universality class $\nu = 1$ and $\beta = 1/12$ (cfr. Tab.1.1). We have plotted in Fig.4.8(b) the magnetisation multiplied by a factor of $L^{\beta/\nu}$ as a function of $L^{1/\nu}(h - h_c)$ in order to show that all the curves collapse into the same universal curve $Q(L^{1/\nu}(h - h_c))$ near criticality. This behaviour is indeed verified proving that for the 4-state clock model $\beta = 1/12$ and $\nu = 1$, thus it correctly falls into the 4-Potts universality class.

4.3.4 Binder cumulant

There is another way of checking that the critical point is indeed $h_c = 1$ in the thermodynamic limit, which relies on the *fourth-order Binder cumulant*, U_L. It is defined as the fourth-order cumulant of the order parameter, namely

$$U_L(h) = 1 - \frac{\langle \tilde{M}^4 \rangle}{3\langle \tilde{M}^2 \rangle^2} \tag{4.2}$$

where we have introduced the "longitudinal" magnetisation $\tilde{M} \equiv \frac{1}{2L}\sum_i (Z_i + Z_i^\dagger)$ as order parameter. The curves of the binder parameter for different system sizes provide useful information about the location of the critical point. Indeed, the critical field h_c corresponds to the point where all these curves cross in the thermodynamic limit [9]. Moreover, the finite-size scaling of the Binder parameter close to the critical point is known to be [9] $U_L(h) = b(\epsilon L^{1/\nu})$, where $b(x)$ is a universal constant. Thus, this provides an alternative way of working out the critical exponent ν in addition to the energy gap and the correlation length.

Let us now focus on the 3-state clock model enforcing periodic boundary conditions. We shown in Fig.4.9(a) the plot of the Binder parameter for different values of L. As expected, all the curves cross at a single point which is very close to

$h_c = 1.0$. To be more quantitative, we have studied the behaviour of the ratio U_{18}/U_{15} in the range $0.9 \leq h \leq 1.1$ and looked at its intersection point with the line $U_{18}/U_{15} = 1$. This has allowed us to identify $h_c = 0.995 \pm 0.005$ as the transition point, which is fully consistent with the nominal value of the literature. In Fig.4.9(b) we also show the finite-size scaling analysis of the Binder cumulant. By plotting U_L as a function of $(h - h_c)L^{1/\nu}$, using $h_c = 1.0$ and $\nu = 5/6$, we could check that all the curves collapse on the universal line $b(x)$, at least close to the critical point. This brings further evidence on the 3-state clock model to fall into the 3-Potts universality class. For the 4-state clock model very similar considerations hold true, therefore we do not present it.

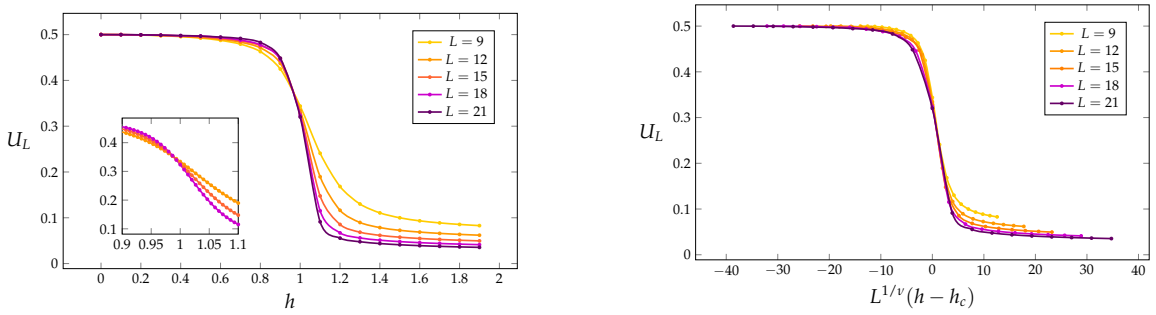

(a) U_L vs h **(b)** Finite-size scaling

Figure 4.9: Fourth-order Binder cumulant of the 3-state clock model (PBC) for $L = 9, 12, 15, 18, 21$. On the left we see that all the curves cross at a single point, consistently with the hypothesis of a phase transition occurring at $h_c = 1.0$ in the thermodynamic limit. Inset: zoom in on a neighbourhood of the critical point. On the right we show the finite-size scaling analysis, which suggests that for this model $\nu = 1$, consistently with the literature.

The universality classes of the 3- and 4-state clock models are now well established. Yet, for the sake of completeness let us also discuss correlation functions at criticality in order to extract the anomalous dimension η as well.

4.3.5 Correlation functions at criticality

We now conclude the discussion of 3- and 4-state clock models by studying the correlation functions at criticality, where the correlation length gets infinite and consequently the correlators decay algebraically. More precisely, we have already seen that their large distance behaviour at criticality defines the anomalous dimension η according to (1.17), thus providing further information about the universality class of the phase transition. In particular, as we are dealing with

one dimensional quantum system, for 3 and 4-state clock models at criticality we expect the correlation function to decay as $G(r) \sim 1/|r|^{\eta}$, in full analogy with the Ising model. Therefore we are able to easily extract the value of η by performing a fit of the correlation function, which we define here as $C_{ij} = \langle Z_i Z_j^{\dagger} \rangle$, at criticality with a power-law functional dependence. We have used chains of $L = 201$ and $L = 200$ for 3- and 4-state clock models respectively and, with the aim of avoiding boundary effects due to open boundary conditions, we have considered only sites from $1/4$ to $3/4$ of the chain length. More precisely, we have fixed the index $i = 50$ and varied j from 51 up to 150. Afterwards, we have performed a fit [10] of these data using the following functional dependence:

$$f(|i-j|) = p2 \cdot \frac{\exp(-|i-j| \cdot p1)}{|i-j|^{p0}} \tag{4.3}$$

where $p0$, $p1$ and $p2$ are three free parameters. The former, $p0$, provides the value of the critical exponent η, which we are interested in. Instead, $p1$ is the inverse of the correlation length, which has to be zero, as we are at the critical point, and $p2$ is a multiplicative constant which does not provide particularly useful information. The resulting plots are shown in Fig.4.10(a) and (b). The agreement with the theoretical fit is good, as a chi-squared test reveals $\chi^2 \sim 10^{-5}$. We also mention that before studying 3- and 4-state clock models we have checked the goodness of the chosen functional dependence using the Ising model as a testing ground, finding $\eta = 0.2486 \pm 0.0006$, which is in good agreement with the nominal value. Coming now to the results, in the case of 3-state clock model we have found $\eta_{fit} \approx 0.2813 \pm 0.0007$, which differs

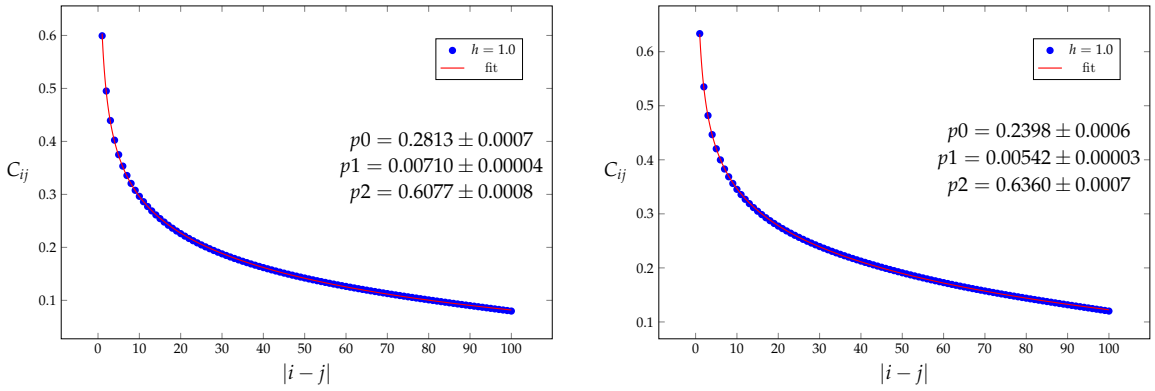

(a) 3-state clock model.

(b) 4-state clock model.

Figure 4.10: Fit of the correlation functions of 3 and 4-state clock models (OBC) at criticality. In both cases we have found values of the anomalous dimension η which are in reasonable agreement with the nominal values for the 3- and 4-Potts universality classes.

from the theoretical value $\eta_{theo} = 4/15$ approximately by 5%. On the other hand, for 4-state clock model we have found $\eta_{fit} \approx 0.2398 \pm 0.0006$, which differs from the theoretical value $\eta_{theo} = 1/4$ by 4%. In both cases the theoretical values of η refer to the thermodynamic limit, thus these small discrepancies are due to the finite size of the system and they may be reduced by increasing the value of L.

We do not discuss correlation functions out of criticality because there their behaviour is not universal. Indeed we recall that when the phase is gapped, correlators fall off exponentially and their decay is ruled by the correlation length with some velocity constant in front and these may both depend on the magnitude of the transverse field.

4.4 $p \geq 5$-state clock models with transverse field

We turn now our attention on clock models with order $p \geq 5$, where, as explained in the second chapter, a new gapless phase of Berezinskii-Kosterlitz-Thouless type is expected to open symmetrically around the point $h = 1.0$. Dealing with high-order clock models is computationally very demanding and for this reason we shall not go through the same analysis as before. Instead, we shall discuss few important observables focusing most of the time on 5-state clock models only.

4.4.1 Energy gap for $p = 5$ and $p = 6$

As usual, we have firstly studied how the energy gap behaves as a function of the magnitude of the transverse field h. We show in Fig.4.11(a) and 4.12b the resulting plots for 5- and 6-state clock models, respectively. First of all we see that the exact self-duality is lost, consistently with the literature. Then we see that, despite the usual finite-size effects preventing any phase transition in a finite geometry, there is evidence of a new critical phase which we know from the literature to be BKT. Indeed, the energy gap does no longer close at a single point, but it stands close to zero throughout a small region around $h = 1.0$ and then it starts growing again in the two regions where $h \ll 1$ and $h \gg 1$. Moreover, the size of this region is strictly dependent on the clock order: it gets broader as the order of the clock model increases, as we see from these same plots.

We are also able to approximately locate the boundaries of this critical region at $h \approx 0.85$ and $h \approx 1.15$ for 5-state clock models and at $h \approx 0.70$ and $h \approx 1.30$ for 6-state clock models. We recall that self-duality considerations require these

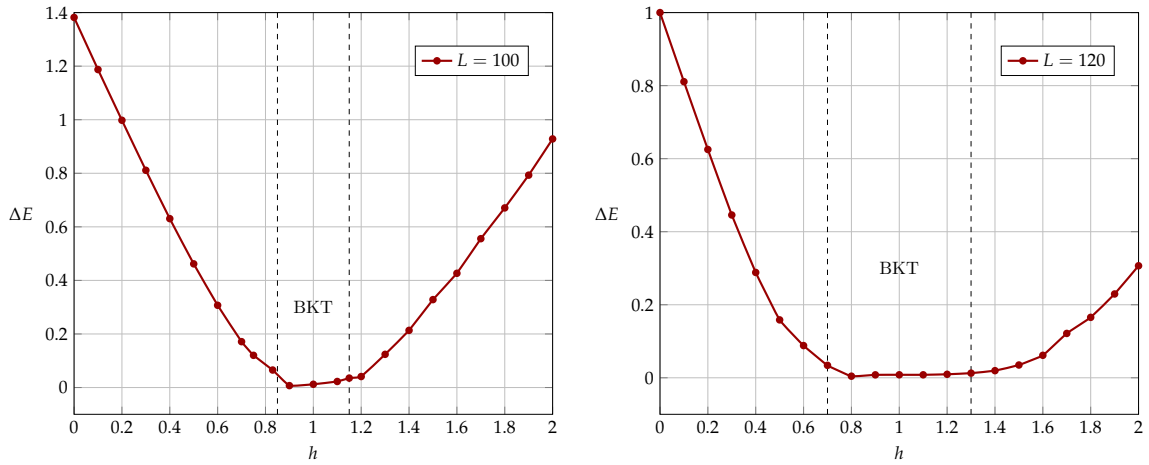

(a) 5-clock model. **(b)** 6-clock model.

Figure 4.11: Plots of the energy gap of 5- and 6-state clock model for a chain of length $L = 100$ and $L = 120$, respectively. In both cases the gap does no longer close at a single point, but a new gapless phase of Berezinski-Kosterlitz-Thouless type opens symmetrically around $h = 1.0$. We are able to approximately locate the two transition points at $h \approx 0.85$ and $h \approx 1.15$ for $p = 5$ and at $h \approx 0.70$ and $h \approx 1.30$ for $p = 6$. Moreover, as we see from the grid, the exact self-duality is lost as the plots are no longer symmetric with respect to the point $h = 1.0$.

two phase transitions to be of the same type, namely BKT, and to be symmetrically located around $h = 1.0$. Clearly the location of BKT critical points is a very difficult task, as we recall that for this special kind of phase transition the correlation length diverges much faster, as its divergence is exponential rather that algebraic. Finite-size scaling analysis for the energy gap may be helpful in this case, so let us discuss it for the 5-state clock model only, due to the huge computational effort. As we show in Fig.4.12, we have performed a fit of the data at different values of h. At $h = 0.85$ and $h = 1.15$ the gap becomes small, yet not perfectly equal to zero, signalling that we are in a vicinity of the phase transition, but still in the gapped ordered phase. At $h = 0.90,\ 1.00$ and 1.10 we have found values which are compatible with zero, meaning that we should now be inside the critical phase. We stress that the negative values we have found in the thermodynamic limit - which are apparently meaningless - signal that we are in presence of deviations from the first order linear behaviour of the energy gap as a function of $1/L$ and thus they are simply finite-size effects. This seems to suggest that in the thermodynamic limit the BKT can be found within a range $0.9 \lesssim h \lesssim 1.1$.

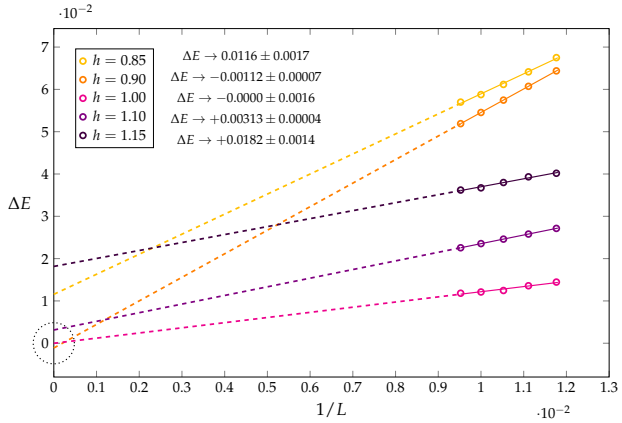

Figure 4.12: Scaling of the energy gap for the 5-state clock model. This analysis suggests that in the thermodynamic limit the BKT phase should be located between $h \approx 0.9$ and $h \approx 1.1$, which is a shorter ranged compared to the one we have previously identified in Fig.4.11(a). Thus, as the system size increases, the critical phase gets smaller.

4.4.2 Magnetisation

The second and last observable we discuss is the magnetisation. We shall focus on the $p = 5$ case only and we will not be quantitative with the finite-size scaling analysis as we are here interested only in the location of the phase transitions.

In full analogy with the 3- and 4-state clock models we have already discussed, we define the normalised magnetisation as in (4.1) enforcing periodic boundary conditions so to avoid boundary effects. High-order clock models would require long chains in order to reach a good accuracy, but at the same time the DMRG algorithm works worst and much slower when periodic boundary conditions are enforce. We have reached a compromise and considered chain lengths up to $L = 80$. The resulting plot is shown in Fig.4.13. If we zoom in on a neighbourhood of the critical BKT phase we see that the curves of the magnetisation all cross at the same value $h \approx 0.925$, they overlap all withing the range $0.925 \lesssim h \lesssim 1.075$ and then they separate again. Such a behaviour is somehow reminiscent of the one we have previously studied in Fig.4.7 for 3- and 4-state clock model. Before all the curves crossed at a single point, which we have identified as the true critical point of the thermodynamic limit, namely $h_c = 1.0$. Assuming then that the overlap of the curves is a signal of criticality, the plot of the magnetisation of the 5-state clock model seems to suggest that in the thermodynamic limit the actual BKT phase is located between $h \approx 0.925$ and $h \approx 1.075$. Such a range is shorter than the one we have identified in Fig.4.11(a) for $L = 100$, meaning that as the system size increases we expect the two critical point to shift towards each other, this resulting in the

shrinking of the critical phase as L increases.

If we make a comparison with the literature, this seems to go in the right direction. For example in Ref. [77] Sun *et al.* have investigated the location of the BKT phase opening in 5-state clock models by studying the scaling of the peaks of the fidelity susceptibility up to $L = 168$. This resulted in $h \approx 0.966$ for the first transition and $h = 1.035$ for the second one. By the way, they have carried out a similar analysis for the 6-state clock model as well for different sizes up to $L = 144$ finding $h \approx 0.782$ and $h \approx 1.285$ for the two BKT transitions, respectively.

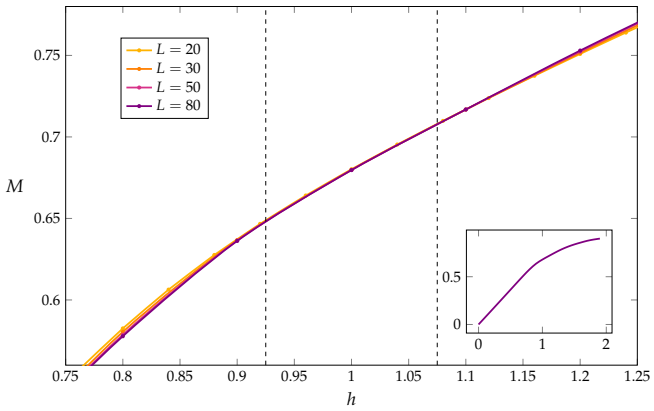

Figure 4.13: Magnetisation for the 5-state clock model (PBC) for different chain lengths. We show a focus on a neighbourhood of the BKT phase. The curves seem to cross at $h \approx 0.925$, then they overlap within the range $0.925 \lesssim h \lesssim 1.075$ and then they split again. Inset: profile of the magnetisation over a broader range of values of h.

4.5 $p = 3$-state chiral clock models with transverse field

This section is devoted to the study of transverse chiral clock models with order $p = 3$ only. This is indeed the first and simplest version of clock models hosting a floating incommensurate phase and thus it represents the best testing ground for investigating its nature. We firstly present the study of the energy gap as a function of h for different angles. This has allowed us to approximately locate the three different phases hosted by these models. In order to do so we have also exploited symmetries and dualities of the phase diagram. A specific discussion is deserved to the Lifshitz oscillations displayed by the energy gap when plotted as a function of the system size. We also briefly discuss the half-chain entanglement entropy in the self-dual case only. We conclude the section by presenting the analysis of the correlation functions within the incommensurate phase.

4.5.1 Energy gap

We proceed in analogy with the symmetric case by firstly discussing the energy gap in order to extract as much information as possible about the phase diagram. This is known to host three phases, out of which one is critical and the other two are gapped. More precisely the two gapped phases are the same ordered ferromagnetic and disordered paramagnetic phases which we have already encountered when studying symmetric clock models. The critical incommensurate one is instead completely new, as - we recall - it shows up starting from $p = 3$, so it has no counterpart in the chiral Ising model.

For convenience, we rewrite here the Hamiltonian of the 3-state chiral clock model for a chain of length L with open boundary conditions:

$$H = -J \sum_{j=1}^{L-1} \left(Z_j Z_{j+1}^{\dagger} e^{i\theta} + h.c. \right) - h \sum_{j=1}^{L} \left(X_j e^{i\phi} + h.c. \right) \ .$$

We have decided to use the same notation and conventions as Zhuang *et al.* [85]. We have fixed $J = 1 - h$, hence the phase diagram of the model depends only on h, θ and ϕ and then, given that the full phase diagram is three-dimensional and is also mostly unexplored for arbitrary angles, we have restricted ourselves only to some peculiar two-dimensional sections. Namely, we have focused on the following cases:

(i) Self-dual case with $\theta = \phi$;

(ii) Case with $\theta \neq 0$ and $\phi = 0$;

(iii) Case with $\theta = 0$ and $\phi \neq 0$.

Case (i). Along the line $\theta = \phi$ the phase diagram of the 3-state chiral clock model is self-dual, with the incommensurate phase opening symmetrically around the point $h = 0.5$, in between the ordered and disordered phases. In the limiting case $\theta = \phi = 0$ the model becomes non-chiral and one recovers all the results previously discussed for the symmetric 3-state clock model. Upon introducing the chirality in the model, two different scenarios are possible: either there is a Lifshitz point at $\theta = \phi = \frac{\pi}{6}$ (Fig.4.14(a)) [35] or a thin incommensurate layer survives all the way down to $\theta = \phi = 0$ (Fig.4.14(b)) [1, 51], implying that the incommensurate phase opens right away as the chirality is introduced. While chiral clock models with order $p \geq 4$ are known to fall into the second picture, for 3-state chiral clock the situation is more controversial as probing either scenario requires an extremely high level of accuracy which is usually impossible to reach in standard numerical simulations.

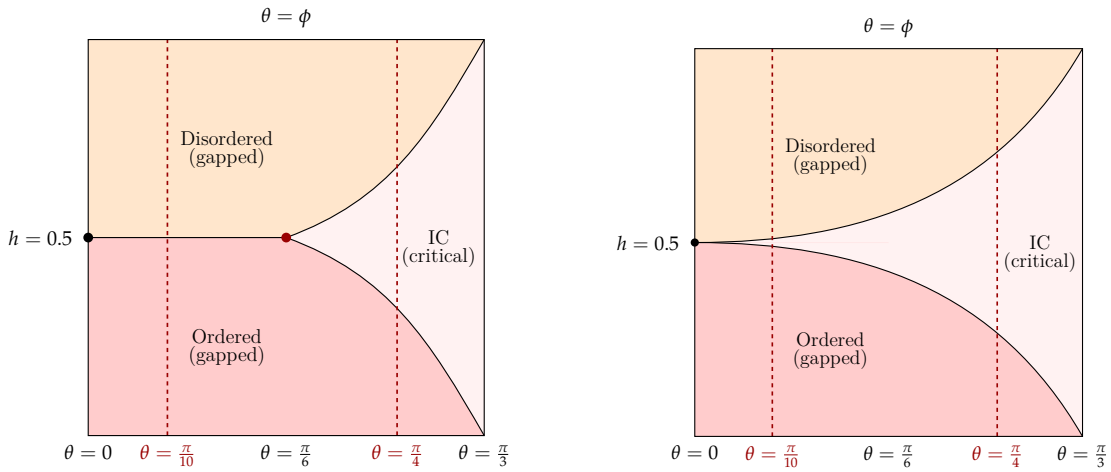

(a) One-step transition **(b)** Two-step transition

Figure 4.14: Cartoon of the two possible scenarios for the phase diagram of the 3-state chiral clock model with $J = 1 - h$ and $\theta = \phi$. On the left there is a tricritical Lifshitz point (in red), thus the phase transition for angles $\theta \leq \frac{\pi}{6}$ is one-step. On the right there is no tricritical point as the critical incommensurate phases persists all the way down to the non-chiral point. Obviously, in this last picture we have deliberately exaggerated the thickness of the incommensurate layer, which is actually very thin, if it ever exists.

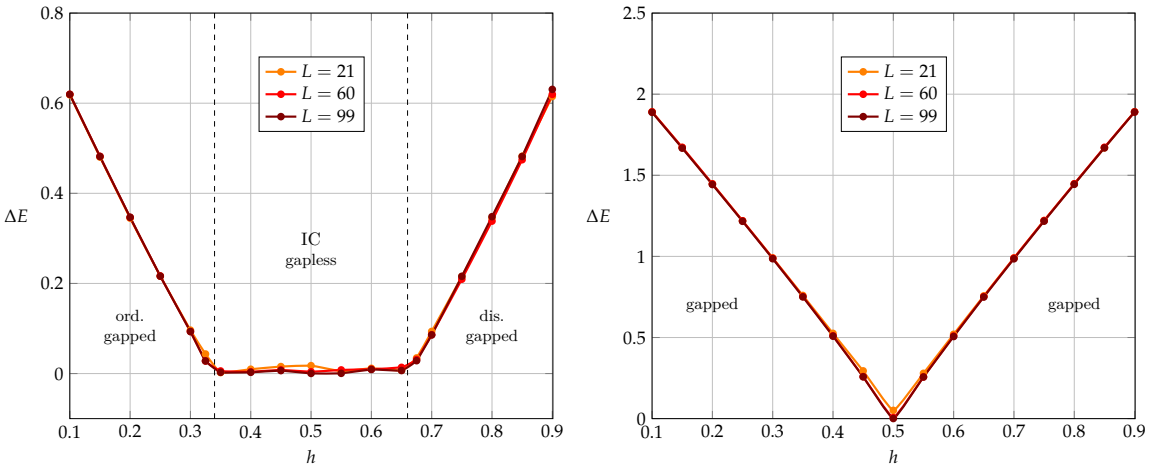

(a) $\theta = \phi = \frac{\pi}{4}$ **(b)** $\theta = \phi = \frac{\pi}{10}$

Figure 4.15: Plot of the energy gap of the 3-state chiral clock model at two different angles, $\theta = \phi = \frac{\pi}{4}$ (left) and $\frac{\pi}{10}$ (right) for different chain lengths. Both the plots are manifestly self-dual. On the left, we see the two gapped phases and the new critical phase opening symmetrically around the point $h = 0.5$. On the other side, we see a plot which shows resemblance with that of the 3-state non-chiral clock model, with the energy gap apparently closing at a single point.

We have then studied the dependence of the energy gap on the magnitude of the transverse field, h, for different angles. We show in Fig.4.15(a) and 4.15(b) the resulting plots for $\theta = \phi = \frac{\pi}{4}$ and $\theta = \phi = \frac{\pi}{10}$. In the former case the plot visibly displays two gapped phases and a critical one opening symmetrically around $h = 0.5$. We could approximately locate the boundaries of this critical region at $h \approx 0.34$ and $h \approx 0.66$. Due to the interplay between finite size of the chain, the clock order, symmetry constraints and chirality, performing the scaling of the energy gap to locale the phase transitions in the thermodynamic limit is not particularly fruitful, even considering chains length which are integer multiples of the clock order. We then recall that according to the literature the first C-IC transition falls into the Pokrovsky-Talapov universality class, whereas the second one is BKT in nature. The first statement may be easily checked by extracting the critical exponent ν associated with the divergence of the correlation length. From the literature we known that for Pokrovsky-Talapov $z = 2$ and $\nu = 1/2$, thus we expect the gap to close linearly as we approach the critical point from the left (cfr. (1.14)). This is indeed what we have found, which is shown in Fig.4.16. Also, according to the fit the gap closes starting from $h = 0.33713 \pm 0.00014$ for $L = 99$. The second phase transition is instead more difficult to locate and classify due to the exponential divergence of the correlation length. On the other hand, for $\theta = \phi = \frac{\pi}{10}$ the plot shows a strong

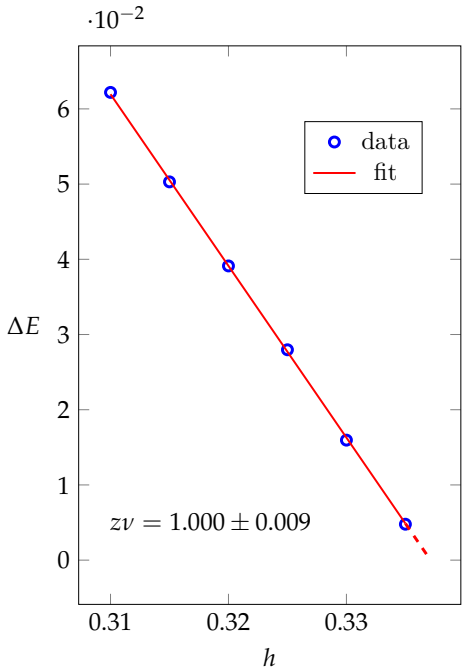

Figure 4.16: Fit of the energy gap near criticality for $\theta = \phi = \frac{\pi}{4}$. The linear closing of the energy gap is consistent with the Pokrovsky-Talapov theory predicting $z = 2$ and $\nu = 1/2$.

resemblance with the one of the 3-state non-chiral clock model (Fig.4.2(a)), yet this is not sufficient to conclude that the transition is one-step. In this regard we mention an interesting work recently carried out by S. Nyckees, J. Colbois and F. Mila on the classical 3-state chiral Potts model [57]. Using corner transfer matrix renormalisation group (CTMRG) and studying effective exponents they have found evidences which seem supporting the hypothesis of a chiral transition occurring at small angles. In particular they have found $\overline{\beta} \approx \nu \approx 2/3$ which is far away both from the nominal values of $\overline{\beta} = \nu = 1/2$ for Pokrovsky-Talapov and even from the $\overline{\beta} = 5/3$ and $\nu = 5/6$ for 3-Potts (cfr. Tab.1.1), suggesting that at small angles the transition may live into a different universality class.

Thus, we may be more quantitative and extract the critical exponent associated with the vanishing of the energy gap along the critical line $h = 0.5$. Before doing so, we recall that the dynamical exponent becomes different from one when the chirality is switched on. We have already said that for Pokrovsky-Talapov $z = 2$. In addition to that, we know from the literature that for the chiral transition $z = 3/2$ [57], thus the quantity $z\nu$ alone is not sensitive to this change. Yet, we may study whether its value is constant and unitary for different angles or not. We show then in Fig.4.17 the fit of the energy gap near criticality for different values of the angles, namely $\theta = \phi = \frac{\pi}{7}$, $\frac{\pi}{10}$, $\frac{\pi}{20}$, $\frac{\pi}{40}$ and $\frac{\pi}{80}$ with $L = 99$. We have performed the fit by approaching the critical point from either side, but expecting - as we have found indeed - values which are consistent with each other due to the self-duality of the phase diagram. First of all we notice that the value of $z\nu$ seems to change rather smoothly along the critical line $h = 0.5$. For $\theta = \phi = \frac{\pi}{20}$, $\theta = \phi = \frac{\pi}{40}$ and $\frac{\pi}{80}$ the critical exponent $z\nu$ is slightly larger that the nominal value $\nu = 5/6$ ($z = 1$) of the 3-Potts universality class for the non-chiral case. On the contrary, for $\theta = \phi = \frac{\pi}{7}$ we have found clear evidences of an incommensurate phase extending from $h = 0.4862 \pm 0.0003$ to $h = 0.5089 \pm 0.0014$. This is also supported by the fact that the gap closes linearly from the left, therefore this phase transition is Pokrovsky-Talapov and the Lifshitz point, if it exists, should be located before the theoretical value of $\frac{\pi}{6}$. Finally, for $\frac{\pi}{10}$ the critical exponents are smaller than one and assuming $z = 3/2$ we find $\nu_{\frac{\pi}{10}} = 0.635 \pm 0.004$ when approaching the critical point from the left and $\nu_{\frac{\pi}{10}} = 0.637 \pm 0.005$ when approaching it from the right. These values are not to far from $\nu \approx \overline{\beta} = 2/3$ found in Ref. [57], but they may also be approximately consistent with a Pokrovsky-Talapov transition if instead we assume $z = 2$. We will come back to this issue when discussing correlation functions along with the incommensurate wave vector.

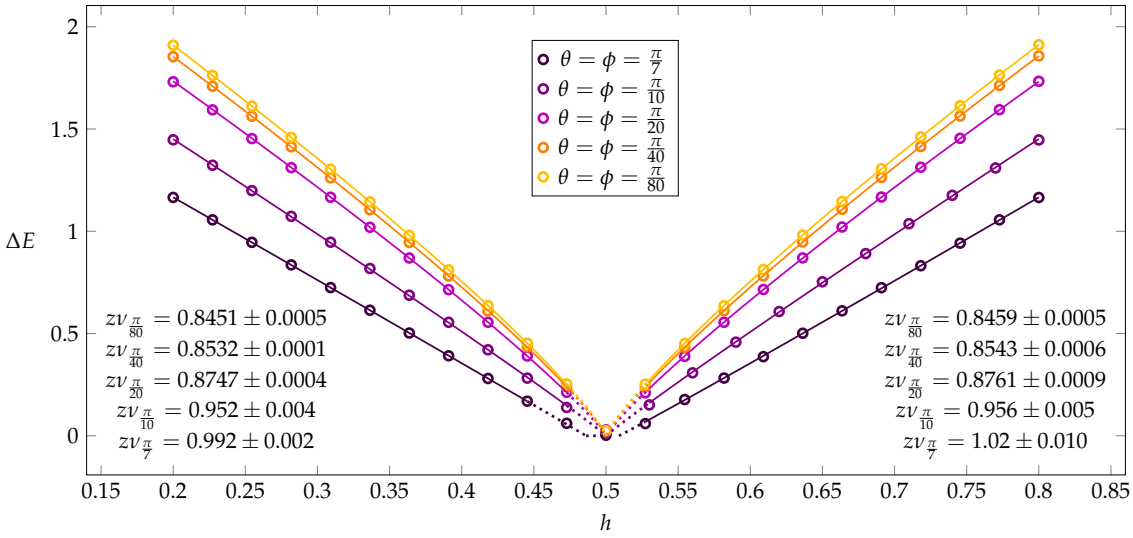

Figure 4.17: Fit of the energy gap near criticality at small angles in the self-dual case and critical exponents. For this plot we have considered chain lengths of $L = 99$ sites.

Case (ii). When $\theta \neq 0$ and $\phi = 0$ time reversal symmetry is preserved, parity is broken and the self-duality is lost. The topology of the phase diagram is well understood from the literature [85] and it is sketched in Fig.4.18(a). We have decided to study the energy gap as a function of h with an angle $\theta = 0.9$. Here we expect to capture the usual three phases characterising these models, but now the resulting plot will not be symmetric around $h = 0.5$. We show the plot of the energy gap in Fig.4.18(b). From the plot, without performing any scaling, we may approximately locate the Pokrovsky-Talapov transition at $h \approx 0.15$ and the BKT one at $h \approx 0.6$. We mention that for this particular setup we will not address the issue of the existence of a Lifshitz point, but the same ambiguities as before hold true even in this case.

Case (iii). The last case we have studied is the one with $\phi \neq 0$ and $\theta = 0$. Here parity is preserved, time reversal is broken and the self-duality of the model is again lost. It is interesting to notice that, given the symmetry of the phase diagram under the simultaneous exchange of the phases and of the couplings, we are now in a situation which is "mirrored" with respect to the one we have just described for *case (ii)*, as we also see from Fig.4.19(a). In order to further highlight this symmetry of the phase diagram, we have studied the energy gap as a function of h with an angle $\phi = 0.9$. From the plot in Fig.4.19(b) we may approximately locate the Pokrovsky-Talapov transition at $h \approx 0.6$ and the BKT one at $h \approx 0.15$, again consistently with what we have previously found. Even in this case we do not address the issue of the existence of a Lifshitz point.

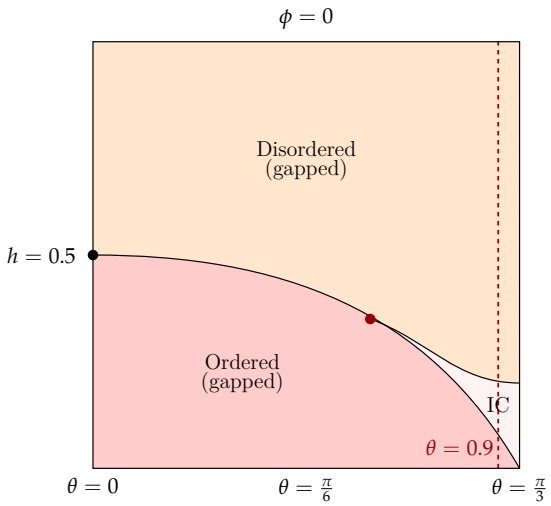

(a) Phase diagram

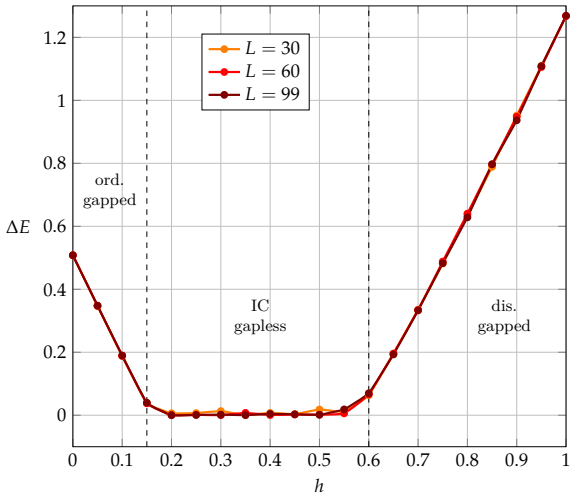

(b) Plot of the energy gap for $\theta = 0.9$ and $\phi = 0$

Figure 4.18: On the left we draw a sketch of the phase diagram of the 3-state chiral clock model with $\theta \neq 0$ and $\phi = 0$ showing the three different phases (in different colours) and the putative Lifshitz point (in red). On the other side we show the plot of the energy gap as a function of h for $\theta = 0.9$ which reveals the three different phases with the critical one in between.

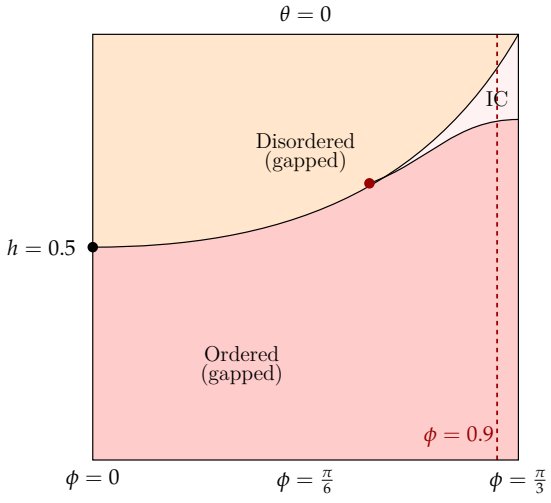

(a) Phase diagram

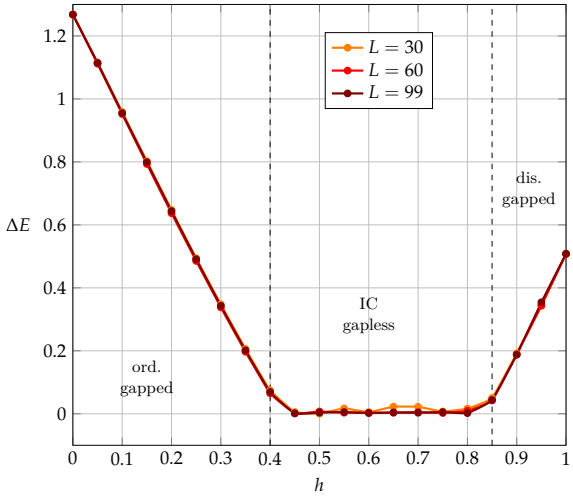

(b) Plot of the energy gap for $\phi = 0.9$ and $\theta = 0$

Figure 4.19: On the left we draw a sketch of the phase diagram of the 3-state chiral clock model with $\phi \neq 0$ and $\theta = 0$ showing the three different phases (in different colours) and the putative Lifshitz point (in red). On the other side we show the plot of the energy gap as a function of h for $\phi = 0.9$ which reveals the three different phases with the critical one in between.

Before concluding this discussion we want to provide some details about the explicit computation of the energy gap. In this respect we show in Fig.4.20 the energy levels of the 3-state chiral clock model for a given L. We immediately see that the chirality has the effect of shifting the energy levels in the different symmetry sectors with respect to what we have seen in the symmetric case. Indeed, in the disordered paramagnetic case the first excited state does no longer live within $Q = 1$, but within $Q = 2$. Therefore, we have computed the energy gap as the difference between the energy eigenvalues of the sectors $Q = 2$ and $Q = 0$. Within the incommensurate phase the situation is more peculiar, as the true ground state actually changes symmetry sector as h changes. In other words, we have found evidence of level-crossing within the incommensurate phase, thus we have consequently computed the energy gap checking the right symmetry sector for each value of h.

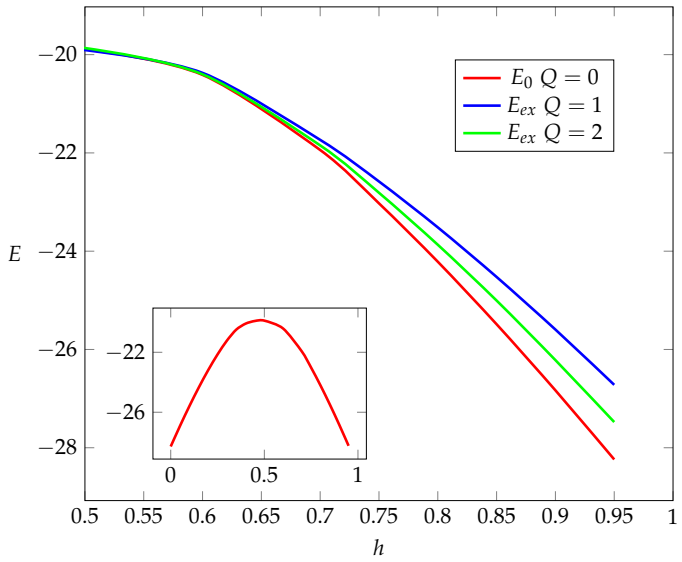

Figure 4.20: Plot of the energy levels of the 3-state chiral clock model with $J = 1 - h$, $\theta = \phi = \frac{\pi}{4}$ and $L = 21$. It shows that introducing a chirality in the model has the effect of shifting the energy levels. For $L = 21$, in the disordered phase the ground state is again within the $Q = 0$ symmetry sector, but now the first excited state lives in the one with $Q = 2$. In the miniature we show the profile of the ground state throughout the three phases, with h running from 0 up to 1.

The level-crossing which seems to characterise these models also reveals itself in a peculiar pattern of oscillations displayed by the energy gap as a function of the chain length. Let us now discuss it more in detail.

4.5.2 Lifshitz oscillations

As we have already anticipated, we have found evidence of oscillations in the plot of the energy gap as a function of the chain length L, whose origin seems to be traced to level-crossing of the ground states in the three symmetry sectors. Before presenting our analysis we mention that in the literature there are some works [82, 85] which are already familiar with these *Lifshitz oscillations*. Still, their origin seems to be not fully understood. Zhuang *et al.* have found evidence of oscillations in the plots of the energy gap and of the entanglement entropy and focused their attention mostly on the latter. They have studied the dependence of the oscillation length ℓ as a function of the angle θ proposing the empirical relation $\ell = \theta^{-3.75} + 1.16$. They have also noticed that the pattern of oscillations in the entanglement entropy disappears when enforcing periodic boundary conditions, consistently with the literature about some free fermions models [67]. On the other hand, Whitsitt *et al.* have confirmed the results of the previous work and produced further evidence which seems to support the scenario of phase transition occurring through a narrow sliver of the incommensurate phase extending all the way down to the 3-state Potts point at $\theta = \phi = 0$ along the line $h = J = 0.5$.

Thus, we have stuck to the self-dual *case (i)* with $\theta = \phi = 0.4$ and focused our attention mainly on the critical $h = 0.5$ [85]. We have firstly studied the energy gaps between the energy levels in the three symmetry sectors $Q = 0,\ 1,$ and 2, which are plotted in Fig.4.21(a), (b) and (c). Interestingly, the ground states oscillate all with the same periodicity of $\ell \approx 51$ sites. Moreover, the minima appearing in these plots actually correspond to points of level-crossing, thus they should be considered as zeros. In other words, the gap closes at these points, as it is manifest from Fig.4.22.

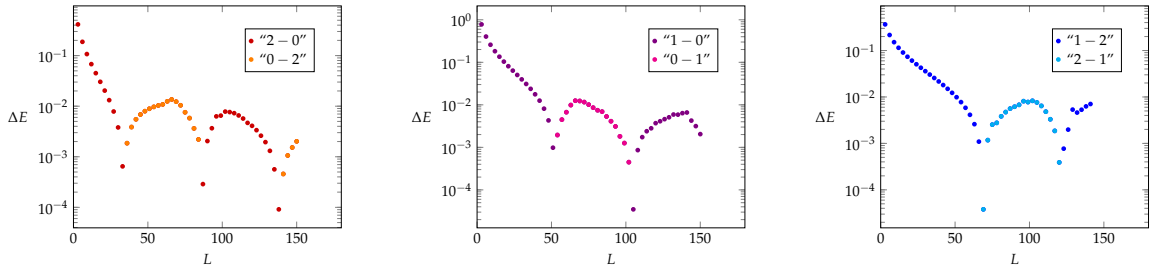

(a) $|E(Q=0) - E(Q=2)|$ **(b)** $|E(Q=0) - E(Q=1)|$ **(c)** $|E(Q=1) - E(Q=2)|$

Figure 4.21: Oscillations of the energy gaps of the 3-state chiral clock model in the different symmetry sectors as a function of L. The different ground states oscillate all with the same periodicity: $\ell \approx 51$. We stress that the minima correspond to the points of level-crossing.

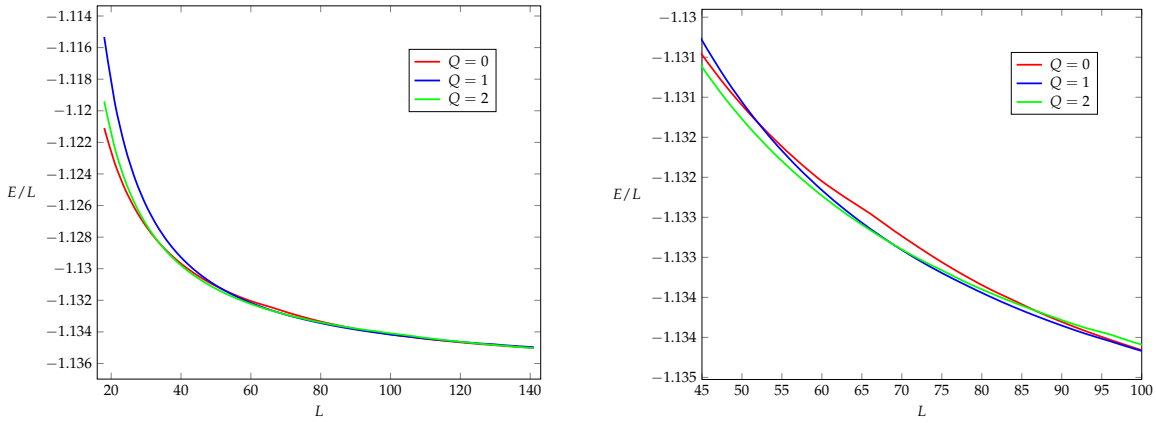

Figure 4.22: Oscillations in the energy levels of the 3-state chiral clock model with $\theta = \phi = 0.4$. Reading the plot on the left: when L is small the true ground state has $Q = 0$ and the first excited state has $Q = 2$, then at $L = 33$ they get exchanged, with the sector in $Q = 2$ becoming the ground state and the one in $Q = 0$ the first excited state. After, at $L = 51$ the energy level in $Q = 1$ crosses the one in $Q = 0$ becoming the new first excited state, and so on. Thus this plot shows evidence of level crossing between the ground states in the different sectors, explaining the oscillating pattern of the energy gap. On the right we show a magnification of the same plot.

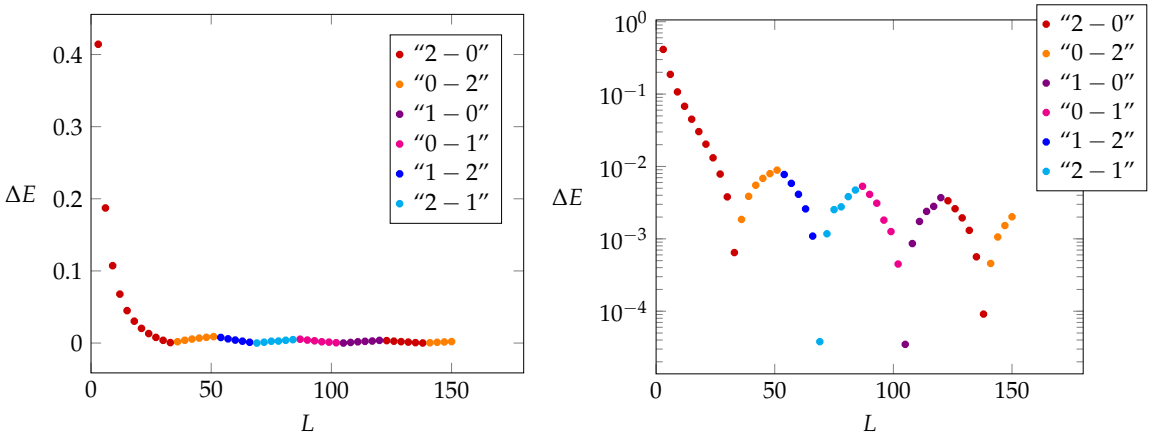

(a) Linear scale.

(b) Logarithmic scale.

Figure 4.23: Oscillations of the energy gap of the 3-state chiral clock model with $\theta = \phi = 0.4$ as a function of the chain length L. Both normal (left) and logarithmic (right) scale are shown in order to better appreciate the pattern of oscillations. The same colour convention of Fig.4.21 has been used to highlight the role played by all the ground states in the three symmetry sectors in the definition of the true energy gap. The change of sectors takes place with a periodicity of about 6 points, corresponding to 18 sites.

The plot of of the energy levels (normalised by the chain length) as a function of L indeed shows evidence of level-crossing between the ground states of the different symmetry sectors which oscillate periodically, thus giving rise to the oscillating pattern already shown in Fig.4.21. A possible explanation for level-crossing along the critical line $h = 0.5$ and within the incommensurate phase may be traced to the competition between the finite size of the system, the symmetry constraints and - most of all - the chirality of the model. Thus, for different values of L it may be more favourable for the system to relax within a given symmetry sector rather than the others, this explaining the interplay of all the three ground states. Moreover, this has allowed us to reconstruct the plot of true energy gap, which also display an oscillating pattern as it is shown in Fig.4.23(a) and (b) where the same colour convention of Fig.4.21 has been used. The oscillation length for of the energy gap in the present conditions is $\ell = 33$ sites, which is consistent with the one obtained by Zhuang *et al.*.

We conclude the discussion of the Lifshiftz oscillations of the energy gap with two observations. First of all, we recall that in the symmetric case $\theta = \phi = 0$ no oscillation is visible in the plot of the energy gap. Moreover, no oscillation is visible in the chiral case slightly out of criticality, for example at $h = 0.4$ and $h = 0.6$, either. Thus, we may quite safely conclude that this oscillating pattern is peculiar to the $h = 0.5$ line. It is also possible that these oscillations are related to the nature of the critical line itself, which - we recall - may either host a one-step transition living in the chiral universality class, or a two-step one proceeding through an incommensurate film so thin to be practically impossible to reveal without ambiguity. For example we recall that we have found evidences of level-crossing within the incommensurate phase as well. However, in this regard it may be worth mentioning that in Ref. [34] Hoeger *et al.* have found evidences of level-crossing in the XY-model and suggest that oscillating patterns in the energy gap are peculiar of phases with non-vanishing wave vector, like both IC phase and chiral transition are. Yet, in our opinion the hypothesis of competition between the chirality of the model and the symmetry constraints seems to be more likely. In fact, the opening and closing of the energy gap along the same critical line for different system sizes has all the appearance of a spurious effect which may not be there in the thermodynamic limit.

The second and last observation is that we have also considered the energy gap under periodic boundary conditions up to $L = 99$ sites only. We have already mentioned that according to the literature the oscillations in the entanglement entropy disappear when periodic boundary conditions are enforced. Interestingly

enough, the energy gap still seems to oscillate with a different periodicity. However, given that DMRG becomes less solid and runs much slower when working with PBC, we defer this issue to future and more accurate simulations.

4.5.3 Entanglement entropy

A second physical observable which may provide useful information about the topology of the phase diagram of the transverse 3-state chiral clock model is the entanglement entropy. We do not intend to be exhaustive here as an in depth study of the entanglement entropy has already been carried out in Ref. [85]. Thus, we have simply studied the half-chain entanglement entropy in the self-dual case for $\theta = \phi = \frac{\pi}{4}$, as for this particular choice of the angles we already known the approximate location of the critical boundaries of the incommensurate phase. We stress that we have computed the entanglement entropy over the true ground state of the system, i.e. considering level-crossing within the critical phase, which is sometimes difficult to deal with. Also, the uncertainties on the data especially close to the boundaries of the incommensurate phase are usually large, as they are affected by multiple technical issues. With these caveats, we shown in Fig.4.24 the resulting plot. We see that for $0.34 \lesssim h \lesssim 0.66$ the entanglement entropy scales with the system size, implying that within that range of parameters the phase is critical. Also, the entropy is constant for $h \lesssim 0.34$ and it goes to zero for $h \gtrsim 0.66$, meaning that in the strong field regime the states become unentangled product states. In the inset we show a magnification of the same plot in a vicinity of the BKT transition, where the curves of the entanglement entropy seem to cross all at the same point $h \approx 0.66$. This seems to suggest that for the second IC-C transition the entanglement entropy behaves as a sort of “order" parameter. In fact, the incommensurate phase is not ordered in the standard sense, but it is expected to display an “ordered" pattern given by the different domain walls, whose size depend on all the parameters of the model, namely θ, ϕ, L and of course h. This is indeed different from the gapped commensurate phase which is paramagnetic in nature. We do not present here any study of the central charges because they are extremely sensible - even with $O(1)$ errors - to the location of the critical points and we do not known the exact location of the two C-IC phase transitions in the thermodynamic limit. A quantitative evaluation of the errors on the central charges slightly out of criticality is shown in Ref. [85].

We also mention that we have found evidences of oscillations in the curves of the entanglement entropy when open boundary conditions are enforced, consistently with the literature. Yet, it is extremely difficult to venture an hypothesis about

the possible relation between these oscillations and the pattern of oscillations we have just discussed for the energy gap. Due to the fact that the energy gap seems to oscillate even when periodic boundary conditions are enforced and that the numerical curves of the entanglement entropy at criticality are obtained with finite bond dimensions - and thus they are plagued by finite-size effects -, it is also possible that these oscillations have a different origin.

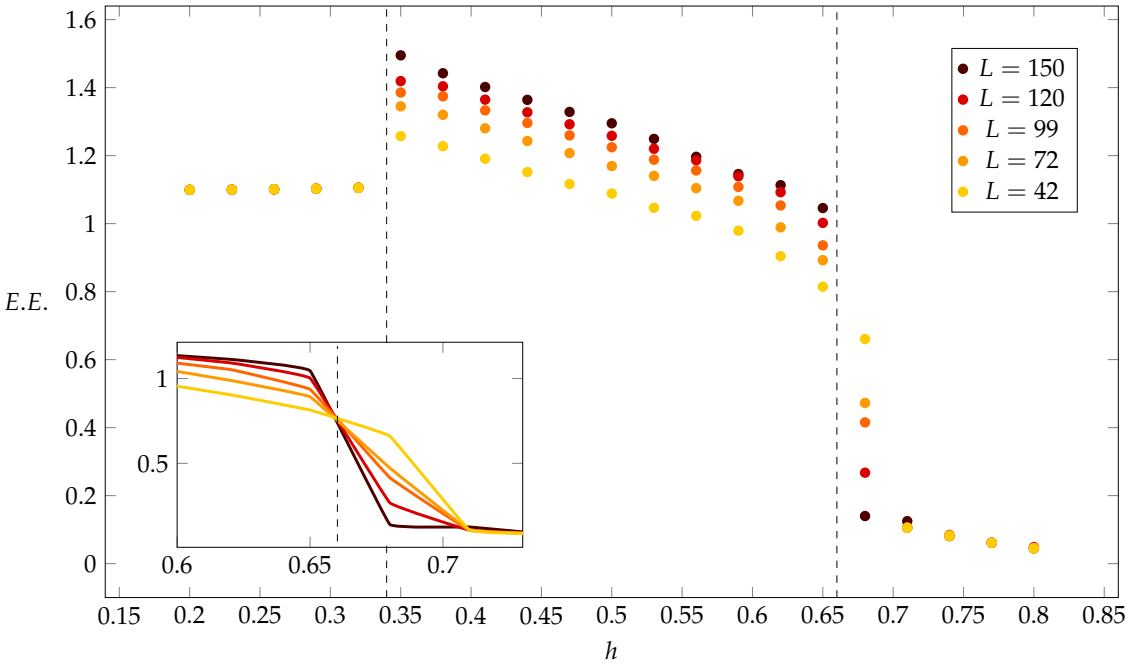

Figure 4.24: Half chain entanglement entropy of the 3-state chiral clock model (OBC) at different chain lengths. For $0.34 \lesssim h \lesssim 0.66$ the entropy scales with L, consistently with the critical nature of the floating incommensurate phase. Inset: same plot of the entanglement entropy in a vicinity of the BKT transition, where all the curves seem to cross at the critical point. This behaviour is typical of order and disorder parameters.

Finally, we mention here that in the following we shall not present the finite-size scaling analysis of the magnetisation for the 3-state chiral clock model as this is spoilt by the chirality. We just mention that the usual order parameter is in principle able to capture only the first C-IC phase transition, as here the system passes from an ordered configuration to a disordered one. However, we may invoke duality considerations and investigate the second IC-C transition with the dual disorder parameter. Thus, both the order and disorder parameters will be zero within the incommensurate phase, consistently with the self-duality of the model when $\theta = \phi$. We also mention that within the IC phase further evidence of level-crossing have been found.

4.5.4 Correlation functions at criticality

We conclude the study of the transverse 3-state chiral clock model by turning the attention on the correlation functions within the incommensurate phase.[5]. This phase is critical and floating incommensurate, thus at large distance we expect the correlation functions to display an algebraic power-law decay with some complex modulation $\sim e^{i(k-k_0)\cdot r}$, for some incommensurate wave vector k. Indeed, the former is typical of criticality, the latter of floating IC phases. Thus we have studied separately the absolute value, the real and imaginary parts of the correlators in order to capture this special behaviour. A specific - but yet paradigmatic - example for $\theta = \phi = \frac{\pi}{4}$ at $h = 0.5$ is shown in Fig.4.25.

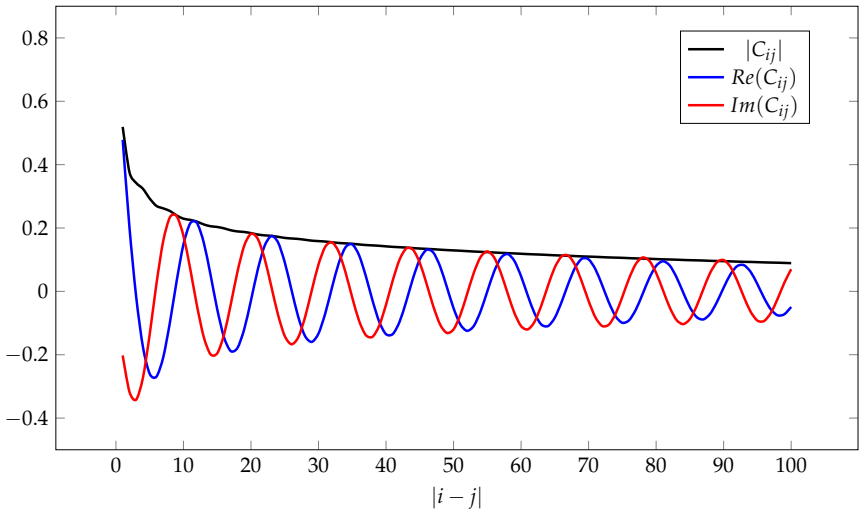

Figure 4.25: Absolute value, real and imaginary part of the correlation functions of the 3-state chiral clock model within the IC phase. The former displays a power law decay typical of criticality. Instead, the real and imaginary parts reveal a pattern of oscillations with a power-law damping.

As expected, both the plots of the real and imaginary parts reveal an oscillating pattern with a power-law damping shifted in relation to each other. Thus, in this context correlation functions provide useful information not only about the nature of the phase transitions via their critical exponents, but they also allow us to extract the incommensurate wave vector characterising both the critical phase and its critical boundaries. Therefore, we have investigated more deeply the dependencies of the wave vector k on the magnitude of the transverse field h and on the angle

[5]We do not take into account correlators within the two gapped phases, because there we expect nothing new compared with the non chiral case, which we have already studied

$\theta = \phi$, as we stick to the self-dual case as usual. We show in Fig.4.26 and 4.27 the real and imaginary parts of the correlation functions for different values of h and θ, respectively.

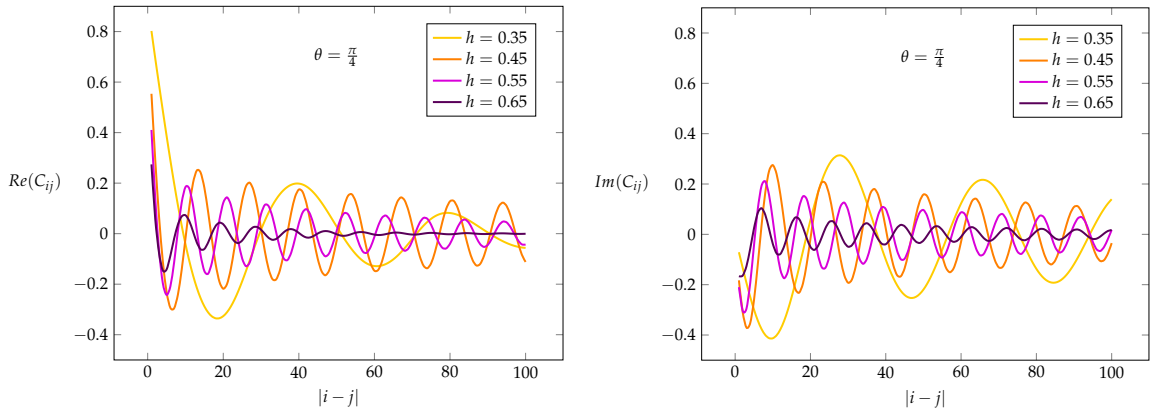

(a) Real part. **(b)** Imaginary part

Figure 4.26: Correlation function of the 3-state chiral clock model for different values of h within the IC phase. They are coloured by increasing values of the wave vector k.

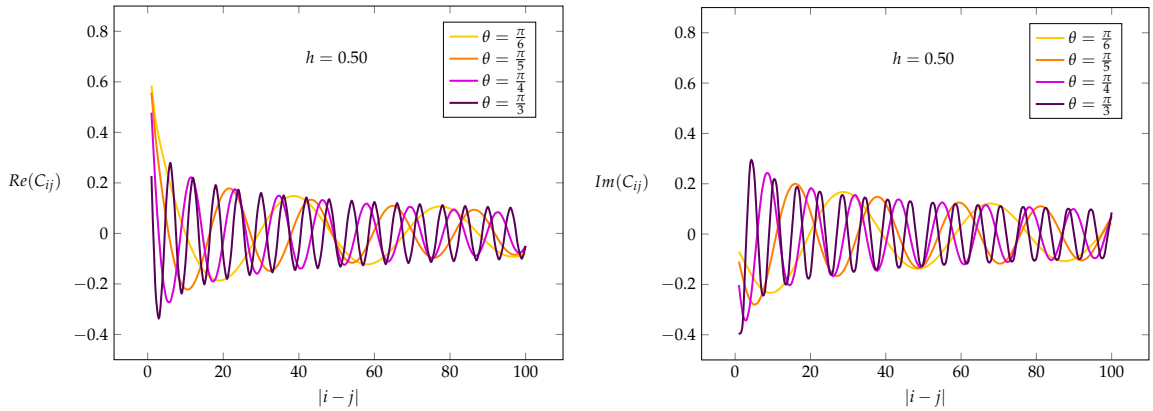

(a) Real part. **(b)** Imaginary part

Figure 4.27: Correlation function of the 3-state chiral clock model for different values of θ within the IC phase. They are coloured by increasing values of the wave vector k.

We have then extracted the value of the wave vector from the fit of the real and imaginary parts of the correlators, considering only sites from $1/4$ to $3/4$ of the chain in order to avoid finite-size effects and using the following functional dependence:

$$f(|i-j|) = p3 \cdot \frac{\exp(-|i-j| \cdot p4)}{|i-j|^{p0}} \cdot \cos(p1 \cdot |i-j| + p2 \cdot \pi) \; . \tag{4.4}$$

The parameter $p0$ rules the power-law decay, $p1$ is the incommensurate wave vector we are interested in, $p2$ is a phase, $p3$ is a multiplicative constant and $p4$ is the inverse of the correlation length, which is expected to be zero as the phase is gapless.

Let us discuss in detail the results. We have started from the case $\theta = \phi = \frac{\pi}{4}$, for which we already know the approximate location of the critical points. We show in Fig.4.28(a) and (b) the plots of the incommensurate wave vector and the oscillation length as a function of h. From the former we learn that the wave vector is zero in the gapped ordered phase, then it starts growing within the incommensurate phase, it reaches a maximum at the BKT transition and then it jumps to zero again in the gapped disordered phase, supporting the hypothesis of phase transitions occurring at $h \approx 0.34$ and $h \approx 0.66$. Also, we see that the oscillations become faster and their length ℓ decreases as h increases within the critical phase. Such a behaviour is consistent with Fig.4.28(b) and with the literature [4]. Then, by restricting ourselves to a vicinity of the first critical point and performing a fit of the data we have extracted the critical exponent $\overline{\beta}$. The Pokrovsky-Talapov theory predicts $\overline{\beta} = 1/2$, which has to be true all along the critical line separating the ordered phase from the incommensurate one. Thus, we have chosen two different angles, $\theta = \frac{\pi}{4}$ and $\theta = \frac{\pi}{5}$ (see Fig.4.29(a) and (b)), finding $\overline{\beta} = 0.507 \pm 0.016$ and $\overline{\beta} = 0.508 \pm 0.009$, respectively. In both cases our results are fully consistent with the theoretical prediction.

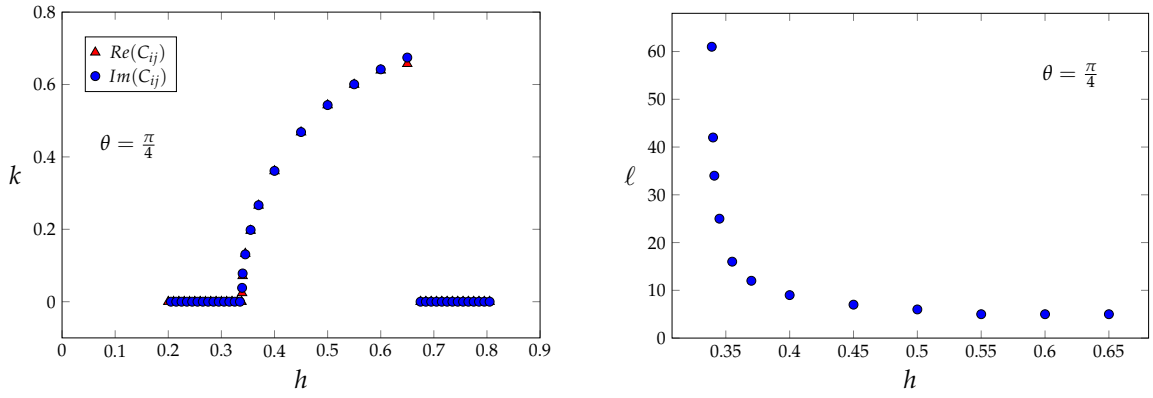

(a) k vs h **(b)** ℓ vs h

Figure 4.28: Wave vector k and oscillation length ℓ as a function of h. Both the plots have been obtained at $\theta = \phi = \frac{\pi}{4}$. The values of k have been extracted from the fit of the correlators considering both the real and imaginary part and no significant difference between the two has been found. There is only a small discrepancy in the left plot for $h \approx 0.34$ and $h \approx 0.66$, which is likely due to the fact that these points are very close to the phase transitions. For the oscillation length we have found no distinction between the real and imaginary parts of the correlators. It decreases as h increases until it stabilises to $\ell \approx 5$ sites starting from $h = 0.55$.

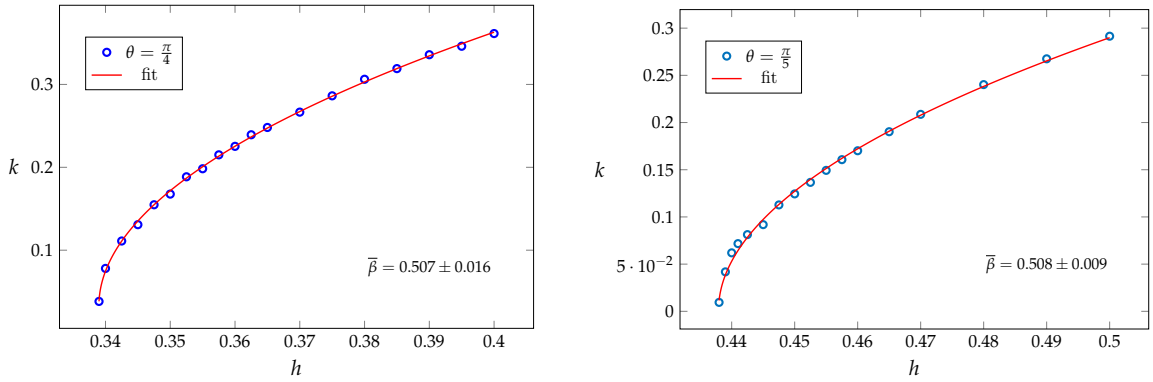

(a) $\theta = \frac{\pi}{4}$ **(b)** $\theta = \frac{\pi}{5}$

Figure 4.29: Incommensurability exponent at Pokrovsky-Talapov for $\theta = \frac{\pi}{4}$ and $\frac{\pi}{5}$. In both cases we have found values which are fully consistent with the nominal $\overline{\beta} = 1/2$.

Now that we have investigated the h-dependence of the correlation functions, we can start discussing the dependence on the angle $\theta = \phi$. We draw in Fig.4.30(a) and (b) the plots showing the angular dependence of the wave vector and the oscillation length, respectively. As before, we have extracted k from the fit of both the real and imaginary part of the correlation functions, although no significant difference is found between the two. Instead for the oscillation length the agreement is perfect, thus we have not distinguished between the two cases. The plot in Fig.4.30(a) shows that the wave vector increases with the angle θ along the critical line $h = 0.5$. We recall that here we are computing the correlators over chains of length $L = 201$ and then fitting within a range of 100 sites. Under these conditions, the latest oscillations are detected at $\theta = 0.35$ with wave vector $k \approx 0.0325$. However, we have found that by increasing the chain length up to $L = 300$, so to compute the correlation functions within a larger range of 150 sites, we are able to detect oscillations down to $\theta = 0.30$ with $k \approx 0.0194$. This implies that for smaller angles the oscillation length becomes larger than the range we are considering for computing the correlators, so that the oscillations are not visible, but they are still there. Interestingly enough, the analysis of the oscillations of the energy gap shows some resemblance with what we have found here for the correlation functions. Indeed, Zhuang *et al.* claim that the oscillation length of the energy gap becomes larger than the size of the system they are considering ($L = 200$) at $\theta = \frac{\pi}{12} \approx 0.262$, which is not too far from our value of $\theta = 0.30$ for a range of 150 sites. On the other hand, from Fig.4.30(b), we learn that ℓ decreases as θ increases. More precisely, a fit of the data reveals the following empirical relation: $\ell \sim 1.69 \cdot \theta^{-3.66} + 1.7$. Again, it is interesting to make a comparison between these results and those known from the literature about the

energy gap. In this regard, Zhuang *et al.* have also found for the oscillation length associated with the oscillations of the energy gap and the entanglement entropy the empirical relation $\ell \sim \theta^{-3.75} + 1.16$. Their exponent ruling the algebraic decay in θ, -3.75, is very similar to our -3.66 ± 0.06, which may be more than a coincidence as they differ only by 2.5%. Yet, for a more accurate comparison we should sample more data and check whether the agreement improves or gets worse.

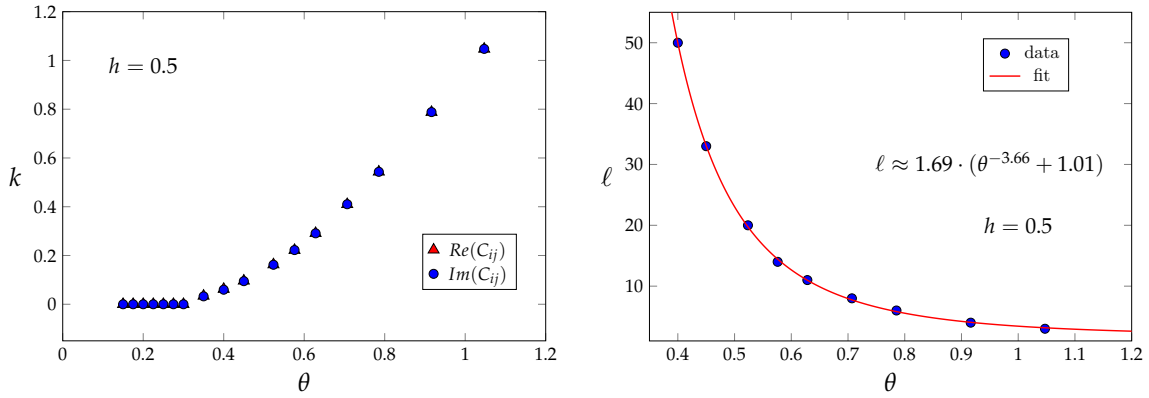

(a) k vs θ **(b)** ℓ vs θ

Figure 4.30: Plots of the wave vector k and of the oscillation length ℓ as a function of θ. Both the plots have been obtained at $h = 0.5$, i.e. right in the middle of the incommensurate phase. The values of k have been extracted from the correlators considering both the real and imaginary part, without significant difference between the two. For ℓ the two data coincide perfectly. For the dependency of ℓ on θ we propose an empirical relation.

Unfortunately, the picture resulting from our numerical analysis is consistent both with the the scenario of a thin incommensurate layer extending down to $\theta = \phi = 0$ and with the hypothesis of a Lifshitz point. In particular we have found evidences of oscillations in the correlators at small angles. Yet, we recall that chiral transitions are characterised by a wave vector just like the incommensurate phase is, thus we expect the correlation functions to oscillate there as well. Also, we have said in the previous chapters that a chiral transition is non-conformal, i.e. $z \neq 1$, and it is characterised by the equality $\overline{\beta} = \nu$. But, as we have understood, this is true for the Pokrovsky-Talapov transition as well. Thus, with our approach based on DMRG simulations and extractions of critical exponents, the only possible way of detecting such a transition is to reveal an abrupt change in the value of the incommensurability exponent $\overline{\beta}$ across the putative Lifshitz point $\theta = \phi = \frac{\pi}{6}$. We have therefore tried to extract $\overline{\beta}$ like we have done at the Pokrovsky-Talapov transition. Namely, we have sat at angles $\theta = \phi = 0.35,\ 0.45$ and 0.50 and tried to approach the phase transition

both from the ordered and disordered phase by studying the wave vector. In doing so we have ended up with two kinds of technical problems. The first is that there are evidences of oscillations in the correlation functions slightly off criticality both in the ordered and disordered phase, but it is possible to say whether these oscillations are physical, and therefore reliable for our analysis, or simply distortions induced by the nearby critical line. The second problem is that when the angles are small the oscillation length of the fluctuations gets large, sometimes - like for $\theta = 0.35$ - even larger that the range within which we are fitting. Therefore the data for the wave vector, which is very small, suffer a large uncertainty. All these effects spoil the analysis of the incommensurabilty exponent so that we cannot provide viable results.

4.5.5 Binder cumulant

Let us now review what we have found so far about the critical line $h = 0.5$ at small angles, always sticking to the self-dual case. We have firstly studied the energy gap to extract the critical exponent $z\nu$, as both the chiral and Pokrovsky-Talapov transitions are non-conformal. Due to the values of the critical exponents of these two universality classes, if a Lifshitz tricritcal point is present, the quantity $z\nu$ is not sensitive to it, as for both transitions we expect $z\nu = 1$. However, as the angle $\theta = \phi$ decreases, a rather smooth dependence was found, resulting in $z\nu \leq 1$. Afterwards, we have studied the oscillating behaviour of the energy gap and of the correlation functions. The former may be traced to the presence of level-crossing and it does not provide any quantitative information about the universality class of the transition. The latter has instead allowed us to extract the incommensurate wave vector together with its incommensurability exponent for the Pokrovsky-Talapov transition but not for the one occurring at small angles for $h = 0.5$.

Let us now make one final attempt by studying the exponent ν which is expected to be sensitive to any change between the two universality classes (cfr. Tab.1.1). Instead of computing it by fitting the correlation functions to extract the correlation length, it is much easier to consider the fourth-order Binder cumulant (4.2). Its finite-size scaling indeed depends only on ν, as we have already seen. Thus, we have proceeded as follows: upon enforcing periodic boundary conditions, we have firstly computed U_L as a function of h for different values of L and for different angles $\theta = \phi < \frac{\pi}{6}$. The plots have revealed that the curves all cross at a single point which is consistent with $h_c = 0.5$ (see Fig.4.31 for $\theta = \phi = \frac{\pi}{10}$). Instead, for $\theta = \phi > \frac{\pi}{6}$, where the incommensurate critical phase is already open, the curves of the Binder parameter suffer an abrupt jump and display a sort of staircase behaviour.

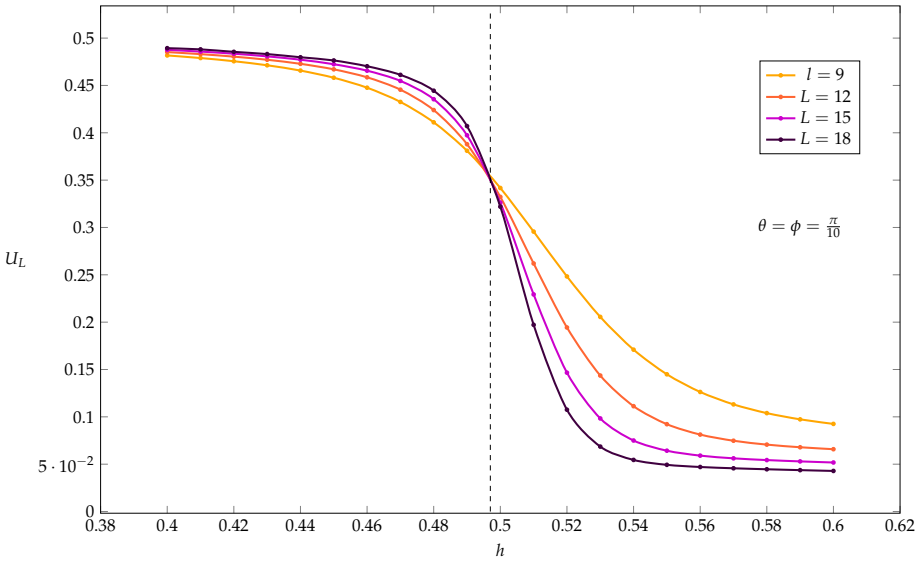

Figure 4.31: Binder cumulant for the 3-state chiral clock model with $\theta = \phi = \frac{\pi}{10}$. All the curves cross at a single point which is consistent with the nominal value $h_c = 0.5$. A very similar plot has been found for $\theta = \phi = \frac{\pi}{40}$ as well.

Therefore, we have focused our attention on the former case only. Afterwards, we have performed the finite-size scaling analysis for three different angles, namely $\theta = \phi = \frac{\pi}{40}$, $\frac{\pi}{10}$ and $\frac{\pi}{7}$. Thus, we have studied the behaviour of U_L as a function of $L^{1/\nu}(h - h_c)$ considering both $\nu = 1/2$ (Pokrovsky-Talapov) and $\nu = 2/3$ (chiral) in order to see in which case all the curves collapse on a single universal curve. For $\nu = 1/2$, we have found that the curves do not collapse. Instead, for $\nu = 2/3$ they do, at least for $\theta = \phi = \frac{\pi}{40}$ and $\frac{\pi}{10}$. The resulting plots are shown in Fig.4.32(a), (b) and (c). We stress that in the first two cases $h_c = 0.5$ has been used, whereas in the last one we have chosen $h_c = 0.4862$, which is the value we have found from the previous analysis of the energy gap.

All these results seem finally to suggest that the transition occurring at small angles for $h = 0.5$ may be chiral in nature. However, we also have to mention that for $\theta = \phi = \frac{\pi}{7}$ with $\nu = 1/2$ the curves of the Binder parameter do not collapse either. This may due to our ignorance about the exact location of the transition point in the thermodynamic limit, as we recall that the value $h_c = 0.4862$ was just an estimate from the fit under a specific setup ($L = 99$ with OBC). Another possibility is that the thin incommensurate phase we have previously observed for $\theta = \phi = \frac{\pi}{7}$ actually closes in the thermodynamic limit. This would be also supported by the following observation: instead of using $h_c = 0.4862$ as critical value for the scaling, if we insist in considering $h_c = 0.5$, then all the curves of the Binder cumulant collapse onto the

same universal curve with the same chiral critical exponent $\nu = 2/3$, just like we have seen for the smaller angles $\theta = \phi = \frac{\pi}{40}$ and $\frac{\pi}{10}$. By the way, this would also be consistent with the theoretical location of the Lifshitz point at $\theta = \phi = \frac{\pi}{6}$.

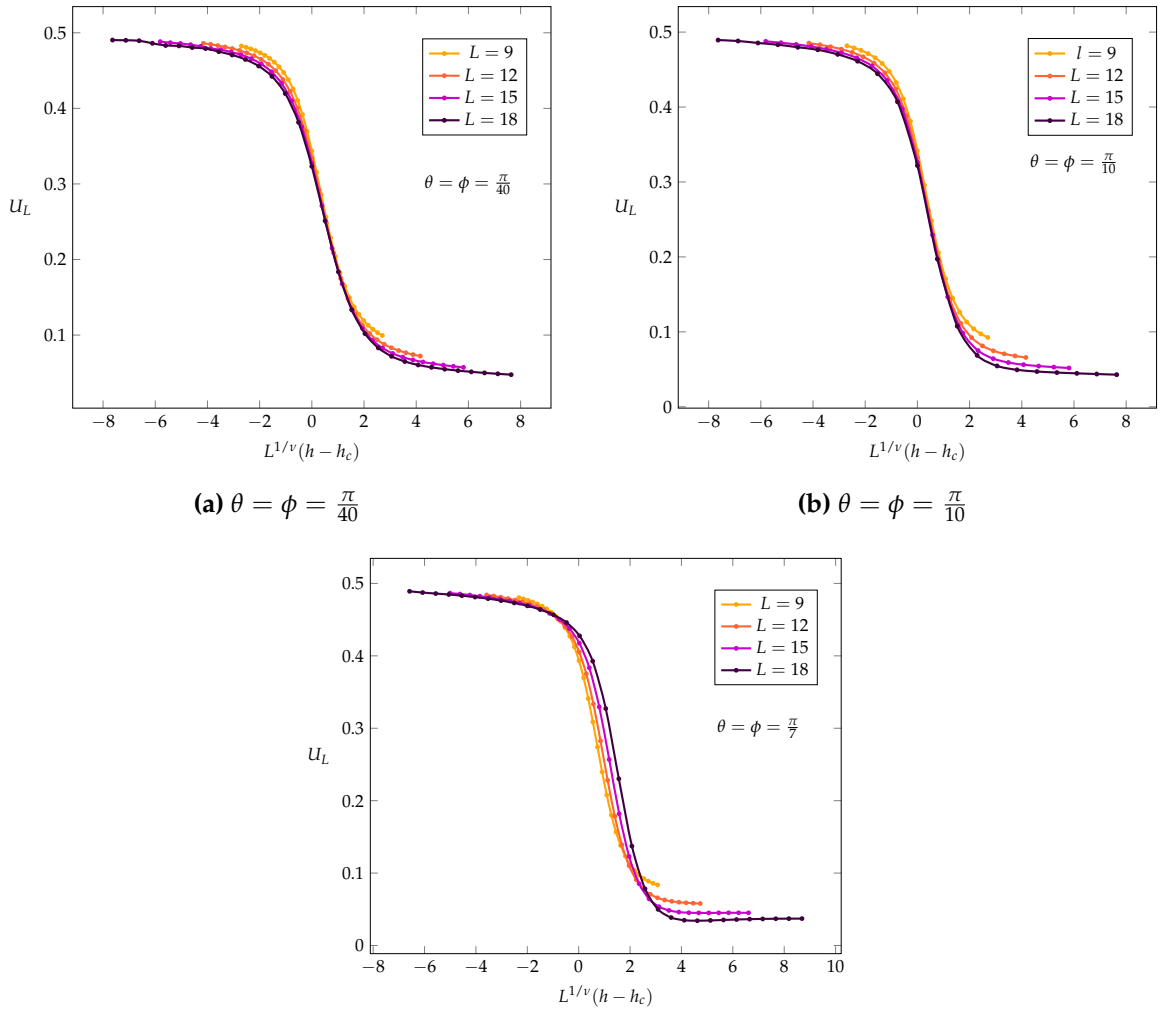

(a) $\theta = \phi = \frac{\pi}{40}$

(b) $\theta = \phi = \frac{\pi}{10}$

(c) $\theta = \phi = \frac{\pi}{7}$

Figure 4.32: Universal scaling of the Binder cumulant for the self-dual 3-state chiral clock model (PBC) assuming $\nu = 2/3$ (chiral transition). For $\theta = \phi = \frac{\pi}{40}$ and $\frac{\pi}{10}$ all the curves correctly collapse into a single universal one in a vicinity of the critical point. Instead for $\theta = \phi = \frac{\pi}{7}$ they do not as they still cross themselves. In the first two cases we have used $h_c = 0.5$, whereas in the last one $h_c = 0.4862$ (cfr. Fig.4.17).

4.6 Adding a longitudinal field

In this last section we apply a longitudinal field to 3-state clock models, both symmetric and chiral, on top of the standard transverse one. The literature for this particular configuration is not so rich. So let us proceed, as usual, by closely following the Ising model, which is instead largely studied in all its configurations.

We have already recalled in the previous chapters that the transverse Ising model is integrable via Jordan-Wigner transformation. By applying to the model also a longitudinal field (cfr. Hamiltonian (1.60)), we find that such a term cannot be mapped into a local fermion operator and therefore it introduces a non-local interaction between fermions. Thus, the Ising model with both transverse and longitudinal fields is not integrable [55]. In addition to the integrability-breaking effect, a longitudinal field is also known to remove the critical point occurring in the ferromagnetic transverse Ising model at $h_x = 1$. Thus, the phase diagram of this model is completely gapped for any non-zero value of the longitudinal field and the only lack of analiticity in the ground state energy occurs at $(h_x = 1, h_z = 0)$.

4.6.1 Phase diagram

Since we are introducing a new parameter in the Hamiltonian, namely the magnitude of the longitudinal field, h_z, the phase diagrams of these models will become one dimension higher. We shall therefore study the two-dimensional (h_x, h_z) phase diagram, which for the 3-state symmetric model is the entire phase diagram itself, whereas for the 3-state chiral model it is just a section for a particular choice of the angles θ and ϕ, given $J = 1 - h_x$.

Let us start by discussing the 3-state symmetric clock model (2.8). We show in Fig.4.33(a) the plot of the energy gap as a function of h_x for different values of the longitudinal field h_z and in Fig.4.33(b) the resulting two-dimensional phase diagram mapped via the energy gap. Both the plots have been obtained enforcing open boundary conditions on a chain of length $L = 99$ sites. We have found that the critical point occurring in the transverse clock model gets immediately removed as far as the longitudinal field is switched on. For example, by applying a weak longitudinal field $h_z = 0.001$, the energy spectrum is already completely gapped. This picture is consistent with what we have previously discussed for the Ising model, which makes sense as the 3-state Potts model is its simplest generalisation [6].

[6] Compare for example our Fig.4.33(b) with Fig.1(a) in Ref. [78].

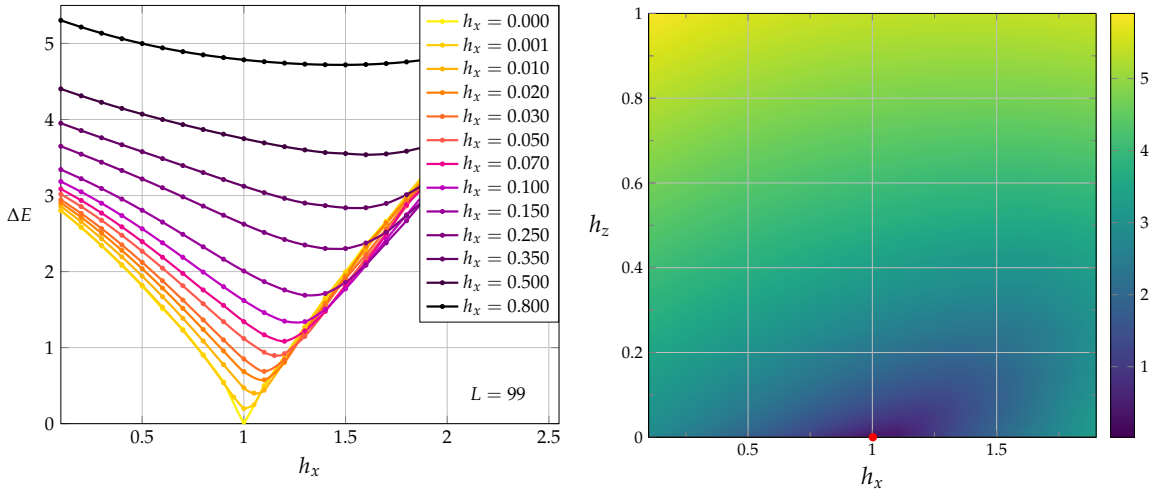

(a) Energy gap vs h_x **(b)** Phase diagram

Figure 4.33: Phase diagram of the 3-state symmetric clock model with both transverse and longitudinal field for $L = 99$ (OBC). On the left we see the plot of the energy gap for different values of the longitudinal field. On the right we show the resulting two-dimensional phase diagram mapped via the energy gap. It has only one critical point occurring at $(h_x = 1, h_z = 0)$.

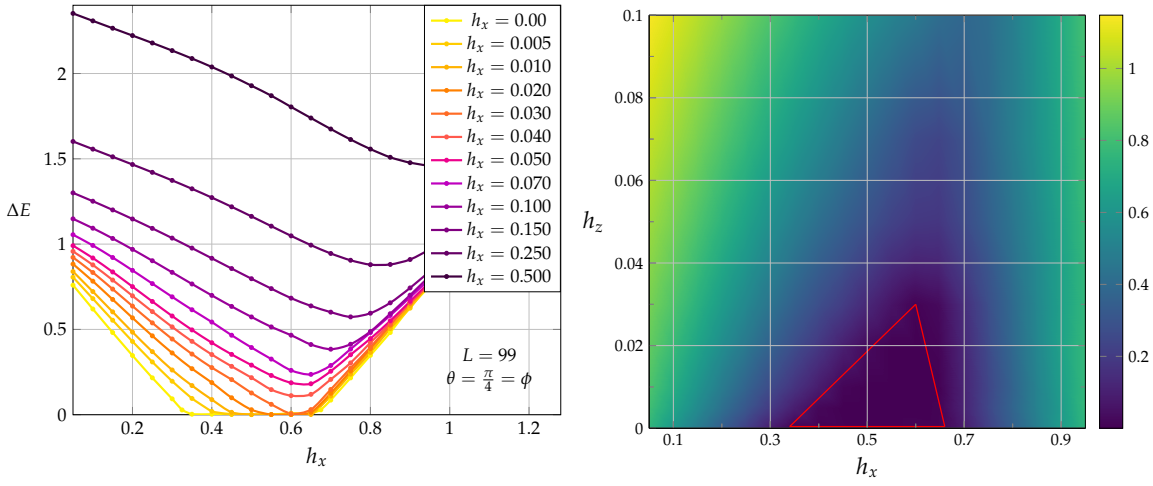

(a) Energy gap vs h_x **(b)** Phase diagram

Figure 4.34: Phase diagram of the 3-state chiral clock model with both transverse and longitudinal field for $L = 99$ (OBC) and $\theta = \phi = \frac{\pi}{4}$ (self-dual case). On the left we see the plot of the energy gap for different values of the longitudinal field. On the right we show the resulting two-dimensional section of the phase diagram mapped via the energy gap up to $h_z = 0.1$. The critical incommensurate phase seems to persist even for small non-zero values of the longitudinal field.

For the 3-state chiral clock model (2.15) the situation is instead slightly different. Naively, we may have expected the critical incommensurate phase to disappear as far as we switch on the longitudinal field, but this is not the case. In fact, we see from Fig.4.34(a) that by increasing the magnitude of the longitudinal field from $h_x = 0.00$ up to $h_x \approx 0.03$ the incommensurate phase survives and it gets shorter until it shrinks into a single critical point for some special value of the field, say h_x^*, which should be approximately located within the range $0.030 \lesssim h_x^* \lesssim 0.035$. Such a persisting of the incommensurate phase even for non-zero values of the longitudinal field may either be a truly physical or a finite-size effect. We are not able to completely rule out the second scenario, yet we mention that we have checked values from $L = 60$ up to $L = 201$ and this phase seems to be stable, as it does not get significantly shorter by increasing the size of the system. We do not show the corresponding plot, but we mention that a similar behaviour with the incommensurate phase surviving and shrinking as h_x increases was observed even for a different choice of the angles, namely $\theta = \frac{\pi}{4}$ and $\phi = 0$. We also notice from Fig.4.34(a) that the incommensurate phase shrinks mostly from the left, i.e. from the Pokrovsky-Talapov side. This behaviour may be traced to the larger robustness of BKT transitions to external perturbation due to their topological nature. In Fig.4.34(b) we then show the resulting two-dimensional section of the phase diagram for $\theta = \phi = \frac{\pi}{4}$ fixed and $J = 1 - h_z$ as usual. We see that instead of a single critical point like in Fig.4.33(b), the phase diagram now hosts an entirely critical triangular-like region.

We finally notice that both in the symmetric and in the chiral case for $h_x \gtrsim 0.3$, where the energy spectrum is completely gapped, we remain within the ordered phase as the longitudinal field forces the ferromagnetic alignment of the spins [7]. Also, consistently with the literature about the Ising model, we see that the self-duality property is lost as the application of the longitudinal field is known to spoil the Kramers-Wannier duality.

We end this discussion by providing some comments about how we have performed these numerical calculations. The previous plots have been obtained after removing the requirement of quantum number conservation throughout the DMRG calculations as the Hamiltonians (2.8) and (2.15) are no longer quantum number preserving. This is due to a technical issue: we cannot act with the operator Z or $Z^\dagger$ on a given state, the ground state in this case, and remain within the initial

[7] This is true at least for the particular Hamiltonians (2.8) and (2.15) we are considering, where we have taken the exchange interaction term to be ferromagnetic ($J > 0$) and the longitudinal field to have a minus sign in front. Different setups may correspond to different models with different phase diagrams.

symmetry sector at the same time. In fact, the action of this operator results in bringing the system into the next symmetry sector.

4.6.2 Duality with Lattice Gauge Theories

Let us now discuss clock models with both transverse and longitudinal fields within the framework of duality transformations with lattice gauge theories, as we have explained in the previous chapter. Due to the computational effort, we shall focus here only on the 3-state clock model.

Let us review the phase diagram of the dual lattice gauge theory to get a flavour of what we expect to find in the clock model formulation. For all three superselection sectors $n = 0, 1, 2$ the $\mathbb{Z}_3$ LGT does not seem to host any phase transition. Also, for $\lambda = 0$ all the sectors have a deconfined point. Thus, for $n = 0$ with $\lambda > 0$ we have a quick transition to a confined phase. Instead, for $n = 1$ and $n = 2$ - which are equivalent - the model seems to exhibit a smooth crossover for $\lambda > 1$, even if the scenario of a true phase transition cannot be ruled out [64]. Therefore, thanks to duality considerations, we expect the corresponding 3-state clock model (cfr. Hamiltonian (2.8)) to display a very similar behaviour. In particular, given $h = \lambda^{-1}$, in our case the phase diagram will host a deconfined point for $h \to \infty$. We also stress that due to the presence of the longitudinal field the expected three-fold degeneracy of the ordered phase of the purely transverse clock model is expected to break down to a two-fold degeneracy.

Our goal now is to present a purely numerical study of the 3-state clock model with both transverse and longitudinal fields to bring further evidence supporting the results of Ref. [64], where a first numerical approach to these models is presented. In particular, in this paper the $\mathbb{Z}_3$ LGT has been numerically investigated via exact diagonalisation technique. Here, we will instead work in the clock model formulation, thus reversing - in certain a sense - the “arrow" of the duality mapping. To make contact with the results about the dual LGT we have enforced periodic boundary conditions as well.

The sector $n = 0$ is not particularly interesting as here the magnitude of the longitudinal field becomes real, namely $h_z = 2$. We can extrapolate the behaviour of this model under these conditions by looking at the plot in Fig.4.33(a). There we see indeed that no phase transition occurs as the energy spectrum is completely gapped. Moreover, the corresponding deconfined point cannot be appreciated in this formulation as it is located at infinity.

On the other hand sectors $n = 1$ and $n = 2$ are more interesting. In order to

be able to make a direct comparison with the plots shown in Ref. [64] we have here considered the Hamiltonian (2.9) under periodic boundary conditions, which is unitarily equivalent to (2.8). We have firstly studied the energy gaps $\Delta E_i = E_i - E_0$ with $i = 1, 2$ for both $n = 1$ and $n = 2$. We show the resulting plot in Fig.4.35. We stress that the very same behaviours have been observed for both sectors, which are indeed equivalent. Moreover, we see that a two-fold degeneracy of the ground state emerges for $h > 1$, just as in the dual LGT.

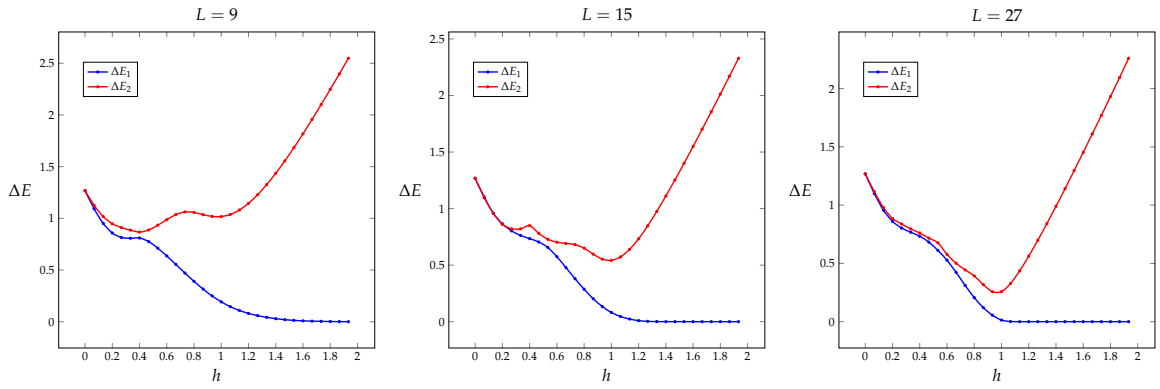

Figure 4.35: Energy gaps $\Delta E_i = E_i - E_0$, $i = 1, 2$ of the 3-state clock model with transverse and longitudinal fields for $L = 9,\ 15$ and 27 (from left to right). For $h > 1$ a two-fold degeneracy of the ground state emerges, consistently with the results in Ref. [64].

The second observable we have considered in order to investigate the phase diagram of these models is the transverse magnetisation (4.1), we show the resulting plot in Fig.4.36(a). All the curves of the magnetisation cross at a single point $h \approx 0.825$, which is a typical behaviour signalling a phase transition in the thermodynamic limit, as we have already studied for the purely transverse 3-state clock model. However, we notice that in Ref. [64] - although they do not exclude the possibility of having a true phase transition - a rather smooth crossover between the two phases is observed in the plot of the half-ladder Wilson loop. This apparent discrepancy may have a double origin. First of all, we are not comparing the same observables, as, strictly speaking, the Wilson loop is dual to a disorder parameter given by the expectation value of a product of X operators. Both this disorder parameter and the transverse magnetisation measure the lack of order along the z-direction, but they are different quantities. The second possibility is that the phase transition reveals itself only at higher sizes, like those we are considering. We stress again that in Ref. [64] all the numerical simulation have been performed via exact diagonalisation. This technique allows for a higher accuracy at the cost of accessing small sizes only, which is not

our case and indeed here we could reach higher chain lengths (up to $L = 27$).

Another interesting observable we may take into account is the "longitudinal" magnetisation $\tilde{M} \equiv \frac{1}{2L}\sum_i (Z_i + Z_i^\dagger)$, which is also expected to signal the qualitative change in the ground state of this model, namely the emergence of a two-fold degeneracy for $h > 1$, as we are moving towards a z-ordered phase. We show the plot of the longitudinal magnetisation in Fig.4.36(b). We see that this observable does indeed capture this behaviour as the curves - although without crossing - display a point of inflection which gets shifted toward unity from the right, $h \to 1^+$, due to finite-size effects.

Finally, our analysis of the magnetisation seems to suggest that in the thermodynamic limit these models may undergo a true phase transition at $h \approx 1$, rather than a smooth crossover. We will not take into account different observables here, even if we stress that this may be helpful in shedding light about the behaviour of the system at $h \approx 1$ and, if a phase transition is indeed present, even about its nature. We defer all these issues to future studies.

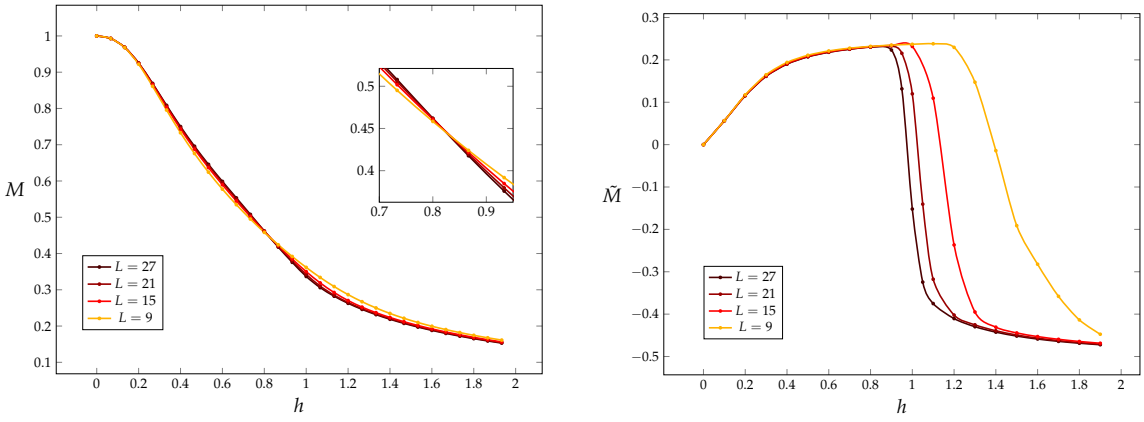

(a) Transverse magnetisation (in X)

(b) Longitudinal magnetisation (in Z)

Figure 4.36: Transverse (left) and longitudinal (right) magnetisation of the 3-state clock model with transverse and longitudinal fields for $L = 9,\ 15,\ 21$ and 27 as a function of h. The curves of the transverse one cross at a single point, $h \approx 0.825$, which is typical of a phase transition occurring in the thermodynamic limit. Inset: focus on a neighbourhood of the crossing. The longitudinal magnetisation is also sensitive to the qualitative change in the ground state of the model occurring for $h \approx 1$. However, despite the previous case, now the curves do not cross.

Conclusions and outlooks

Throughout this dissertation we have discussed both symmetric and chiral quantum clock models in one dimension via duality transformations and numerical simulations based on DMRG. Firstly, by studying the behaviour of the main thermodynamic observables at criticality, we have been able to reconstruct a picture of the well-understood phase diagram of symmetric clock models, finding results which are all consistent with the literature. We have thereafter applied the same machinery to chiral clock models as well, sticking to the $p = 3$ case, and carried out a similar analysis. Here, by trying to address those issues which are still controversial in the literature, we have found evidences of level-crossing between the ground states of the different symmetry sectors both within the floating incommensurate phase and along the critical line $h = 0.5$ at small angles. This behaviour, which is likely due to the interplay of finite size, symmetry constraints, clock order and chirality, might - among others - provide a reasonable explanation for the Lifshitz oscillations observed in the energy gap as a function of the chain length. Finally, we have studied symmetric and chiral models with order $p = 3$ by adding both transverse and longitudinal fields. As the literature for this particular setup is not so rich, in the symmetric case we have closely followed the discussion of the ferromagnetic Ising model and invoked duality considerations. In this case we have then found that the longitudinal field removes the non-analiticity in the ground state energy as far as it is switched on. Thus, the energy spectrum of the 3-state symmetric clock model with both transverse and longitudinal fields is completely gapped. We stress that this behaviour is fully consistent with the literature about the Ising model under the same setup. Instead, for the 3-state chiral clock model we have found that the floating incommensurate phase persists when the longitudinal field is weak and, as this field is lowered, it shrinks from the Pokrovsky-Talapov side until it disappears completely. Such a behaviour seems stable under finite-size effects, at least for the specific sizes we have considered. Finally, the duality between Abelian $\mathbb{Z}_p$ lattice gauge theories and p-state symmetric clock models has been numerically investigated in the clock model formulation, finding results which are mostly consistent with recent works.

We now want to conclude this thesis by outlining some pathways for possible future research. First of all, in order to bring further evidence to the literature, disposing of more time and computational resources, a more detailed studied on higher order symmetric and chiral clock models could be carried out and all the previous results could be tested with a higher accuracy as well. Also, different numerical methods, besides the standard DMRG, may be used to tackle these same problems from different points of view. This may indeed shed some light on those controversial issues like the topology of the phase diagram of the 3-state chiral clock model, in order to better understand whether there exists a Lifshitz point with a phase transition falling into the chiral universality class at small angles - like recent works seem to suggest - or simply a thin incommensurate layer extends down to the 3-Potts point. The phase diagram of the 3-state chiral clock model with both transverse and longitudinal fields might be worth of further investigation as well in order to understand whether the incommensurate phase indeed survives when the longitudinal field is weak or not. If this behaviour is confirmed, this may be the simplest clock model characterised by the coexistence of criticality and longitudinal field, as we recall that both in the Ising model and in the 3-state symmetric clock model no phase transition occurs when a longitudinal field is present. The duality between lattice gauge theories and clock models may also be notable of further studies, hopefully even providing more analytical insights about the inverse duality mapping, namely from clock models to lattice gauge theories. Finally, it would be extremely interesting - and indeed there are already some works pushing towards this direction [82] - to address the problem of the commensurate-incommensurate transition from the field theoretical point of view and in the fermion language as well.

A

Computational tools

In this appendix we collect the descriptions of the main computational tools we have used all along this dissertation. In particular, we mainly focus on how DMRG works, distinguishing between infinite-system and finite-system DMRG. Then, given that all numerical simulations have been performed using the ITensor software library, we think necessary to provide a short overview on the Tensor Networks method as well.

A.1 The Density Matrix Renormalisation Group

The Density Matrix Renormalisation Group (DMRG) is nowadays one of the most powerful and successful variational algorithms for computing the low-energy properties of one-dimensional quantum systems. Thanks to its ability of dealing with strongly correlated systems in general, its area of application actually goes beyond quantum many-body theory, ranging from quantum chemistry to nuclear physics. It was invented by Steven R. White in 1992 [81] in order to overcome the technical problems of Real Space Renormalisation Group (RSRG) which had proven to be unreliable when applied to some particular quantum models, like the Hubbard and the Heisenberg ones. The crucial idea behind DMRG relies on the usage of the eigenstates of the density matrix of the system rather than those of the Hamiltonian. This indeed allows for an accurate description of systems which are strongly coupled

to the environment. Since its introduction, many different versions of DMRG have then been invented, like time-dependent DMRG (tDMRG), finite-temperature DMRG and so on, together with its generalisation to two-dimensional quantum systems as well. In the present section we shall focus on time-independent DMRG at zero temperature for one-dimensional quantum systems, as all the numerical simulations we have performed fall into this case. Also, in the following we will consider open boundary conditions, as we have mostly done in our dissertation. Indeed, despite lots of numerical methods and most of the analytical ones use periodic boundary conditions in order to mimic the ideal setup of infinite system - avoiding boundary effects - DMRG prefers open boundary conditions.

The primary goal of DMRG is computing the ground state and the ground state energy of a one-dimensional quantum system of length L with Hamiltonian H. This can be done either in the thermodynamic limit for $L \to \infty$ with a modest accuracy or in the finite case $L < \infty$ with higher accuracy. These two versions go under the name of infinite-system and finite-system DMRG, respectively, which we are now going to discuss. However, we stress that both of them have to face the problem of the exponential growth of the Hilbert space, e.g. for a $\frac{1}{2}$-spin system it grows like 2^L.

A.1.1 Infinite-system DMRG

The infinite-system DMRG procedure works as follows [72]. First of all we need to find the reduced space containing all the relevant physics. Such a reduced space does exist for one-dimensional quantum systems and can be found by

(i) introducing a left and right block, A and B, containing one site each so that at the beginning the chain length is $L = 2$;

(ii) building iteratively longer chains by adding - between the blocks - one site to each block at any step, so that the full block state space grows like 2^ℓ, being ℓ the current block size. Such a chain $2\ell + 2$ sites long is usually referred to as *superblock*;

(iii) defining an orthonormal basis $\{|a_\ell\rangle_{A,B}\}$ for the reduced Hilbert space which we assume to be χ-dimensional (being χ the *bond dimension*) so that any state $|\psi\rangle$ of the superblock may be expressed as

$$|\psi\rangle = \sum_{a_A,\sigma_A,a_B,\sigma_B} \psi_{a_A\sigma_A a_B\sigma_B} |a\rangle_A |\sigma\rangle_A |\sigma\rangle_B |a\rangle_B \equiv \sum_{i_A,j_B} \psi_{i_A j_B} |i\rangle_A |j\rangle_B \tag{A.1}$$

where $\{|\sigma\rangle_{A,B}\}$ is a basis for the d-dimensional local state space hosting the states of the sites next to A and B, respectively, while $\{|i\rangle_A\}$ $\{|j\rangle_B\}$ are the

$(d\chi)$-dimensional basis of the corresponding block together with the nearby site, say $A\bullet$ and $\bullet B$;

(iv) performing a numerical diagonalisation (via Lanczos or Davidson algorithms) to find the state $|\psi_0\rangle$ which minimises the energy

$$E = \frac{\langle\psi_0|H_{sup}|\psi_0\rangle}{\langle\psi_0|\psi_0\rangle} \tag{A.2}$$

being H_{sup} the superblock Hamiltonian;

(v) avoiding the exponential growth of the bases $\{|i\rangle_A\}$, $\{|j\rangle_B\}$ by truncating them to χ states. This can be achieved by introducing the density matrices of the larger blocks $A\bullet$ and $\bullet B$, namely

$$\rho_{A\bullet} = \mathrm{Tr}_{\bullet B}\,|\psi_0\rangle\langle\psi_0| \quad \text{and} \quad \rho_{\bullet B} = \mathrm{Tr}_{A\bullet}\,|\psi_0\rangle\langle\psi_0| \tag{A.3}$$

respectively, whose eigenstates are determined via exact diagonalisation. Next we perform the truncation by retaining as reduced basis only those χ orthonormal eigenstates of the density matrix having the largest eigenvalues;

(vi) performing an approximate change of basis so that we may increase again the system size until the desired value.

A.1.2 Finite-system DMRG

For a higher accuracy finite-system DMRG is usually preferred. We stress that both methods deal with the iterative growth of the blocks. The main difference is that while in infinite-system DMRG this growth occurs at both sides, in the finite-system case it occurs only at one side at the expense of the other. More precisely, finite-system DMRG consists in [72]

(i) stopping infinite-system DMRG up to some desired length L;

(ii) repeating the same procedure we have described for infinite-system DMRG, but now for one block only, say block B, at the expense of block A, which shrinks down to its minimal size, i.e. the size for which the dimension of the Hilbert space of block A does not exceed χ;

(iii) reversing then the growth direction and doing the same for block A as block B shrinks;

(iv) repeating this *sweeping procedure* until the convergence of the wave function is reached.

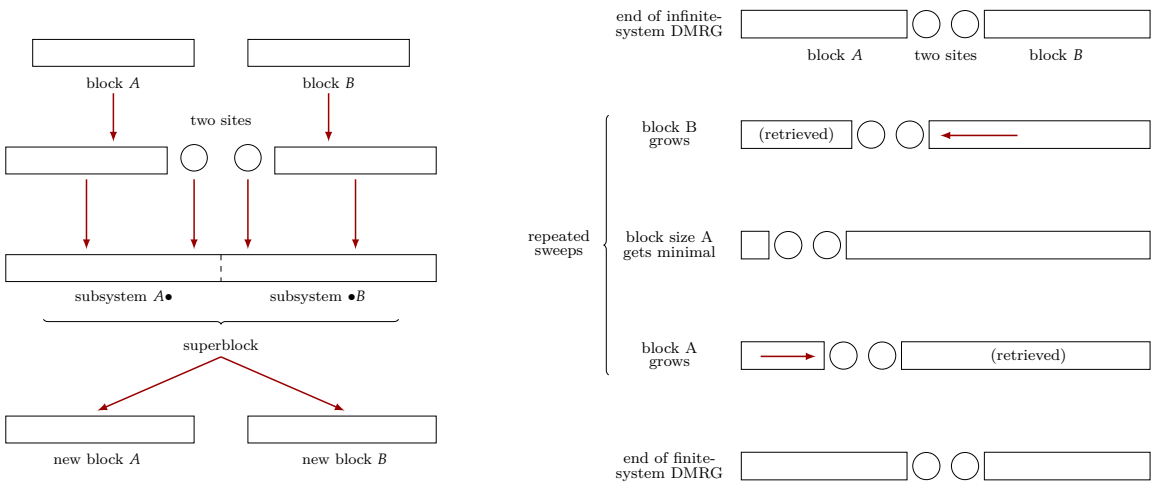

(a) Infinite-system DMRG **(b)** Finite-system DMRG

Figure A.1: Schematic representation of infinite-system DMRG vs finite-system DMRG. These sketches have been realised following Fig.2 of Ref. [72].

In order to find out the ground state $|\psi_0\rangle$ of each superblock this method needs to use some iterative large sparse matrix eigensolver consisting in the sequential applications of the Hamiltonian on the input wavefunction. This is the reason why it is important to choose the initial wavefunction to be as closer as possible to the final one in order both to make the convergence easier and to save computational time.

A pictorial representation of infinite- and finite-system DMRG is sketched in Fig.A.1(a) and (b) respectively.

A.2 Tensor Networks: a brief overview

Tensor networks are representations of high-order tensors as the contracted product of many low-order tensors. Since their introduction, they have gained a huge popularity because they allow for an intuitive diagrammatic notation which makes tensors extremely simpler to handle. All the numerical results presented in this dissertation have been obtained by using ITensor, which is a tensor-network-inspired software library which provides the advantage of translating tensor diagrams directly into code [29].

The most common and widely used tensor networks formats are matrix product states (MPS) and matrix product operators (MPO). Let us discuss them in detail.

A.2.1 Matrix Product States

For local Hamiltonians with a gap between the ground state and the first excited state finding the ground state is a relatively easy task. Despite the problem of the exponential growth of the Hilbert space, when the Hamiltonian of the system satisfies the previous requirements the relevant corner of the Hilbert space we may restrict ourselves to is actually small and it may be efficiently parametrised by using matrix product states. Let us see how to decompose an arbitrary quantum state into a MPS [72]. Consider a chain or more generally a lattice [8] with L sites and let $\{\sigma_i\}$ be the d-dimensional local state space at the i-th site. The most general representation of a pure quantum state $|\psi\rangle$ (which we will assume to be normalised) reads

$$|\psi\rangle = \sum_{\sigma_1,\ldots,\sigma_L} c_{\sigma_1\ldots\sigma_L}|\sigma_1,\ldots,\sigma_L\rangle \tag{A.4}$$

for some coefficients $c_{\sigma_1\ldots\sigma_L}$. We may then recast our d^L-dimensional state vector into a $(d \times d^{L-1})$ matrix, say Ψ, with components $\Psi_{\sigma_1,(\sigma_2\ldots\sigma_L)} = c_{\sigma_1\ldots\sigma_L}$. A singular value decomposition (SVD) of this matrix provides

$$c_{\sigma_1\ldots\sigma_L} = \Psi_{\sigma_1,(\sigma_2\ldots\sigma_L)} = \sum_{a_1}^{r_1} U_{\sigma_1,a_1} S_{a_1,a_1} (V^\dagger)_{a_1,(\sigma_2\ldots\sigma_L)} \equiv \sum_{a_1}^{r_1} U_{\sigma_1,a_1} c_{a_1\sigma_2\ldots\sigma_L)} \tag{A.5}$$

with U and V unitary, S diagonal, $r_1 \leq d$ and in the last step we have again recast the product $(SV^\dagger)$ into a vector. By decomposing U into a collection of d row vectors A^{σ_1} with entries $A^{\sigma_1}_{a1} = U_{\sigma_1,a_1}$ and writing $c_{a_1,(\sigma_2\ldots\sigma_L)}$ as a $(r_1 d \times d^{L-2})$ matrix $\Psi_{(a_1\sigma_1),(\sigma_3\ldots\sigma_L)}$, (A.5) becomes

$$c_{\sigma_1\ldots\sigma_L} = \sum_{a_1}^{r_1} A^{\sigma_1}_{a1} \Psi_{(a_1\sigma_1),(\sigma_3\ldots\sigma_L)} \,. \tag{A.6}$$

Performing then another SVD on Ψ, we find

$$c_{\sigma_1\ldots\sigma_L} = \sum_{a_2}^{r_2}\sum_{a_1}^{r_1} A^{\sigma_1}_{a_1} U_{(a_1\sigma_2),a_2} S_{a_2,a_2} (V^\dagger)_{a_2,(\sigma_3\ldots\sigma_L)} = \sum_{a_2}^{r_2}\sum_{a_1}^{r_1} A^{\sigma_1}_{a_1} A^{\sigma_2}_{a_1,a_2} \Psi_{(a_2\sigma_3),(\sigma_4\ldots\sigma_L)} \tag{A.7}$$

where now A^{σ_2} are d $(r_1 \times r_2)$ matrices having entries $A^{\sigma_2}_{a_1,a_2} = U_{(a_1\sigma_2),a_2}$, Ψ is a $(r_2 d \times d^{L-3})$ matrix and $r_2 \leq r_1 d \leq d^2$. Going further in performing SVDs, at the end we find

$$c_{\sigma_1\ldots\sigma_L} = \sum_{a_1,\ldots,a_{L-1}} A^{\sigma_1}_{a_1} A^{\sigma_2}_{a_1,a_2} \ldots A^{\sigma_{L-1}}_{a_{L-2},a_{L-1}} A^{\sigma_L}_{a_{L-1}} \equiv A^{\sigma_1} A^{\sigma_2} \ldots A^{\sigma_{L-1}} A^{\sigma_L} \,. \tag{A.8}$$

[8] MPS are numerically manageable only in one dimension, but nothing prevents us to be more general.

Thus, we are finally able to write our quantum state $|\psi\rangle$ as matrix product state in the form

$$|\psi\rangle = \sum_{\sigma_1,\ldots,\sigma_L} A^{\sigma_1} A^{\sigma_2} \ldots A^{\sigma_{L-1}} A^{\sigma_L} |\sigma_1, \ldots, \sigma_L\rangle \ . \tag{A.9}$$

More precisely, this representation of $|\psi\rangle$ takes the name of *left-canonical matrix product state* as this MPS representation consists only in left-normalised matrices, i.e. matrices satisfying

$$\sum_{\sigma_\ell} A^{\sigma_\ell \dagger} A^{\sigma_\ell} = \mathbb{1} \ . \tag{A.10}$$

A similar *right-canonical matrix product state* representation does exist as welly

$$|\psi\rangle = \sum_{\sigma_1,\ldots,\sigma_L} B^{\sigma_1} B^{\sigma_2} \ldots B^{\sigma_{L-1}} B^{\sigma_L} |\sigma_1, \ldots, \sigma_L\rangle \ . \tag{A.11}$$

where now these matrices obey

$$\sum_{\sigma_\ell} B^{\sigma_\ell} B^{\sigma_\ell \dagger} = \mathbb{1} \ . \tag{A.12}$$

and thus they are said to be right-normalised.

Before concluding the discussion of MPS, we want to underline two points. Firstly, gauge degrees of freedom do exist in these representations, thus MPS are not unique. Secondly, there exists a deep connection between DMRG and MPS, as it has been discovered that finite-system DMRG leads to quantum states in MPS form. Thus, it is possible and even more natural to rephrase the entire DMRG implementation using the language of MPS as ITensor does.

A.2.2 Matrix Product Operators

The Matrix Product Operators (MPO) representation is straightforward once we have become familiar with MPS. Indeed we may naturally generalise the expression of a single coefficient of a MPS, namely

$$\langle \vec{\sigma} | \psi \rangle = M^{\sigma_1} M^{\sigma_2} \ldots M^{\sigma_{L-1}} M^{\sigma_L} \tag{A.13}$$

and write the coefficients of an arbitrary operator $\hat{O}$ as

$$\langle \vec{\sigma} | \hat{O} | \vec{\sigma}' \rangle = W^{\sigma_1,\sigma_1'} W^{\sigma_2,\sigma_2'} \ldots W^{\sigma_{L-1},\sigma_{L-1}'} W^{\sigma_L,\sigma_L'} \ , \tag{A.14}$$

where now the operator reads

$$\hat{O} = \sum_{\vec{\sigma},\vec{\sigma}'} W^{\sigma_1,\sigma_1'} W^{\sigma_2,\sigma_2'} \ldots W^{\sigma_{L-1},\sigma_{L-1}'} W^{\sigma_L,\sigma_L'} |\vec{\sigma}\rangle\langle\vec{\sigma}'| \ . \tag{A.15}$$

For our numerical simulations with DMRG we have used Hamiltonians in MPO representations.

Bibliography

[1] G. Albertini, B. M. McCoy and J. H.H. Perk. "Commensurate-incommensurate transition in the ground state of the superintegrable chiral Potts model". *Physics Letters A* 135 (1989), 159. DOI: https://doi.org/10.1016/0375-9601(89)90254-5.

[2] T. Andrews. "The Bakerian lecture: On the continuity of the gaseous and liquid states of matter". *Phil. Trans. R. Soc.* 159 (1869), 106.

[3] J. Ashkin and E. Teller. "Statistics of Two-Dimensional Lattices with Four Components". *Phys. Rev.* 64 (1943), 178. DOI: 10.1103/PhysRev.64.178.

[4] P. Bak. "Commensurate phases, incommensurate phases and the devil's staircase". *Reports on Progress in Physics* 45 (1982). DOI: 10.1088/0034-4885/45/6/001.

[5] R.J. Baxter. *Exactly Solved Models in Statistical Mechanics*. Dover Publications, 2007.

[6] J. G. Bednorz and K. A. Müller. "Possible high T_c superconductivity in the BaLaCuO system". *Zeitschrift für Physik B Condensed Matter* 64 (1986), 189. DOI: https://doi.org/10.1007/BF01303701.

[7] V. L. Berezinskii. "Destruction of long range order in one-dimensional and two-dimensional systems having a continuous symmetry group. I. Classical systems". *Sov. Phys. JETP* 32 (1971), 493.

[8] V. L. Berezinskii. "Destruction of long-range Order in one-dimensional and two-dimensional systems possessing a continuous symmetry group. II. Quantum Systems." *Sov. Phys. JETP* 34 (1972), 610.

[9] K. Binder. "Finite size scaling analysis of ising model block distribution functions". *Zeitschrift für Physik B Condensed Matter* 43 (1981), 119. DOI: 10.1007/BF01293604.

[10] R. Brun and F. Rademakers. "ROOT: An object oriented data analysis framework". *Nucl. Instrum. Meth. A* 389 (1997). Ed. by M. Werlen and D. Perret-Gallix, 81. DOI: 10.1016/S0168-9002(97)00048-X.

[11] P. Calabrese and J. Cardy. "Entanglement entropy and conformal field theory". *Journal of Physics A: Mathematical and Theoretical* 42 (2009), 504005. DOI: 10.1088/1751-8113/42/50/504005.

[12] J. Cardy, P. Goddard and J. Yeomans. *Scaling and Renormalization in Statistical Physics*. Cambridge University Press, 1996.

[13] P. M. Chaikin and T. C. Lubensky. *Principles of Condensed Matter Physics*. Cambridge University Press, 1995.

[14] X. Chen, Z.-C. Gu and X.-G. Wen. "Local unitary transformation, long-range quantum entanglement, wave function renormalization, and topological order". *Phys. Rev. B* 82 (2010), 155138. DOI: 10.1103/physrevb.82.155138.

[15] N. Chepiga and F. Mila. "Floating Phase versus Chiral Transition in a 1D Hard-Boson Model". *Phys. Rev. Lett.* 122 (2019), 017205. DOI: 10.1103/PhysRevLett.122.017205.

[16] N. Chepiga and F. Mila. "Kibble-Zurek exponent and chiral transition of the period-4 phase of Rydberg chains". *Nature Communications* 12 (2021). DOI: 10.1038/s41467-020-20641-y.

[17] N. Chepiga and F. Mila. "Lifshitz point at commensurate melting of chains of Rydberg atoms". *Phys. Rev. Research* 3 (2021), 023049. DOI: 10.1103/PhysRevResearch.3.023049.

[18] P. Christe and M. Henkel. *Introduction to Conformal Invariance and Its Applications to Critical Phenomena*. Springer Berlin Heidelberg, 1993.

[19] E. Cobanera, G. Ortiz and Z. Nussinov. "The bond-algebraic approach to dualities". *Advances in Physics* 60 (2011), 679. DOI: 10.1080/00018732.2011.619814.

[20] P. Di Francesco, P. Mathieu and D. Sénéchal. *Conformal Field Theory*. Springer, 1997.

[21] A. Einstein. "The theory of opalescence of homogeneous fluids and liquid mixtures near the critical state". *Annalen der Physik* 33 (1910), 1275.

[22] S. Elitzur, R. B. Pearson and J. Shigemitsu. "Phase structure of discrete Abelian spin and gauge systems". *Phys. Rev. D* 19 (1979), 3698. DOI: 10.1103/PhysRevD.19.3698.

[23] E. Ercolessi, G. Morandi and F. Napoli. *Statistical Mechanics: An Intermediate Course (2nd Edition)*. World Scientific Publishing Company, 2001.

[24] J. W. Essam and M. E. Fisher. "Padé Approximant Studies of the Lattice Gas and Ising Ferromagnet below the Critical Point". *The Journal of Chemical Physics* 38 (1963), 802. DOI: 10.1063/1.1733766.

[25] P. Fendley. "Parafermionic edge zero modes in Z_n-invariant spin chains". *Journal of Statistical Mechanics: Theory and Experiment* 2012 (2012), P11020. DOI: 10.1088/1742-5468/2012/11/p11020.

[26] R. P. Feynman and A. R. Hibbs. *Quantum Mechanics and Path Integrals*. McGraw-Hill, 1965.

[27] M. E. Fisher. "Rigorous inequalities for critical-point correlation exponents". *Phys. Rev.* 180 (1969), 594. DOI: 10.1103/PhysRev.180.594.

[28] M. E. Fisher and M. N. Barber. "Scaling Theory for Finite-Size Effects in the Critical Region". *Phys. Rev. Lett.* 28 (1972), 1516. DOI: 10.1103/PhysRevLett.28.1516.

[29] M. Fishman, S. R. White and E. M. Stoudenmire. *The ITensor Software Library for Tensor Network Calculations*. 2020. arXiv: 2007.14822.

[30] E. Fradkin. *Field Theories of Condensed Matter Physics*. Cambridge University Press, 2013.

[31] E. Fradkin and L. P. Kadanoff. "Disorder variables and para-fermions in two-dimensional statistical mechanics". *Nuclear Physics B* 170 (1980), 1. DOI: https://doi.org/10.1016/0550-3213(80)90472-1.

[32] E. Fradkin and L. Susskind. "Order and disorder in gauge systems and magnets". *Phys. Rev. D* 17 (1978), 2637. DOI: 10.1103/PhysRevD.17.2637.

[33] R. B. Griffiths. "Thermodynamic inequality near the critical point for ferromagnets and fluids". *Phys. Rev. Lett.* 14 (1965), 623. DOI: 10.1103/PhysRevLett.14.623.

[34] C. Hoeger, G. von Gehlen and V. Rittenberg. "Finite-size scaling for quantum chains with an oscillatory energy gap". *Journal of Physics A: Mathematical and General* (1985), 1813. DOI: 10.1088/0305-4470/18/10/033.

[35] S. Howes, L. P. Kadanoff and M. Den Nijs. "Quantum model for commensurate-incommensurate transitions". *Nuclear Physics B* 215 (1983), 169. DOI: https://doi.org/10.1016/0550-3213(83)90212-2.

[36] D. A. Huse and M. E. Fisher. "Domain Walls and the Melting of Commensurate Surface Phases". *Phys. Rev. Lett.* 49 (1982), 793. DOI: 10.1103/PhysRevLett.49.793.

[37] E Ising. "Beitrag zur Theorie des Ferromagnetismus". *Zeitschrift für Physik* 31 (1925), 253. DOI: https://doi.org/10.1007/BF02980577.

[38] C. Itzykson and J.-M. Drouffe. Vol. 1. Cambridge University Press, 1989.

[39] B. D. Josephson. "Inequality for the specific heat: I. Derivation". *Proceedings of the Physical Society* 92 (1967), 269. DOI: 10.1088/0370-1328/92/2/301.

[40] B. D. Josephson. "Inequality for the specific heat: II. Application to critical phenomena". *Proceedings of the Physical Society* 92 (1967), 276. DOI: 10.1088/0370-1328/92/2/302.

[41] A. Yu. Kitaev. "Fault-tolerant quantum computation by anyons". *Annals of Physics* 303 (2003), 2. DOI: 10.1016/s0003-4916(02)00018-0.

[42] A. Yu. Kitaev. "Unpaired Majorana fermions in quantum wires". *Physics-Uspekhi* 44 (2001), 131. DOI: 10.1070/1063-7869/44/10s/s29.

[43] J. Kogut and L. Susskind. "Hamiltonian formulation of Wilson's lattice gauge theories". *Phys. Rev. D* 11 (1975), 395. DOI: 10.1103/PhysRevD.11.395.

[44] J. M. Kosterlitz and D. J. Thouless. "Ordering, metastability and phase transitions in two-dimensional systems". *Journal of Physics C: Solid State Physics* 6 (1973), 1181. DOI: 10.1088/0022-3719/6/7/010.

[45] H. A. Kramers and G. H. Wannier. "Statistics of the Two-Dimensional Ferromagnet. Part I". *Phys. Rev.* 60 (1941), 252. DOI: 10.1103/PhysRev.60.252.

[46] H. A. Kramers and G. H. Wannier. "Statistics of the Two-Dimensional Ferromagnet. Part II". *Phys. Rev.* 60 (1941), 263. DOI: 10.1103/PhysRev.60.263.

[47] L. D. Landau and V. L. Ginzburg. "On the theory of superconductivity". *Zh. Eksp. Teor. Fiz.* 20 (1950), 1064.

[48] R. B. Laughlin. "Anomalous Quantum Hall Effect: An Incompressible Quantum Fluid with Fractionally Charged Excitations". *Phys. Rev. Lett.* 50 (1983), 1395. DOI: 10.1103/PhysRevLett.50.1395.

[49] P. Liang, R. Fazio and S. Chesi. "Commensurate-Incommensurate Transitions of the 1D Disordered Chiral Clock Model" (2022). DOI: 10.48550/ARXIV.2203.16879.

[50] P. Martin. *Potts Models and Related Problems in Statistical Mechanics*. WORLD SCIENTIFIC, 1991.

[51] B. M. McCoy and S. Roan. "Excitation spectrum and phase structure of the chiral Potts model". *Physics Letters A* 150 (1990), 347. DOI: https://doi.org/10.1016/0375-9601(90)90230-L.

[52] N. D. Mermin and H. Wagner. "Absence of ferromagnetism or antiferromagnetism in one- or two-dimensional isotropic Heisenberg models". *Phys. Rev. Lett.* 17 (1966), 1133. DOI: 10.1103/PhysRevLett.17.1133.

[53] R. S. K. Mong et al. "Universal Topological Quantum Computation from a Superconductor-Abelian Quantum Hall Heterostructure". *Phys. Rev. X* 4 (2014), 011036. DOI: 10.1103/PhysRevX.4.011036.

[54] G. Mussardo. *Statistical Field Theory: An Introduction to Exactly Solved Models in Statistical Physics*. Oxford University Press, 2010.

[55] J. D. Noh. "Operator growth in the transverse-field Ising spin chain with integrability-breaking longitudinal field". *Phys. Rev. E* 104 (2021), 034112. DOI: 10.1103/PhysRevE.104.034112.

[56] Z. Nussinov and G. Ortiz. "Bond algebras and exact solvability of Hamiltonians: Spin $S = \frac{1}{2}$ multilayer systems". *Phys. Rev. B* 79 (2009), 214440. DOI: 10.1103/PhysRevB.79.214440.

[57] S. Nyckees, J. Colbois and F. Mila. "Identifying the Huse-Fisher universality class of the three-state chiral Potts model". *Nuclear Physics B* 965 (2021), 115365. DOI: 10.1016/j.nuclphysb.2021.115365.

[58] S. Nyckees and F. Mila. "Commensurate-incommensurate transition in the chiral Ashkin-Teller model". *Phys. Rev. Research* 4 (2022), 013093. DOI: 10.1103/PhysRevResearch.4.013093.

[59] L. Onsager. "Crystal Statistics. I. A Two-Dimensional Model with an Order-Disorder Transition". *Phys. Rev.* 65 (1944), 117. DOI: 10.1103/PhysRev.65.117.

[60] G. Ortiz, E. Cobanera and Z. Nussinov. "Dualities and the phase diagram of the p-clock model". *Nuclear Physics B* 854 (2012), 780. DOI: https://doi.org/10.1016/j.nuclphysb.2011.09.012.

[61] S. Ostlund. "Incommensurate and commensurate phases in asymmetric clock models". *Phys. Rev. B* 24 (1981), 398. DOI: 10.1103/PhysRevB.24.398.

[62] V. L. Pokrovsky and A. L. Talapov. "Ground State, Spectrum, and Phase Diagram of Two-Dimensional Incommensurate Crystals". *Phys. Rev. Lett.* 42 (1979), 65. DOI: 10.1103/PhysRevLett.42.65.

[63] R. B. Potts. "Some generalized order-disorder transformations". *Mathematical Proceedings of the Cambridge Philosophical Society* 48 (1952), 106. DOI: 10.1017/S0305004100027419.

[64] S. Pradhan, A. Maroncelli and E. Ercolessi. "Discrete Abelian lattice gauge theories on a ladder and their dualities with quantum clock models" (2022). DOI: 10.48550/ARXIV.2208.04182.

[65] D. Radicevic. "Spin Structures and Exact Dualities in Low Dimensions" (2018). DOI: 10.48550/ARXIV.1809.07757.

[66] M. F. Araujo de Resende. "A pedagogical overview on 2D and 3D Toric Codes and the origin of their topological orders". *Reviews in Mathematical Physics* 32 (2020), 2030002. DOI: 10.1142/S0129055X20300022.

[67] M. Rodney et al. "Scaling of entanglement entropy across Lifshitz transitions". *Phys. Rev. B* 87 (2013), 115132. DOI: 10.1103/PhysRevB.87.115132.

[68] G. S. Rushbrooke. "On the Thermodynamics of the Critical Region for the Ising Problem". *The Journal of Chemical Physics* 39 (1963), 842. DOI: 10.1063/1.1734338.

[69] S. Sachdev. *Quantum Phase Transitions*. Cambridge University Press, 2011.

[70] S. Sachdev. "XY model: particle-vortex duality." (2018). URL: http://qpt.physics.harvard.edu/phys268b/Lec2_XYmodel_duality.pdf.

[71] R. Samajdar et al. "Numerical study of the chiral $\mathbb{Z}_3$ quantum phase transition in one spatial dimension". *Phys. Rev. A* 98 (2018), 023614. DOI: 10.1103/PhysRevA.98.023614.

[72] U. Schollwöck. "The density-matrix renormalization group in the age of matrix product states". *Annals of Physics* 326 (2011), 96. DOI: 10.1016/j.aop.2010.09.012.

[73] H. J. Schulz. "Critical behavior of commensurate-incommensurate phase transitions in two dimensions". *Phys. Rev. B* 22 (1980), 5274. DOI: 10.1103/PhysRevB.22.5274.

[74] J. Schwinger. "Unitary operator bases". *Proceedings of the National Academy of Sciences* 46 (1960), 570. DOI: 10.1073/pnas.46.4.570.

[75] M. von Smoluchowski. "Molekular-kinetische Theorie der Opaleszenz von Gasen im kritischen Zustand, sowie einiger verwandter Erscheinungen". *Annalen der Physik* 330 (1908), 205. DOI: 10.1002/andp.19083300203.

[76] A. D. Sokal. "Rigorous proof of the high-temperature Josephson inequality for critical exponents". *Journal of Statistical Physics* 25 (1981), 51. DOI: https://doi.org/10.1007/BF01008478.

[77] G. Sun et al. "Phase transitions in the $\mathbb{Z}_p$ and U(1) clock models". *Phys. Rev. B* 100 (2019), 094428. DOI: 10.1103/PhysRevB.100.094428.

[78] C. J. Turner et al. "Optimal free descriptions of many-body theories". *Nature Communications* 8 (2017), 14926. DOI: 10.1038/ncomms14926.

[79] G. Vidal et al. "Entanglement in Quantum Critical Phenomena". *Phys. Rev. Lett.* 90 (2003), 227902. DOI: 10.1103/PhysRevLett.90.227902.

[80] X.-G. Wen. "Topological Order: From Long-Range Entangled Quantum Matter to a Unified Origin of Light and Electrons". *ISRN Condensed Matter Physics* 2013 (2013), 1. DOI: 10.1155/2013/198710.

[81] S. R. White. "Density matrix formulation for quantum renormalization groups". *Phys. Rev. Lett.* 69 (1992), 2863. DOI: 10.1103/PhysRevLett.69.2863.

[82] S. Whitsitt, R. Samajdar and S. Sachdev. "Quantum field theory for the chiral clock transition in one spatial dimension". *Phys. Rev. B* 98 (2018), 205118. DOI: 10.1103/PhysRevB.98.205118.

[83] B. Widom. "Equation of State in the Neighborhood of the Critical Point". *The Journal of Chemical Physics* 43 (1965), 3898. DOI: 10.1063/1.1696618.

[84] K. G. Wilson. "Confinement of quarks". *Phys. Rev. D* 10 (1974), 2445. DOI: 10.1103/PhysRevD.10.2445.

[85] Y. Zhuang et al. "Phase diagram of the Z_3 parafermionic chain with chiral interactions". *Phys. Rev. B* 92 (2015), 035154. DOI: 10.1103/PhysRevB.92.035154.